university of groningen / faculty of science and engineering

MASTER THESIS

The Effect of Crystal Plastic Anisotropy on the Void Nucleation Process in BCC Ferrite

Supervisors:
dr. Francesco Maresca
prof. dr. ir. Erik van der Giessen
dr. Predrag Andric

Student name:
Andreas Christiaan van der Last
s3433374

October 7, 2022

CmME

Contents

List of Figures

Acknowledgements

In this thesis, a research project that lasted for +/- 28 weeks is described that was conducted at the Multi-Scale Mechanics (MSM) sub-group within the Computational Mechanical and Materials Engineering (CMME) research group at the University of Groningen. Along the way I learned a lot of different things, ranging from new software to (to me) quite unknown fields of science. Many people have helped me reach the goal of this project.

First of all, I would like to thank dr. Francesco Maresca, who was my first supervisor. His guidance was much appreciated for setting up the method, as well as doing research in general. He was always open to talk about whatever, whenever, and made me learn much about the fields of computational mechanics and crystal plasticity. Not only was his project-related guidance great, he also cares a lot about the well-being of his students.

Next, I want to thank dr. Predrag Andric for making time for our weekly meetings and giving great feedback to help me go in the right direction. Prof. dr. ir. Erik van der Giessen is thanked as well, for introducing me to this interesting field of science together with Francesco. Discussions with Lei Liu from TU Eindhoven about the plotting and meshing were greatly appreciated as well.

Finally, I would like to thank the entire MSM group, of which the members were always available for a discussion and (together with my classmates) made my mechanical engineering studies an unforgettable time.

Nomenclature

Abbreviations

Acronym	Description
1D	One-dimensional
BCC	Body-centered cubic
CPA	Crystal plasticity rotation A
CPB	Crystal plasticity rotation B
CPX	Crystal plasticity unrotated
E	Elasticity
EIM	Equivalent inclusion method
FCC	Face-centered cubic
FEM	Finite element method
GUI	Graphical user interface
HCP	Hexagonal closed-packed
LEFM	Linear elastic fracture mechanics
P	Isotropic plasticity
PDE	Partial differential equation
PTF	Isotropic plasticity Taylor factor
PVW	Principle of virtual work
SEM	Scanning electron microscopy

Notations and operations

Tensor notation	Index notation	Description
a, ε	a	Scalar
$\boldsymbol{a}$	a_i	Vector
$\boldsymbol{A}, \boldsymbol{\varepsilon}$	A_{ij}, ε_{ij}	2nd order tensor
$\mathbb{A}$	A_{ijkl}	4th order tensor
$\boldsymbol{C} = \boldsymbol{A}^T$	$C_{ij} = A_{ji}$	Transpose 2nd order tensor
$\mathbb{C} = \mathbb{A}^{LT}$	$C_{ijkl} = A_{jikl}$	Left transpose 4th order tensor
$\dot{a}$	$\dot{a}$	Rate, time derivative
$\hat{\boldsymbol{a}}$	$\hat{a_i}$	Nodal value
$\bar{\boldsymbol{A}}$	$\bar{A_{ij}}$	Tensor in intermediate configuration
$c = \boldsymbol{a} \cdot \boldsymbol{b}$	$c = a_i b_i$	Dot product between two vectors
$\boldsymbol{c} = \boldsymbol{A} \cdot \boldsymbol{b}$	$c_i = A_{ij} b_j$	Dot product between 2nd order tensor and vector
$c = \boldsymbol{A} : \boldsymbol{B}$	$c = A_{ij} B_{ij}$	Double dot product between two 2nd order tensors
$\boldsymbol{C} = \mathbb{A} : \boldsymbol{B}$	$C_{ij} = A_{ijkl} B_{kl}$	Double dot product between 4th order and 2nd order tensor
$\mathbb{C} = \mathbb{A} \odot \boldsymbol{B}$	$C_{ijkl} = A_{imkl} B_{mj}$	Contraction of 2nd index of 4th order tensor with 1st index of 2nd order tensor
$\boldsymbol{C} = \boldsymbol{a} \otimes \boldsymbol{b}$	$C_{ij} = a_i b_j$	Outer product of two vectors
$\mathbb{C} = \frac{\partial \boldsymbol{A}}{\partial \boldsymbol{B}}$	$C_{ijkl} = \frac{\partial A_{ij}}{\partial B_{kl}}$	Partial derivative of 2nd order tensor with respect to other 2nd order tensor
$\boldsymbol{I}$	$I_{ij} = \delta_{ij}$	2nd order identity tensor
$\mathbb{I}$	$I_{ijkl} = \delta_{ijkl}$	4th order identity tensor

Chapter 1

Introduction

Whether it is desired or not: materials fracture. This can be dangerous, especially if the fracture occurs in a rapid and unpredictable manner. Unpredictability is a key property of brittle fracture. This fracture type has catastrophic consequences, as can be observed in Figure 1.1, in which the brittle fracture of a pressure vessel is shown. If it is wanted to operate such a pressure vessel, for example, to store hydrogen in an efficient and safe manner, brittle fracture should be avoided at all costs.

Figure 1.1: Brittle fracture of a pressure vessel [1].

The unpredictable nature of brittle fracture follows from the fact that very little to no plastic deformation occurs. This unpredictability can be lowered by designing for another fracture mechanism, namely ductile fracture. This mechanism involves lots of plastic deformation, which can be detected and appropriate actions can be taken. Ductile fracture can be obtained by altering material properties and consists of a couple of steps. These steps comprise: void nucleation, void growth, void coalescence and eventually fracture. Parts of the process, or even the whole process, of ductile fracture, can be modelled using material models.

Material models that are utilised to describe the deformation of metals for engineering applications are most commonly based on two assumptions. These models usually assume that the material response is equivalent for all directions if the same load is applied, meaning that the material behaviour is isotropic. Also, it is often assumed that the material is homogeneous and that it deforms in the same way at each location inside the material. As a consequence of the larger length scales present in certain engineering applications (>1 mm), this simplification seems valid and can be applied for designing components. The criterion for yielding of a metal is determined

by its yield surface, which in reality multi-dimensional. The aforementioned assumptions, however, imply a transformation of this multi-dimensional yield surface into a one-dimensional (1D) yield point [2]. An example of this 1D yield point is given in the uniaxial stress-strain curve, as shown in Figure 1.2, which is an important mechanical measure for the design of materials.

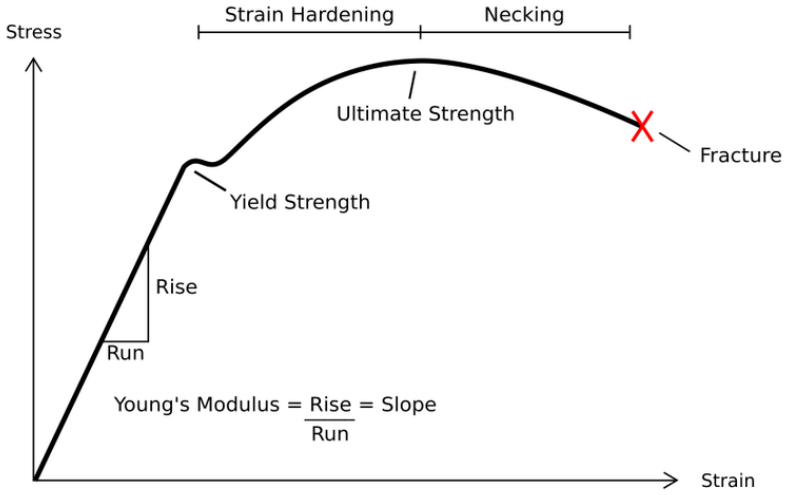

Figure 1.2: 1D stress-strain curve where the yield strength is represented by a scalar quantity [3].

Material response at the micrometer scales is substantially different compared to the larger engineering scale. At this length scale, it becomes clear that the earlier simplifications of the material being isotropic and homogeneous are invalid. Materials such as metals consist of multiple crystals (or grains) that are differently oriented. As a consequence, the plastic response of materials composed of grains depends on the loading direction with respect to their crystallographic orientations. By considering the crystal anisotropy involved in plastic deformation, constitutive equations describing the relation between plastic deformation and force are established. In this research, the void nucleation process of the ductile fracture mechanism will be investigated by taking into account the plastic anisotropy arising from crystallographic orientations. This is done using a numerical approach in which the finite element method (FEM) is applied in combination with constitutive equations that describe the deformation of crystalline materials.

Chapter 2

Literature review

Before the problem of void nucleation can be studied numerically, it is essential to comprehend material models that can be used for this purpose. In addition, the ductile fracture mechanism should be understood and specifically how to model the void nucleation part of this mechanism.

2.1 Elasticity material model

Elastic deformation can be characterised by the straight line at small strain in the stress-strain curve in Figure 1.2. The Saint-Venant model is a material model that can predict the elastic deformation of metals accurately. In this section, the mechanism behind elasticity will be discussed, as well as how it can be modelled.

2.1.1 Mechanism

Elastic deformation is the result of stretching or compressing atomic bonds. In Figure 2.1, an initially perfect crystal is illustrated which undergoes a purely elastic shape change due to shear. A distorted lattice is the result of this shear. The external cause for this deformation must be maintained to keep the distorted lattice. When the external cause is removed, the lattice deforms back to its original shape [2].

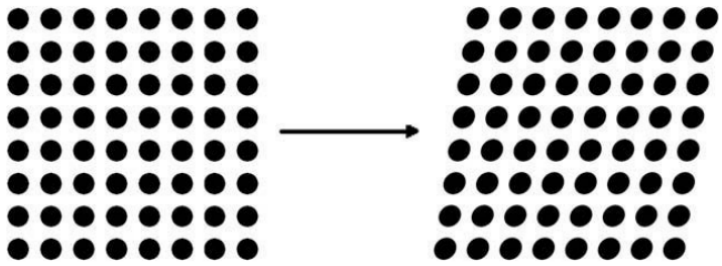

Figure 2.1: Example of pure elastic lattice deformation [2].

2.1.2 Kinematics

The kinematics of finite deformations describes the process during which a reference configuration is deformed into the current configuration as a result of applied forces and displacements [2]. This process is depicted schematically in Figure 2.2. When $\boldsymbol{y}$ and $\boldsymbol{x}$ are the positions of a point inside a material in the current and reference configuration, respectively, the deformation gradient is defined as:

$$\boldsymbol{F} = \nabla \boldsymbol{y}(\boldsymbol{x}) \tag{2.1}$$

For later use it is also convenient to define the right Cauchy-Green tensor $\boldsymbol{C}$ as:

$$\boldsymbol{C} = \boldsymbol{F}^T \cdot \boldsymbol{F} \tag{2.2}$$

and the Green-Lagrange strain $\boldsymbol{E}$:

$$\boldsymbol{E} = \frac{1}{2}\left(\boldsymbol{C} - \boldsymbol{I}\right) \tag{2.3}$$

In addition, the first $\boldsymbol{P}$ and second $\boldsymbol{S}$ Piola-Kirchhoff stress tensors are introduced, where $\boldsymbol{S}$ is defined in the reference configuration. The relation between these two stress tensors is given through the deformation gradient by the following equation:

$$\boldsymbol{P} = \boldsymbol{F} \cdot \boldsymbol{S} \tag{2.4}$$

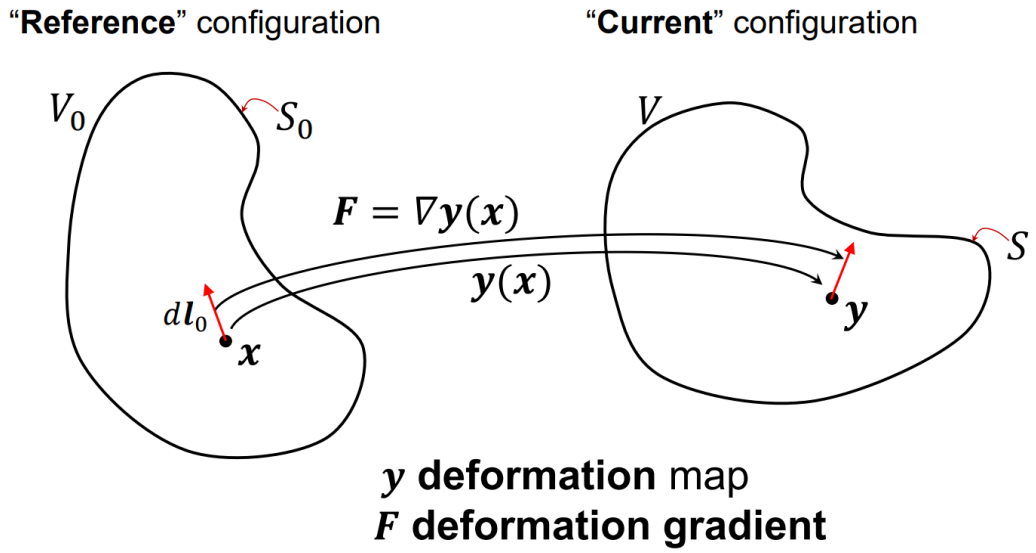

Figure 2.2: Sketch of the deformation process [4].

2.1.3 Constitutive model

The Saint-Venant model is a hyperelastic material model, where hyperelastic indicates that the constitutive model is derived from the Helmholtz free energy density ψ. This Helmholtz free energy depends on F as $\psi = \psi\left(\boldsymbol{F}\right)$. For the derivation of the constitutive model, objectivity of the Helmholtz free energy is required, meaning that it does not change under rigid-body rotations. To obey objectivity, ψ depends on the kinematic variable $\boldsymbol{F}$ through the right Cauchy-Green tensor $\boldsymbol{C}$ like $\psi = \psi\left(\boldsymbol{C}\right)$. The constitutive equations must obey thermodynamic restrictions and should not violate the second law of thermodynamics. Therefore, the reduced Clausius-Duhem inequality should be satisfied. This Clausius-Duhem inequality reads:

$$\int_{v_0} \frac{\mathrm{d}\psi}{\mathrm{d}t}\,\mathrm{d}V_0 - P^{ext}(\dot{\boldsymbol{y}}) \leq 0 \qquad \forall \dot{\boldsymbol{y}}, v_0 \tag{2.5}$$

where t is the time, v_0 is a part of the volume of the body, V_0 is the total volume of the body, P^{ext} is the external power and $\dot{\boldsymbol{y}}$ is the actual deformation rate where the dot is a time derivative.

The principle of virtual work can be used to change the external power to an internal power that depends on the time derivative of the deformation gradient:

$$P^{ext}(\dot{\boldsymbol{y}}) = P^{int}(\dot{\boldsymbol{F}}) \tag{2.6}$$

The expressions for the external and internal work are substituted in Equation 2.6 giving rise to:

$$\int_{v_0} \boldsymbol{b} \cdot \dot{\boldsymbol{y}}\,\mathrm{d}V_0 + \int_{s_0} \boldsymbol{t} \cdot \dot{\boldsymbol{y}}\,\mathrm{d}S_0 = \int_{v_0} \boldsymbol{P} : \dot{\boldsymbol{F}}\,\mathrm{d}V_0 \tag{2.7}$$

where $\boldsymbol{b}$ is the body force, $\boldsymbol{t}$ the traction and s_0 is a part of the surface and S_0 is the entire surface.

Now the external work in Equation 2.5 can be substituted by the internal work, leading to:

$$\int_{v_0} \frac{\mathrm{d}\psi}{\mathrm{d}t}\, \mathrm{d}V_0 - \int_{v_0} \boldsymbol{P} : \dot{\boldsymbol{F}}\, \mathrm{d}V_0 \leq 0 \qquad \forall \dot{\boldsymbol{F}}, v_0 \tag{2.8}$$

Regrouping the terms gives:

$$\int_{v_0} \left(\frac{\mathrm{d}\psi}{\mathrm{d}t} - \int_{v_0} \boldsymbol{P} : \dot{\boldsymbol{F}} \right) \mathrm{d}V_0 \leq 0 \qquad \forall \dot{\boldsymbol{F}}, v_0 \tag{2.9}$$

and the integral can be dropped:

$$\frac{\mathrm{d}\psi}{\mathrm{d}t} - \boldsymbol{P} : \dot{\boldsymbol{F}} \leq 0 \qquad \forall \dot{\boldsymbol{F}} \tag{2.10}$$

Then the chain rule is used in the following manner:

$$\frac{\partial \psi}{\partial \boldsymbol{F}} : \dot{\boldsymbol{F}} - \boldsymbol{P} : \dot{\boldsymbol{F}} \leq 0 \qquad \forall \dot{\boldsymbol{F}} \tag{2.11}$$

and the following inequality is obtained:

$$\left(\frac{\partial \psi}{\partial \boldsymbol{F}} - \boldsymbol{P} \right) : \dot{\boldsymbol{F}} \leq 0 \qquad \forall \dot{\boldsymbol{F}} \tag{2.12}$$

From this inequality, it can be concluded that the first Piola-Kirchhoff stress reads:

$$\boldsymbol{P} = \frac{\partial \psi}{\partial \boldsymbol{F}} = 2\boldsymbol{F} \cdot \frac{\partial \psi}{\partial \boldsymbol{C}} \tag{2.13}$$

Here, the chain rule was used, as well as the definition of the right Cauchy-Green tensor $\boldsymbol{C}$ in Equation 2.2 in this way:

$$\begin{aligned} \frac{\partial \psi}{\partial \boldsymbol{F}} &= \frac{\partial \psi}{\partial \boldsymbol{C}} : \frac{\partial \boldsymbol{C}}{\boldsymbol{F}} = \frac{\partial \psi}{\partial \boldsymbol{C}} \frac{\partial \boldsymbol{F}^T \cdot \boldsymbol{F}}{\partial \boldsymbol{F}} \\ &= \frac{\partial \psi}{\partial \boldsymbol{C}} : \left(\frac{\partial \boldsymbol{F}^T}{\partial \boldsymbol{F}} : \boldsymbol{F} + \boldsymbol{F}^T : \frac{\partial \boldsymbol{F}}{\partial \boldsymbol{F}} \right) \\ &= \frac{\partial \psi}{\partial \boldsymbol{C}} : \left(\mathbb{I}^{LT} : \boldsymbol{F} + \boldsymbol{F}^T : \mathbb{I} \right) = 2\boldsymbol{F} \cdot \frac{\partial \psi}{\partial \boldsymbol{C}} \end{aligned}$$

where $\mathbb{I}$ is the fourth order identity tensor and LT indicates the left transpose. Furthermore, $\boldsymbol{S}$ can be obtained by combining Equation 2.4 with Equation 2.13 resulting in the following constitutive restriction:

$$\boldsymbol{S} = \boldsymbol{F}^{-1} \cdot 2\boldsymbol{F} \cdot \frac{\partial \psi}{\partial \boldsymbol{C}} = 2\frac{\partial \psi}{\partial \boldsymbol{C}} = 2\frac{\partial \psi}{\partial \boldsymbol{E}} : \frac{\partial \boldsymbol{E}}{\partial \boldsymbol{C}} = \frac{\partial \psi}{\partial \boldsymbol{E}} \tag{2.14}$$

where again the chain rule is used together with the fact that $\frac{\partial \boldsymbol{E}}{\partial \boldsymbol{C}} = \frac{1}{2}$ according to the definition of the Green-Lagrange strain $\boldsymbol{E}$ in Equation 2.3.

The Helmholtz free energy in the case of the Saint-Venant model is given by:

$$\psi(\boldsymbol{C}) = \frac{1}{2}\boldsymbol{E} : \mathbb{C} : \boldsymbol{E} \tag{2.15}$$

where $\mathbb{C}$ is the fourth order elasticity tensor. Eventually, by substituting Equation 2.15 into Equation 2.14 and performing the derivative, the following constitutive equation is obtained:

$$\boldsymbol{S} = \mathbb{C} : \boldsymbol{E} \tag{2.16}$$

2.2 Isotropic elastoplasticity material model

Material models for elastoplasticity do not only account for elasticity, but also the complex trajectory after the yield point in the stress-strain curve of Figure 1.2.

2.2.1 Mechanism

The total deformation of elastoplastic materials, like many metals, can be divided into elastic and plastic deformations. Plastic deformation is the result of sliding atoms in a crystal lattice. In Figure 2.3, an example of pure plastic deformation is shown, during which the lattice is unchanged but atoms did slide permanently even after removing the external boundary condition [2].

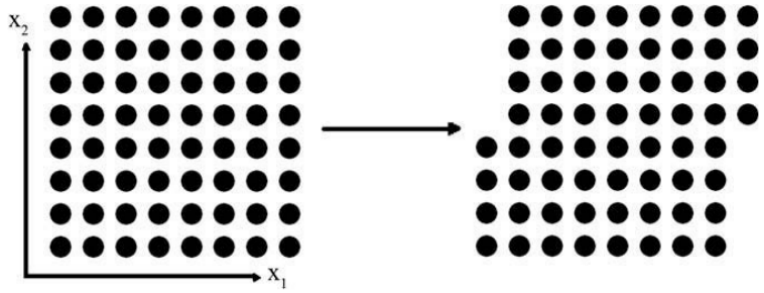

Figure 2.3: Example of pure dislocation deformation [2].

Individual crystals inside a metal can induce certain plastic anisotropy, but in conventional material models for elastoplasticity this anisotropic plastic behaviour is averaged out, resulting in isotropic plasticity. This anisotropic plastic behaviour is averaged out because of the many randomly oriented crystals at the macroscale. However, there are material models that do account for macroscopic plastic anisotropy due to the microsctructure, but still by homogenising the effect of single crystals.

2.2.2 Kinematics

Modelling the deformation of elastoplastic materials requires decomposing the total deformation gradient $\boldsymbol{F}$ into an elastic deformation gradient $\boldsymbol{F}_e$ and a plastic deformation gradient $\boldsymbol{F}_p$. This can be done in a multiplicative manner as follows [5–7]:

$$\boldsymbol{F} = \boldsymbol{F}_e \cdot \boldsymbol{F}_p \tag{2.17}$$

Decomposing the deformation gradient in this way is also referred to as the Kröner-Lee decomposition. The elastic part of the total deformation is reversible and does not depend on its history. The plastic part of the total deformation, however, is irreversible and history-dependent. Therefore the total deformation process is modelled using a sequence of two deformations, namely the transformation of the reference configuration to the intermediate configuration due to plastic deformation and subsequently the deformation of the intermediate configuration to the current configuration due to elastic deformation. If $\boldsymbol{x}$, $\boldsymbol{z}$ and $\boldsymbol{y}$ are material points in the reference, intermediate and current configurations, respectively, then the plastic and elastic deformations gradients read:

$$\boldsymbol{F}_p = \nabla_x \boldsymbol{z} \tag{2.18a}$$

$$\boldsymbol{F}_e = \nabla_z \boldsymbol{y} \tag{2.18b}$$

The sequence of these deformation steps is depicted schematically in Figure 2.4.

Since $\boldsymbol{F}_p$ is history-dependent, it should be known how it changes in time if one wants to model it. Therefore the plastic velocity gradient $\boldsymbol{L}_p$ is introduced as $\boldsymbol{F}_p$ evolves according to this quantity. It is defined as follows:

$$\boldsymbol{L}_p = \dot{\boldsymbol{F}}_p \cdot \boldsymbol{F}_p^{-1} \tag{2.19}$$

In the case of isotropic plasticity, $\boldsymbol{L}_p$ can be specified as this flow rule:

$$\boldsymbol{L}_p = \dot{\lambda} \boldsymbol{r} \left(\bar{\boldsymbol{M}}^d \right) \tag{2.20}$$

where $\dot{\lambda}$ is the equivalent plastic strain rate and $\boldsymbol{r}$ is the flow direction, which is a function of the Mandel stress, which will be defined later. The bar indicates that the quantity is acting on the intermediate configuration.

For further use, the elastic right Cauchy-Green tensor and elastic Green-Lagrange strain tensors are defined as, respectively:

$$\boldsymbol{C_e} = \boldsymbol{F}_e^T \cdot \boldsymbol{F}_e \tag{2.21a}$$

$$\boldsymbol{E_e} = \frac{1}{2}\left(\boldsymbol{C_e} - \boldsymbol{I}\right) \tag{2.21b}$$

In addition, the second Piola-Kirchhoff stress tensor $\bar{\boldsymbol{S}}$ in the intermediate configuration reads:

$$\begin{aligned}\bar{\boldsymbol{S}} &= \boldsymbol{F}_e^{-1} \cdot \boldsymbol{P} \cdot \boldsymbol{F}_p^T \\ &= \boldsymbol{F}_e^{-1} \cdot \boldsymbol{F} \cdot \boldsymbol{S} \cdot \boldsymbol{F}_p^T \\ &= \boldsymbol{F}_p \cdot \boldsymbol{S} \cdot \boldsymbol{F}_p^T\end{aligned} \tag{2.22}$$

by using the fact that $\boldsymbol{P} = \boldsymbol{F} \cdot \boldsymbol{S}$. The cauchy stress $\boldsymbol{\sigma}$ can be obtained according to:

$$\boldsymbol{\sigma} = \frac{1}{\det\left(\boldsymbol{F}\right)} \boldsymbol{P} \cdot \boldsymbol{F}^T \tag{2.23}$$

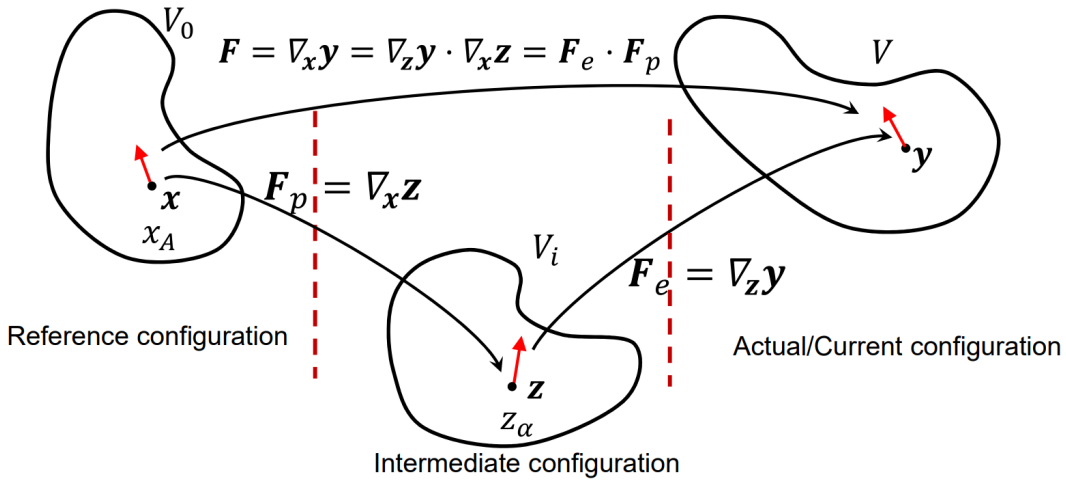

Figure 2.4: Sketch of the deformation process accounting for plasticity with an additional intermediate (purely plastically deformed) configuration [4].

2.2.3 Constitutive model

As in the previous section, the Helmholtz free energy is defined as a function that depends solely on the elastic part of the deformation gradient: $\psi = \psi\left(\boldsymbol{F} \cdot \boldsymbol{F}_p^{-1}\right) = \psi\left(\boldsymbol{F}_e\right)$. This means that the inequality in Equation 2.12 can be rewritten using the multiplicative decomposition of Equation 2.17 into:

$$\left(\frac{\partial \psi}{\partial \boldsymbol{F}_e} - \boldsymbol{P} \cdot \boldsymbol{F}_p^T\right) : \dot{\boldsymbol{F}}_e - \boldsymbol{P} : \boldsymbol{F}_e \cdot \dot{\boldsymbol{F}}_p \leq 0 \qquad \forall \dot{\boldsymbol{F}}_e \tag{2.24}$$

where $\dot{\boldsymbol{F}}_p$ is consistent with the flow rule in Equation 2.20 and is therefore not arbitrary.

This inequality should hold for arbitrary $\dot{\boldsymbol{F}}_e$, which means that the term inside the parentheses must be zero. This gives rise to the following constitutive restriction:

$$\boldsymbol{P} = \frac{\partial \psi}{\partial \boldsymbol{F}_e} \cdot \boldsymbol{F}_p^{-T} \tag{2.25}$$

Consequently, the constitutive restriction yields the following equation for the dissipation:

$$D = \boldsymbol{P} : \boldsymbol{F}_e \cdot \dot{\boldsymbol{F}}_p \geq 0 \tag{2.26}$$

which can be rewritten as:

$$D = \left(\boldsymbol{C}_e \cdot \bar{\boldsymbol{S}}\right) : \boldsymbol{L}_p \geq 0 \tag{2.27}$$

where $\bar{\boldsymbol{M}}$ is the Mandel stress. This stress is work-conjugated with $\boldsymbol{L}_p$ and is defined as:

$$\bar{\boldsymbol{M}} = \boldsymbol{C}_e \cdot \bar{\boldsymbol{S}} \tag{2.28}$$

Substituting the flow rule of Equation 2.20 into Equation 2.27 gives the following restriction on $\boldsymbol{r}$:

$$\bar{\boldsymbol{M}} : \boldsymbol{r}(\bar{\boldsymbol{M}}) \geq 0 \qquad \forall \bar{\boldsymbol{M}} \tag{2.29}$$

because $\dot{\lambda}$ is non-negative.

The time-dependent plastic strain rate that is used in the flow rule depends on the Mandel stress and can be calculated like this:

$$\frac{\dot{\lambda}}{\dot{\lambda}_0} = \left(\frac{\bar{M}_{eq}^d}{\bar{M}_Y}\right)^{\frac{1}{m}} \tag{2.30}$$

where m is a strain rate sensitivity parameter, $\bar{M}_Y$ is the yield stress and $\bar{M}_{eq}^d$ is the equivalent Mandel stress:

$$\bar{M}_{eq}^d = \sqrt{\frac{3}{2}\bar{\boldsymbol{M}}^d : \bar{\boldsymbol{M}}^d} \tag{2.31}$$

$\bar{\boldsymbol{M}}^d$ indicates the deviatoric Mandel stress, which can be computed using the next equation:

$$\bar{\boldsymbol{M}}^d = \bar{\boldsymbol{M}} - \frac{1}{3}\text{tr}\left(\bar{\boldsymbol{M}}\right) \tag{2.32}$$

Both the deviatoric and equivalent Mandel stress can be used to calculate the flow direction:

$$\boldsymbol{r} = \sqrt{\frac{3}{2}}\frac{\bar{\boldsymbol{M}}^d}{\bar{M}_{eq}^d} \tag{2.33}$$

The evolution of the yield stress $\bar{M}_y$ can be taken as this form [8]:

$$\dot{\bar{M}}_y = h\dot{\lambda} \tag{2.34}$$

where $\bar{M}_y(t=0) = \bar{M}_0$ (the initial yield stress) and h is the hardening modulus, which follows:

$$h = h_{eq,0}\left(1 - \frac{\bar{M}_y}{\bar{M}_{y,\infty}}\right)^b \tag{2.35}$$

where $h_{eq,0}$, $\bar{M}_y$ and $\bar{M}_{y,\infty}$ are material parameters.

In the context of metal plasticity, the largest part of the deformation is due to the motion of dislocations. The elastic deformations will be small and therefore the Saint-Venant model can be utilised. Since the transformation from the intermediate configuration to the current configuration is described by elasticity, the model is defined in the current configuration, which means that also $\psi = \psi(\boldsymbol{C}_e)$.

In order to determine the constitutive equation of $\bar{\boldsymbol{S}}$, the restriction for the first Piola-Kirchhoff stress $\boldsymbol{P}$ in Equation 2.25 is taken and rewritten as follows:

$$\boldsymbol{P} = \frac{\partial \psi}{\partial \boldsymbol{F}_e} \cdot \boldsymbol{F}_p^{-T} = 2\boldsymbol{F}_e \cdot \frac{\partial \psi}{\partial \boldsymbol{C}_e} \cdot \boldsymbol{F}_p^{-T} \tag{2.36}$$

This restriction can be plugged into the definition of the second Piola-Kirchhoff stress $\bar{\boldsymbol{S}}$ in Equation 2.22, which yields:

$$\bar{\boldsymbol{S}} = \boldsymbol{F}_e^{-1} \cdot \boldsymbol{P} \cdot \boldsymbol{F}_p^T = 2\frac{\partial \psi}{\partial \boldsymbol{C}_e} = \frac{\partial \psi}{\partial \boldsymbol{E}_e} \tag{2.37}$$

Eventually, the elastic description is obtained by using the following Helmholtz free energy:

$$\psi = \frac{1}{2}\boldsymbol{E}_e : \mathbb{C} : \boldsymbol{E}_e \tag{2.38}$$

and reads [4]:

$$\bar{\boldsymbol{S}} = \mathbb{C} : \boldsymbol{E}_e \tag{2.39}$$

2.3 Crystal plasticity material model

Within the crystal plasticity framework, individual crystals are tracked and plastic anisotropy induced by these crystals are all taken into account.

2.3.1 Mechanism

Sliding of atoms in the crystal lattice during plastic deformation is accommodated by the slip of dislocations through slip systems. These slip systems depend on the crystal structure, e.g. body-centered cubic (BCC), face-centered cubic (FCC) and hexagonal closed-packed (HCP). Consequently, plastic deformation depends largely on the crystallographic orientation with respect to the applied load. At the microscale, there is a small number of crystals present and the plastic response is highly anisotropic. At the macroscale, however, this anisotropy is averaged out because of the large number of crystals with random orientations.

Each slip system comprises a slip direction and a slip plane. Miller indices are used to define crystallographic slip directions and planes. Slip direction $\boldsymbol{s}^\alpha$ of slip system α is identified as $[abc]$ whereas $\langle abc \rangle$ denotes a family of directions. The slip planes are specified by their slip plane normal $\boldsymbol{n}^\alpha$. In a similar manner as for the slip directions, the planes are denoted by (abc) for a slip plane and $\{abc\}$ for a family of planes. The shorthand notation for slip systems is $[abc](abc)$. One of the 12 slip systems of an FCC crystal is shown in Figure 2.5.

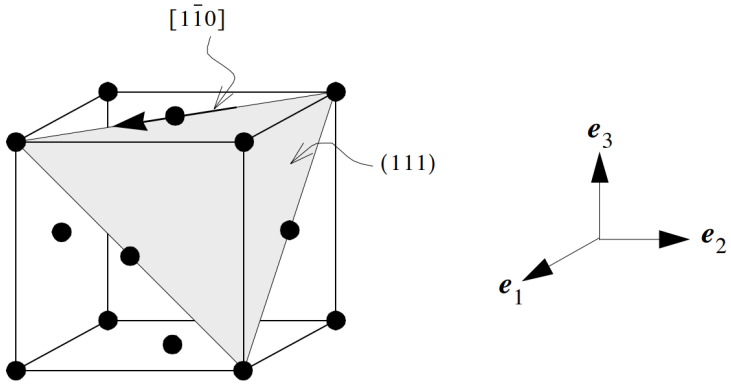

Figure 2.5: One of the 12 slip systems for an FCC crystal in its unit cell. The slip plane and slip direction are indicated [9].

Dislocations start to move once a critical resolved shear stress is reached. For the case of a material being subjected to uniaxial tension, as depicted schematically in Figure 2.6, the shear stress resolved on the slip system acting parallel to the slip direction can be calculated from the applied stress σ according to Schmid's law for uniaxial tension [10]:

$$\tau = \sigma \cos(\lambda) \cos(\phi) \tag{2.40}$$

where λ is the angle between the slip and loading directions and ϕ is the angle between the slip plane normal and loading direction. The factor consisting of these cosines is called the Schmid factor.

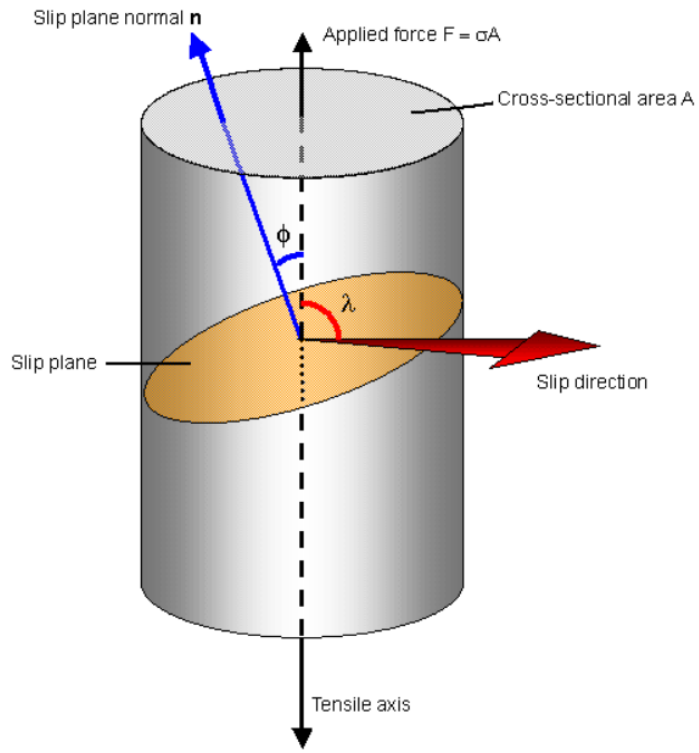

Figure 2.6: Illustration of Schmid's law for one slip system undergoing uniaxial tension [11].

2.3.2 Kinematics

The same multiplicative deformation gradient decomposition is adopted to represent the kinematics of elastoplastic materials when crystal plasticity is taken into account, which is repeated here for convenience:

$$\boldsymbol{F} = \boldsymbol{F}_e \cdot \boldsymbol{F}_p \tag{2.41}$$

In Figure 2.7, a schematic of the deformation process is given where the blue lines indicate a slip system in the three configurations.

Both the elastic and plastic deformation gradients can be expressed as sums of the second order identity tensor and the second order elastic and plastic distortion tensors $\boldsymbol{\beta}_e$ and $\boldsymbol{\beta}_p$, respectively, in the following way:

$$\boldsymbol{F}_e = \boldsymbol{I} + \boldsymbol{\beta}_e \tag{2.42a}$$

$$\boldsymbol{F}_p = \boldsymbol{I} + \boldsymbol{\beta}_p \tag{2.42b}$$

When denoting the dislocation deformation due to the kth slip event as $\boldsymbol{F}_p^{(k)}$, the multiplicative decomposition of the plastic deformation gradient due to n successive events reads [2]:

$$\boldsymbol{F}_p = \boldsymbol{F}_p^{(n)} \boldsymbol{F}_p^{(n-1)} ... \boldsymbol{F}_p^{(1)} \tag{2.43}$$

which would mean that the order of dislocation deformation matters. However, since individual dislocation deformations are generally small, this order can be neglected, unless the atomistic scale is considered. This can be visualised by substituting the distortion representation of the plastic deformation gradient of each dislocation deformation into the multiplicative decomposition of the total plastic deformation gradient, yielding:

$$\boldsymbol{F}_p = \boldsymbol{I} + \sum_{k=1}^{n} \boldsymbol{\beta}_p^{(k)} + \mathcal{O}(\boldsymbol{\beta}_p^2) + \mathcal{O}(\boldsymbol{\beta}_p^3) + ... \approx \boldsymbol{I} + \sum_{k=1}^{n} \boldsymbol{\beta}_p^{(k)} \tag{2.44}$$

where only the linear terms remain if the smaller higher order terms are neglected, meaning that the order is not relevant at the scale of single crystals.

The expression for the plastic velocity gradient, however, differs from the one in the previous section. It was suggested by Rice [12] and is given by:

$$\boldsymbol{L}_p = \sum_{\alpha=1}^{N} \dot{\gamma}^{\alpha} \boldsymbol{s}^{\alpha} \otimes \boldsymbol{n}^{\alpha} = \sum_{\alpha=1}^{N} \dot{\gamma}^{\alpha} \boldsymbol{P}_0^{\alpha} \tag{2.45}$$

where $\boldsymbol{P}_0^{\alpha}$ is the Schmid tensor and $\dot{\gamma}^{\alpha}$ is the plastic slip rate of slip system α and N is the number of slip systems.

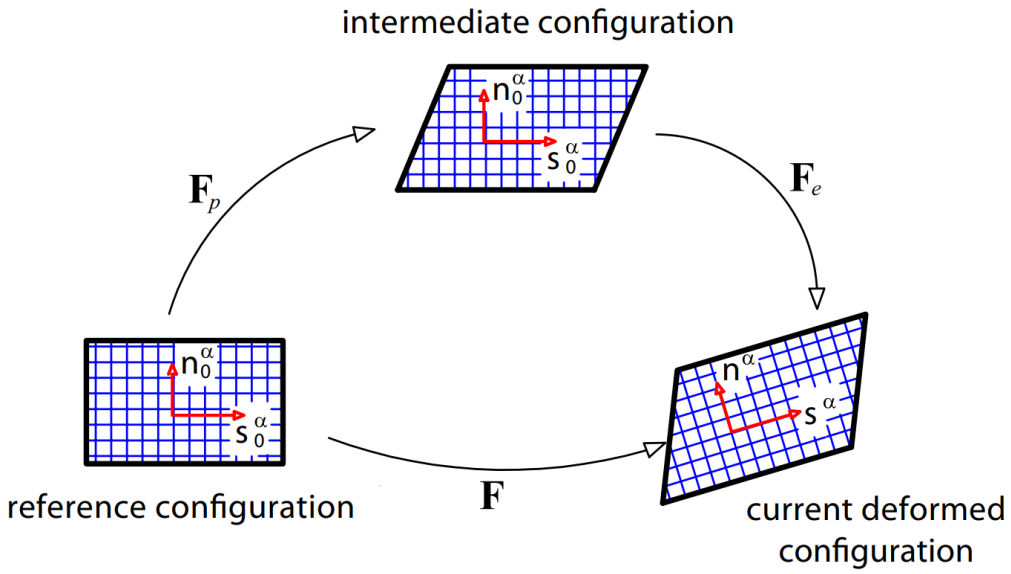

Figure 2.7: Sketch of the deformation process for the crystal plasticity case [4].

2.3.3 Constitutive model

To derive the dissipation inequality for this case, the same procedure can be followed as for the conventional elastoplasticity. This procedure led to the following dissipation:

$$D = \left(\boldsymbol{C}_e \cdot \bar{\boldsymbol{S}}\right) : \boldsymbol{L}_p \geq 0 \tag{2.46}$$

However, since the expression of the plastic velocity gradient $\boldsymbol{L}_p$ differs, also the dissipation differs from this point. Using the crystal plasticity formulation of $\boldsymbol{L}_p$, together with the definition of the Mandel stress, the following dissipation relation is obtained:

$$D = \sum_{\alpha=1}^{N} \dot{\gamma}^{\alpha} \bar{\boldsymbol{M}} : \boldsymbol{P}_0^{\alpha} \geq 0 \tag{2.47}$$

which takes this form:

$$D = \sum_{\alpha=1}^{N} \dot{\gamma}^{\alpha} \tau^{\alpha} \geq 0 \tag{2.48}$$

when using the definition of the resolved shear stress on slip system α:

$$\tau^{\alpha} = \bar{\boldsymbol{M}} : \boldsymbol{P}_0^{\alpha} \tag{2.49}$$

which is the general form of Schmid's law. The plastic slip rate $\dot{\gamma}^{\alpha}$ depends on τ^{α} via the following law [2, 13, 14]:

$$\dot{\gamma}^{\alpha} = \dot{\gamma}_0 \left| \frac{\tau^{\alpha}}{s^{\alpha}} \right|^{\frac{1}{m}} \operatorname{sign}\left(\tau^{\alpha}\right) \tag{2.50}$$

where $\dot{\gamma}_0$ is a reference slip rate and s^{α} is the slip resistance, which is defined by [15]:

$$\dot{s}^{\alpha} = \sum_{\beta=1}^{N} h^{\alpha\beta} \left| \dot{\gamma}^{\beta} \right| \tag{2.51}$$

where $h^{\alpha\beta}$ is a hardening matrix which is given by:

$$h^{\alpha\beta} = h_0 \left(1 - \frac{s^\alpha}{s_\infty}\right)^a q^{\alpha\beta} \tag{2.52}$$

with h_0, s_∞ and a being material parameters and $q^{\alpha\beta}$ being a matrix that contains ones on the diagonal and q_n off-diagonal. This q_n is the ratio of latent hardening with respect to the self-hardening for non-coplanar slip systems [15].

The constitutive relation for $\bar{\boldsymbol{S}}$ is the same as in the previous section since the Saint-Venant model can be used for the elasticity in this case as well:

$$\bar{\boldsymbol{S}} = \mathbb{C} : \boldsymbol{E}_e \tag{2.53}$$

2.4 Inclusions

Various types of inclusions can be present in alloys, which are particles of different chemical composition than the alloy itself. These inclusions can be put in the material on purpose, such as hardening precipitates ($\leq$ 10 nm) or dispersoids ($\approx$ 100 nm) that control the grain size in aluminium alloys. However, unwanted inclusions arise as well in the same aluminium alloys in the form of coarse intermetallics ($\geq$ 0.5 μm) [16, 17].

An important group of inclusions in low-carbon steels are carbide precipitates. Low-carbon steels are mainly iron and carbon alloys, where carbon plays the role of increasing the strength. Carbon atoms, however, are practically insoluble in BCC iron at room temperature. As a consequence, the microstructure of low-carbon steels is characterised by low-carbon BCC ferrite and carbide precipitates (Fe_3C or cementite) that take up the excess carbon that cannot be dissolved into the ferrite [18]. In Figure 2.8, a reflected light microscopy image of a low-carbon steel with carbides can be observed.

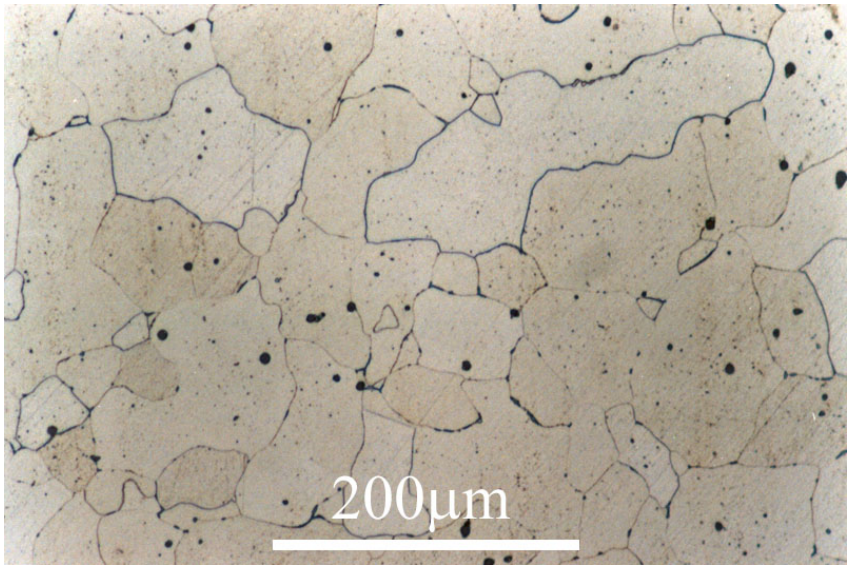

Figure 2.8: Reflected light microscopy image of low-carbon steel with carbides [19].

2.4.1 Properties

Since the chemical composition of the inclusion is different compared to the metal, the properties differ too. The elastic field at the local and global scale is disturbed because of the presence of inclusions in the material due to differences in elastic moduli. Consequently, the mechanical properties of the whole material are altered. Inclusions are being used as reinforcements inside a matrix of composite material in order to obtain better properties. It would not have been possible to achieve these properties with completely homogeneous materials. However, the unintentionally formed inclusions, such as oxides, carbides and voids, during the manufacturing process of steel, frequently act as origins of stress concentrations. This could potentially lead to the nucleation and growth of cracks, affecting the performance of the material or even lead to complete failure [20].

2.4.2 Mechanics

Eshelby [21, 22] calculated the stress field of an ellipsoidal inclusion in dilute cases, meaning that the inclusion can be considered to live inside an infinite matrix, by using the equivalent inclusion method (EIM). This method involves replacing the inclusion with inhomogeneous properties (with different elastic moduli compared to the matrix) with one with the stiffness of the matrix, but with an appropriate eigenstrain as depicted in Figure 2.9.

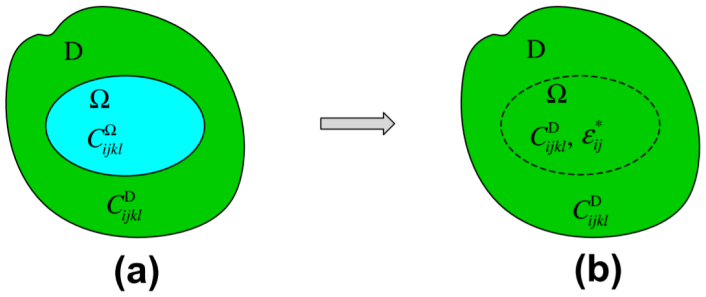

Figure 2.9: Matrix with (a) inhomogeneous inclusion and (b) homogeneous inclusion with appropriate eigenstrain [20].

If the inclusion is inhomogeneous and has different elastic moduli, the following problem has to be solved:

$$\sigma_{ij}(\underline{x}) = \begin{cases} C^I_{ijkl}\varepsilon_{kl}(\underline{x}) & \underline{x} \in V_I \\ \\ C^M_{ijkl}\varepsilon_{kl}(\underline{x}) & \underline{x} \in V_M \end{cases} \tag{2.54}$$

where index notation is used. $\underline{x}$ is the position and the superscripts I and M denote the inclusion and the matrix.

When a uniform strain ε^A_{ij} is applied, the inclusion changes shape by this strain:

$$\varepsilon^I_{ij} = \varepsilon^A_{ij} + \Delta\varepsilon_{ij} \qquad \underline{x} \in V_I \tag{2.55}$$

where $\Delta\varepsilon_{ij}$ is an extra unknown strain due to the fact that $\mathbb{C}^I \neq \mathbb{C}^M$ and depends on the shape of the inclusion, $\varepsilon^A_{ij}, \mathbb{C}^I$ and $\mathbb{C}^M$. The stress inside the inclusion equals:

$$\sigma^I_{ij} = C^I_{ijkl}(\varepsilon^A_{kl} + \Delta\varepsilon_{kl}) \tag{2.56}$$

Eshelby's theory states that the real inclusion with $\mathbb{C}^I$ should be replaced by a homogeneous inclusion having $\mathbb{C}^M$ with a fictitious eigenstrain ε^*_{ij}. ε^*_{ij} is chosen such that:

1. Deformed shape of homogeneous inclusion = shape of real inclusion
2. Stress inside homogeneous inclusion = stress inside real inclusion

So, ε^*_{ij} is chosen such that the homogeneous inclusion does exactly fit inside the deformed shape of the real inclusion and has the same stress. In this way, the same stress and displacement are present at the interface ensuring the same stress and displacement outside the inclusion.

The extra distortion strain $\Delta\varepsilon_{ij}$ is obtained through the Eshelby tensor S_{ijkl} such that:

$$\Delta\varepsilon_{ij} = S_{ijkl}\varepsilon^*_{kl} \tag{2.57}$$

The following statement is required to get the same stress in the inclusions:

$$\underbrace{C^I_{ijkl}(\varepsilon^A_{kl} + \Delta\varepsilon_{kl})}_{\text{real stress}} = \underbrace{C^M_{ijkl}(\varepsilon^A_{kl} + \Delta\varepsilon_{kl} - \varepsilon^*_{kl})}_{\text{stress in homogeneous inclusion with eigenstrain } \varepsilon^*_{kl}} \tag{2.58}$$

The eigenstrain and the stress are obtained by combining Equation 2.57 and Equation 2.58.

$$\boldsymbol{\varepsilon}^* = \left[(\mathbb{C}^I - \mathbb{C}^M)\mathbb{S} + \mathbb{C}^M\right]^{-1}(\mathbb{C}^M - \mathbb{C}^I)\boldsymbol{\varepsilon}^A \tag{2.59}$$

$$\boldsymbol{\sigma}^I = \mathbb{C}^M\left[\boldsymbol{\varepsilon}^A + (\mathbb{S} - \mathbb{I})\boldsymbol{\varepsilon}^*\right] = \boldsymbol{\sigma}^A + \mathbb{C}^M + (\mathbb{S} - \mathbb{I})\boldsymbol{\varepsilon}^* \tag{2.60}$$

2.5 Ductile fracture

Globally, two ways of complete failure of structures can be distinguished: brittle fracture and ductile fracture. Brittle fracture is known for its sudden, rapid failure with little to no plastic deformation during the process. This mechanism is generally unwanted, because of its unpredictability. The ductile fracture mechanism includes a much more gradual failure, during which the cross-sections become thinner and thinner due to large plastic deformation. This fracture mechanism is mostly favoured over brittle fracture. However, it is not always possible to get ductile fracture, because, when designing the material, an increase in fracture toughness often leads to a decrease in strength. In addition, ductile materials can become brittle if the temperature reaches below the ductile-to-brittle transition temperature [23].

In Figure 2.10 one can see the fracture surfaces of fractured specimens that have failed through both mechanisms. One can observe ductile fracture in the left specimen, where much plastic deformation can be observed. Because of the shape of the fracture surfaces, this is also known as *cup-and-cone* fracture. The right specimen consists of a brittle material that has fractured rapidly. No ductile deformation can be observed here.

Brittle fracture is described quite well by the theory of linear elastic fracture mechanics (LEFM), but this theory will not be described in this report. In the following subsections, however, the ductile fracture mechanism is explained.

Figure 2.10: (a) Ductile *cup-and-cone* fracture in aluminium and (b) brittle fracture in mild steel [24].

2.5.1 Mechanism

The mechanism of ductile fracture is substantially different from brittle fracture with very small plastic deformation. Whereas brittle fracture involves a rapid crack propagating through the material, the ductile fracture process contains more stages. These stages are shown in a schematic way in Figure 2.11. In the first figure, impurities or inclusions present inside a ductile material matrix can be observed. When a stress is applied to the matrix, void nucleation starts taking place near the inclusions. Thereafter nucleated voids start to grow and strain localisation between voids is induced. Then necking between voids occurs and eventually there is void coalescence and the material fractures.

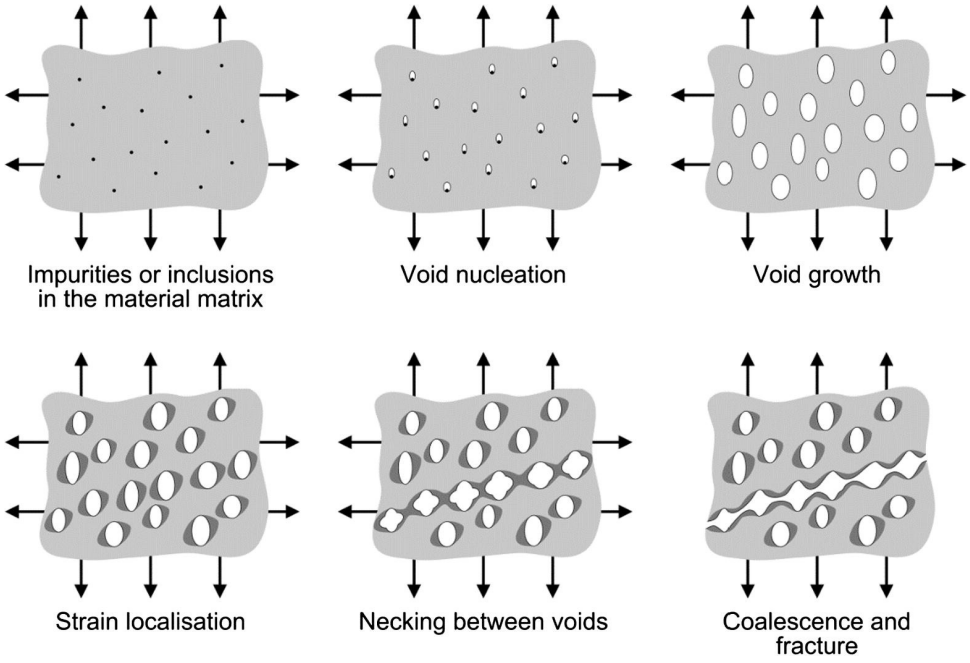

Figure 2.11: Ductile fracture mechanism [25].

Nucleation of voids can be caused by two processes: inclusions debonding from the matrix or cracking of the inclusion itself [26–28]. Whether an inclusion debonds or cracks depends on the shape and size, as well as the loading direction with respect to the inclusion. In Figure 2.12, scanning electron microscopy (SEM) images of both cases can be viewed. Marteleur et al. [29] found that inclusions cracked when the load was applied in the longitudinal direction with respect to the inclusion and that the inclusions debonded when the load was applied in the transversal direction. Goods and Brown [26] found that equiaxed inclusions generally debond, while irregularly shaped particles with high aspect ratio fracture internally. Also, it was established that larger inclusions debond earlier than small inclusions, which rather crack. Furthermore, they found that debonding starts at the poles of the inclusions, meaning at two opposite sites on the edge of the inclusion.

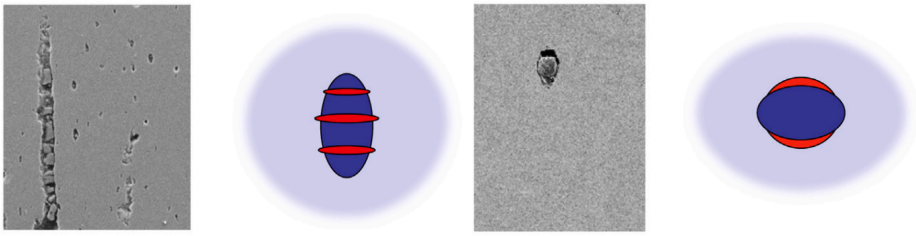

(a) L-specimen (b) T-specimen

Figure 2.12: Void nucleation by (a) inclusion cracking when loaded in the longitudinal direction and (b) inclusion-matrix decohesion when loaded in the transversal direction [29].

2.5.2 Cohesive zone model

COhesive zone modelling is a tool that can be used to model the propagation of a crack. According to LEFM, there is a stress singularity at the tip of a sharp crack. This opening stress σ_{22} is represented by the blue line in Figure 2.13a. In the same figure, also more realistic stress values are plotted as the red line, with finite values at the crack tip. Barenblatt [30] analysed the cohesive tractions between the surfaces of a crack and split it into a cohesive zone region u_c and the rest of the crack length $a - u_c$ where tractions are negligible as shown in Figure 2.13b.

The nonlinear traction-separation relation between two surfaces are described by a cohesive law. An example

of such a cohesive law is shown in Figure 2.13c, where the traction T is plotted versus the separation δ. When surfaces separate and δ increases, also the traction increases until the maximum stress σ_c is reached at a separation δ^*. From this point, the traction decreases until no traction between the interfaces is left and δ_{max} is reached.

For complete separation of two surfaces, an energy of G_c is required, which is defined as:

$$G_c = \int_0^{\delta_{max}} T(\delta) \mathrm{d}\delta \tag{2.61}$$

This expression can also be seen as the area under the traction-separation of Figure 2.13c. For the function of the traction $T(\delta)$ the nonlinear Universal Binding Energy relation can be used:

$$T(\delta) = e \frac{\sigma_c}{\delta^*} \delta e^{-\frac{\delta}{\delta^*}} \tag{2.62}$$

where $\int_0^{\delta_{max}} T(\delta) \mathrm{d}\delta = \gamma_s$ This Universal Binding Energy relation is an exponential function which can be fitted to the properties of the interface.

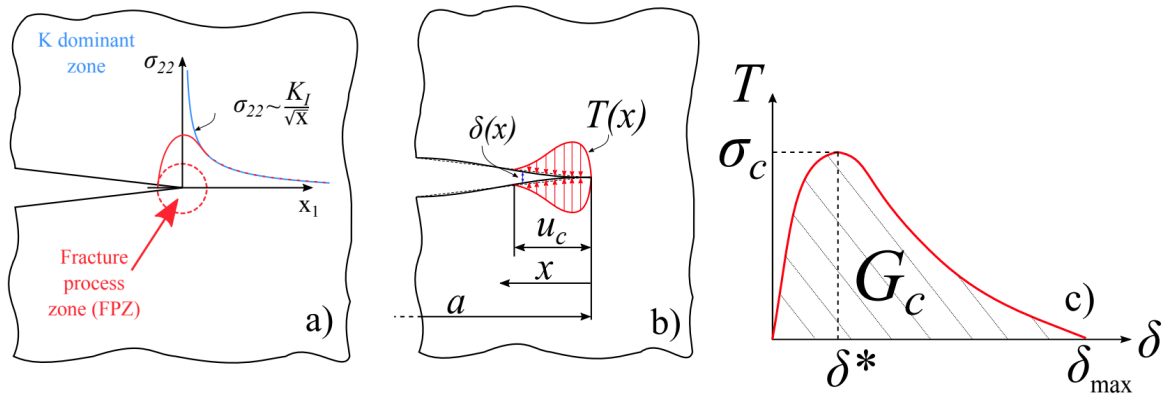

Figure 2.13: a) Stress singularity arising from opening stress σ_{22} computed using LEFM (blue line) together with a more realistic nonlinear stress field (red). b) Cohesive zone with traction T over the length u_c. c) Traction as a function of crack face separation δ. The maximum traction is σ_c at a separation of δ^*. At δ_{max}, the two faces are separated fully and feel no tractions anymore. The area under the curve is the cohesive energy G_c [31].

Tvergaard and Hutchinson [32] analysed the crack growth initiation and subsequent resistance for elastoplastic solids with a traction-separation law. They found that, in elastic perfectly plastic materials i.e. without hardening, debonding can occur when:

$$\sigma_c < \left(\frac{2+\pi}{\sqrt{3}} \right) \sigma_y \approx 2.97 \sigma_y \tag{2.63}$$

Needleman [33] and Xu and Needleman [34] analysed the void nucleation and subsequent void growth of the ductile fracture mechanism using a cohesive zone model together with the finite element method (FEM). The mesh that they considered is shown in Figure 2.14, which allows a circular cylindrical inclusion to debond from a metal matrix. The metal matrices considered were modeled using isotropic plasticity [33] and crystal plasticity [34] material models, where the crystal plasticity model contained three slip systems. Despite the fact that two different material models were used, the results in terms of global stress/strain behaviour and local plastic strain behaviour showed little variations.

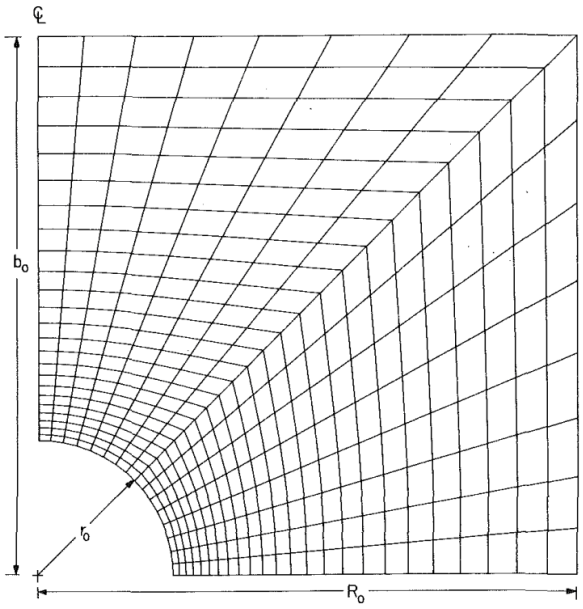

Figure 2.14: FEM mesh used in calculations by Needleman [33].

Chapter 3

Research definition

From the literature review, it can be concluded that void nucleation is an essential part of the ductile fracture mechanism. This void nucleation can occur through cracking of inclusions, as well as debonding of inclusions from a metal matrix.

Metals consist of crystals, which are regular arrangements of atoms according to a lattice. The orientation and atom arrangement of these crystals govern the process of plastic deformation, which is anisotropic at the scale of single crystals. At the scale of micron-sized inclusions, which is in the order of the scale of these single crystals, crystal plastic anisotropy should be taken into account.

Because of crystal plastic anisotropy, the inclusion debonding process differs from those of isotropic elastic or isotropic plastic materials.

3.1 Research goal

Void nucleation has been researched thoroughly, for example by Needleman [33]. He introduced a continuum model for void nucleation by inclusion debonding and described the development from initial debonding to entire separation and successive growth. This research was extended by Xu and Needleman [34], by taking into account the crystallographic nature of metal plasticity. They found little difference between void nucleation predictions based on crystal plasticity and those based on an isotropic theory. However, the research that has been conducted until now, was performed on a 2D simplification of the problem with circular cylindrical inclusions. Also, only three slip systems were considered with no different crystal orientations. Therefore, the complete role of crystal plastic anisotropy on the void nucleation process in a ferrite matrix still remains unclear.

This leads to the following goal of this research: The goal of this research is to establish the effect of crystal plastic anisotropy on the void nucleation process in BCC ferrite. In order to reach this goal, it is useful to pose it as the main research question: **How does crystal plastic anisotropy influence the void nucleation process in BCC ferrite?**

This main research question can be divided into four sub-questions:

1. What are the properties that control void nucleation in elastic materials?
2. What is the role of isotropic plasticity around the inclusion in the void nucleation process?
3. What is the role of plastic anisotropy of the matrix in the void nucleation process?
4. What are the main ingredients that an effective model for void nucleation should incorporate, in order to account for crystal plastic anisotropy?

3.2 Hypothesis

As observed by Marteleur [29] and Goods and Brown [26], it is expected that debonding starts at two sides of the inclusion. Rotation of the crystal orientation could lead to debonding at other locations compared to the debonding sites of isotropic materials. In addition, varying the crystal orientation could make debonding occur at larger or lower applied stress or strain. This would in turn lead to different global stress/strain behaviour. The local stress

and strain fields are expected to contain some asymmetry for the cases of a rotated crystal, compared to symmetric fields for isotropic and unrotated cases. Furthermore, the strain at which an inclusion fully debonds could be altered by varying the crystal orientation.

Chapter 4

Finite element implementation

In this chapter, the finite element implementation that is used to solve the problem at hand is discussed.

4.1 Finite element method

The finite element method (FEM) is an appropriate method for solving differential equations numerically. The differential equation that commonly has to be solved during a solid mechanics problem is the balance of momentum:

$$\text{Div}\boldsymbol{P} + \boldsymbol{b}_0 = 0 \qquad \text{in } V_0 \tag{4.1}$$

where the Div operator indicates the divergence with respect to $\boldsymbol{x}$ and $\boldsymbol{b}_0$ and V_0 are the body forces and volume, respectively, both in the reference configuration. The balance of momentum is also known as the strong form when used in FEM. From this strong form, the deformation of the studied volume can be computed. The strategy of FEM comprises converting the body's volume into multiple smaller body's called *finite elements* (in this research hexahedral 8 node elements) and transforming the strong form into a solvable analytical weak form:

$$\int_{S_0} \boldsymbol{v} \cdot \boldsymbol{t} \, \mathrm{d}S_0 + \int_{V_0} \boldsymbol{v} \cdot \boldsymbol{b}_0 \, \mathrm{d}V_0 = \int_{V_0} \nabla_x \boldsymbol{v} : \boldsymbol{P} \, \mathrm{d}V_0 \tag{4.2}$$

where $\boldsymbol{V} = \delta\boldsymbol{u}$ is an admissible displacement variation, $\boldsymbol{n}_0$ is the normal vector, $\boldsymbol{t}$ is the tractions and S_0 is the reference surface area. This equation is also called the principle of virtual work (PVW), as the left terms are the external virtual work, which are equal to the right term, called the internal virtual work.

$\boldsymbol{P}$ and $\boldsymbol{t}$ are nonlinear functions of the deformation gradient $\boldsymbol{F}$ and $\boldsymbol{b}_0$ is also a function of $\boldsymbol{F}$. To solve this nonlinear equation, the Newton-Raphson method can be applied, which is an iterative root-finding method. Application of the Newton-Raphson method leads to the following linear system of equations:

$$\sum_{m=1}^{N_{el}} \left(\left[\boldsymbol{K}^{(i)}\right]_m [\delta\hat{\boldsymbol{y}}]_m = \left[\hat{\boldsymbol{f}}_{ext}\right]_m - \left[\hat{\boldsymbol{f}}_{int}^{(i)}\right]_m \right) \tag{4.3}$$

where N_{el} is the total number of elements, $\left[\boldsymbol{K}^{(i)}\right]_m$ is the element stiffness matrix at iteration i, $[\delta\hat{\boldsymbol{y}}]_m$ is the per element difference between the nodal deformation at iteration $i+1$ and iteration i, $\left[\hat{\boldsymbol{f}}_{ext}\right]_m$ are the element external forces and $\left[\hat{\boldsymbol{f}}_{int}^{(i)}\right]_m$ are the element internal forces. Assembling the matrices and arrays of all elements yields this complete linear system of equations:

$$\left[\boldsymbol{K}^{(i)}\right] [\delta\hat{\boldsymbol{y}}] = \left[\hat{\boldsymbol{f}}_{ext}\right] - \left[\hat{\boldsymbol{f}}_{int}^{(i)}\right] \tag{4.4}$$

This procedure is followed for each time step in a time-dependent problem. In Appendix A, pseudocodes for the elasticity, plasticity and crystal plasticity material model implementations are given, for the sake of clarity.

4.2 Time integration of plastic velocity gradient

Plasticity and accordingly crystal plasticity are history-dependent processes because the stress depends on the plastic strain rate. Therefore the time should be taken into account for these cases, unlike for purely elastic modelling. It is possible to model the time, by obtaining a plastic deformation gradient at the next time step ($\boldsymbol{F}_{p,n+1}$) that depends on its value of the previous time step ($\boldsymbol{F}_{p,n}$). The expression for this is governed by performing a time integration of the plastic velocity gradient $\boldsymbol{L}_p$:

$$\begin{aligned}\int_{t_n}^{t_{n+1}} \boldsymbol{L}_p(t)\mathrm{d}t &= \int_{t_n}^{t_{n+1}} \dot{\boldsymbol{F}}_p \cdot \boldsymbol{F}_p^{-1}\mathrm{d}t \\ &= \Big[\ln(\boldsymbol{F}_p)\Big]_{t_n}^{t_{n+1}} \\ &= \ln(\boldsymbol{F}_{p,n+1} \cdot \boldsymbol{F}_{p,n}^{-1})\end{aligned} \tag{4.5}$$

where the definition of the plastic velocity gradient is used according to Equation 2.19. The exponential of both sides can be taken according to:

$$\exp\left(\int_{t_n}^{t_{n+1}} \boldsymbol{L}_p(t)\mathrm{d}t\right) = \boldsymbol{F}_{p,n+1} \cdot \boldsymbol{F}_{p,n}^{-1} \tag{4.6}$$

$\boldsymbol{F}_{p,n+1}$ can be isolated in the following manner:

$$\boldsymbol{F}_{p,n+1} = \exp\left(\int_{t_n}^{t_{n+1}} \boldsymbol{L}_p(t)\mathrm{d}t\right) \cdot \boldsymbol{F}_{p,n} \tag{4.7}$$

and the Taylor approximation of an exponential can be used, leading to this expression:

$$\boldsymbol{F}_{p,n+1} = \left(\boldsymbol{I} + \int_{t_n}^{t_{n+1}} \boldsymbol{L}_p(t)\mathrm{d}t\right) \cdot \boldsymbol{F}_{p,n} \tag{4.8}$$

4.2.1 Plasticity

To acquire the specific $\boldsymbol{F}_{p,n+1}$ for the isotropic plasticity case, the corresponding plastic velocity gradient should be considered, which is repeated here for convenience.

$$\boldsymbol{L}_p = \dot{\lambda}\boldsymbol{r}\left(\bar{\boldsymbol{M}}^d\right)$$

Plugging this definition into Equation 4.8 yields:

$$\boldsymbol{F}_{p,n+1} = \left(\boldsymbol{I} + \int_{t_n}^{t_{n+1}} \dot{\lambda}\boldsymbol{r}\left(\bar{\boldsymbol{M}}^d\right)\mathrm{d}t\right) \cdot \boldsymbol{F}_{p,n} = \left(\boldsymbol{I} + \boldsymbol{r}\left(\bar{\boldsymbol{M}}^d\right)\int_{t_n}^{t_{n+1}} \dot{\lambda}\mathrm{d}t\right) \cdot \boldsymbol{F}_{p,n} \tag{4.9}$$

where the forward Euler method is used to evaluate the integral of the plastic strain rate in the previous expression:

$$\int_{t_n}^{t_{n+1}} \dot{\lambda}\mathrm{d}t = \dot{\lambda}_n \Delta t \tag{4.10}$$

where $\Delta t = t_{n+1} - t_n$. This forward Euler method is substituted into Equation 4.9, leading to the final expression:

$$\boldsymbol{F}_{p,n+1} = \left(\boldsymbol{I} + \dot{\lambda}_n\boldsymbol{r}\left(\bar{\boldsymbol{M}}^d\right)\Delta t\right) \cdot \boldsymbol{F}_{p,n} \tag{4.11}$$

4.2.2 Crystal plasticity

For the crystal plasticity case, the following plastic velocity gradient was mentioned in section 2.3:

$$\boldsymbol{L}_p = \sum_{\alpha=1}^{N} \dot{\gamma}^\alpha \boldsymbol{s}^\alpha \otimes \boldsymbol{n}^\alpha = \sum_{\alpha=1}^{N} \dot{\gamma}^\alpha \boldsymbol{P}_0^\alpha$$

Using this version for transforming Equation 4.8 leads to:

$$\boldsymbol{F}_{p,n+1} = \left(\boldsymbol{I} + \int_{t_n}^{t_{n+1}} \sum_{\alpha=1}^{N} \dot{\gamma}^{\alpha} \boldsymbol{P}_0^{\alpha} \mathrm{d}t \right) \cdot \boldsymbol{F}_{p,n} = \left(\boldsymbol{I} + \sum_{\alpha=1}^{N} \boldsymbol{P}_0^{\alpha} \int_{t_n}^{t_{n+1}} \dot{\gamma}^{\alpha} \mathrm{d}t \right) \cdot \boldsymbol{F}_{p,n} \tag{4.12}$$

where again the forward Euler method is used to integrate the plastic slip rate in this case:

$$\int_{t_n}^{t_{n+1}} \dot{\gamma}^{\alpha} \mathrm{d}t = \dot{\gamma}_n^{\alpha} \Delta t \tag{4.13}$$

leading to the following expression for the plastic deformation gradient at the next time step:

$$\boldsymbol{F}_{p,n+1} = \left(\boldsymbol{I} + \Delta t \sum_{\alpha=1}^{N} \dot{\gamma}_n^{\alpha} \boldsymbol{P}_0^{\alpha} \right) \cdot \boldsymbol{F}_{p,n} \tag{4.14}$$

4.3 Analytical tangent stiffness

An important step for calculating tie element stiffness matrix in FEM is the computation of the analytical tangent stiffness. It is computed for each iteration in the Newton-Raphson method, and differs for the case of elasticity, isotropic plasticity and crystal plasticity. Deriving them involves some mathematical steps, which are discussed in this section.

4.3.1 Elasticity

For the case of elasticity, where no time is involved, the derivation is relatively simple. The analytical tangent stiffness can be divided into a geometric stiffness and material stiffness:

$$\mathbb{A}^{(i)} = \left(\frac{\partial \boldsymbol{P}}{\partial \boldsymbol{F}} \right)_{\boldsymbol{F}=\boldsymbol{F}^i} = \mathbb{K}_{geo}^{(i)} + \mathbb{K}_{mat}^{(i)} \tag{4.15}$$

Using the definitions of the Cauchy-Green tensor, Green-Lagrange strain and first Piola-Kirchhoff stress of Equation 2.2, Equation 2.3 and Equation 2.4 together with the fact that $\frac{\partial \boldsymbol{F}}{\partial \boldsymbol{F}} = \mathbb{I}$ and $\frac{\partial \boldsymbol{F}^T}{\partial \boldsymbol{F}} = \mathbb{I}^{LT}$, the following steps can be performed:

$$\begin{aligned}
\mathbb{A} &= \frac{\partial \boldsymbol{P}}{\partial \boldsymbol{F}} && (4.16)\\
&= \frac{\partial \boldsymbol{F}}{\partial \boldsymbol{F}} \odot \boldsymbol{S} + \boldsymbol{F} \cdot \frac{\partial \boldsymbol{S}}{\partial \boldsymbol{F}} && (4.17)\\
&= \mathbb{I} \odot \boldsymbol{S} + \boldsymbol{F} \cdot \mathbb{C} : \frac{\partial \boldsymbol{E}}{\partial \boldsymbol{F}} && (4.18)\\
&= \mathbb{I} \odot \boldsymbol{S} + \frac{1}{2} \boldsymbol{F} \cdot \mathbb{C} : \frac{\partial \left(\boldsymbol{F}^T \cdot \boldsymbol{F} - \boldsymbol{I} \right)}{\partial \boldsymbol{F}} && (4.19)\\
&= \mathbb{I} \odot \boldsymbol{S} + \frac{1}{2} \boldsymbol{F} \cdot \mathbb{C} : \left(\frac{\partial \boldsymbol{F}^T}{\partial \boldsymbol{F}} \odot \boldsymbol{F} + \boldsymbol{F}^T \cdot \frac{\partial \boldsymbol{F}}{\partial \boldsymbol{F}} \right) && (4.20)\\
&= \mathbb{I} \odot \boldsymbol{S} + \frac{1}{2} \boldsymbol{F} \cdot \mathbb{C} : \left(\mathbb{I}^{LT} \odot \boldsymbol{F} + \boldsymbol{F}^T \cdot \mathbb{I} \right) && (4.21)
\end{aligned}$$

where $\odot$ indicates a tensor product where the second index of the first tensor contracts with the first index of the second tensor. The two resulting terms are the geometric and material stiffness according to these two equations:

$$\mathbb{K}_{geo}^{(i)} = \mathbb{I} \odot \boldsymbol{S}^{(i)} \tag{4.22}$$

$$\mathbb{K}_{mat}^{(i)} = \frac{1}{2} \boldsymbol{F}^{(i)} \cdot \mathbb{C} : \left(\mathbb{I}^{LT} \odot \boldsymbol{F}^{(i)} + \boldsymbol{F}^{T(i)} \cdot \mathbb{I} \right) \tag{4.23}$$

4.3.2 Plasticity and crystal plasticity

Deriving the analytical tangent stiffness for the isotropic plasticity and crystal plasticity cases is somewhat more complicated since it involves more partial differential equations (PDEs). The analytical tangent stiffness can again be split into a geometric and material contribution, but as time is involved now, the time step is also indicated:

$$\mathbb{A}_{n+1}^{(i)} = \left(\frac{\partial \boldsymbol{P}}{\partial \boldsymbol{F}}\right)_{\boldsymbol{F}=\boldsymbol{F}_{n+1}^{i}} = \mathbb{K}_{geo}^{(i,n+1)} + \mathbb{K}_{mat}^{(i,n+1)} \tag{4.24}$$

For clarity during the computation, the Newton-Raphson iteration index is removed because it does not change the derivation:

$$\mathbb{A}_{n+1} = \frac{\partial \boldsymbol{P}_{n+1}}{\partial \boldsymbol{F}_{n+1}} = \mathbb{K}_{geo}^{n+1} + \mathbb{K}_{mat}^{n+1} \tag{4.25}$$

The geometric contribution to the analytical tangent stiffness is computed in the exact same way as for the elastic case, only with indication of the time step. Computing the material stiffness, however, involves different steps. Pushing forward the second Piola-Kirchhoff stress in the reference configuration to the intermediate configuration gives rise to three PDEs, indicated by three colours.

$$\mathbb{K}_{geo}^{n+1} = \frac{\partial \boldsymbol{F}_{n+1}}{\partial \boldsymbol{F}_{n+1}} \odot \boldsymbol{S}_{n+1} = \mathbb{I} \odot \boldsymbol{S}_{n+1} \tag{4.26}$$

$$\mathbb{K}_{mat}^{n+1} = \boldsymbol{F}_{n+1} \cdot \frac{\partial \boldsymbol{S}_{n+1}}{\partial \boldsymbol{F}_{n+1}} \tag{4.27}$$

$$= \boldsymbol{F}_{n+1} \cdot \frac{\partial \left(\boldsymbol{F}_{p,n+1}^{-1} \cdot \bar{\boldsymbol{S}}_{n+1} \cdot \boldsymbol{F}_{p,n+1}^{-T}\right)}{\partial \boldsymbol{F}_{n+1}} \tag{4.28}$$

$$= \boldsymbol{F}_{n+1} \cdot \left(\frac{\partial \boldsymbol{F}_{p,n+1}^{-1}}{\partial \boldsymbol{F}_{n+1}} \odot \bar{\boldsymbol{S}}_{n+1} \cdot \boldsymbol{F}_{p,n+1}^{-T} + \boldsymbol{F}_{p,n+1}^{-1} \cdot \frac{\partial \bar{\boldsymbol{S}}_{n+1}}{\partial \boldsymbol{F}_{n+1}} \odot \boldsymbol{F}_{p,n+1}^{-T} + \boldsymbol{F}_{p,n+1}^{-1} \cdot \bar{\boldsymbol{S}}_{n+1} \cdot \frac{\partial \boldsymbol{F}_{p,n+1}^{-T}}{\partial \boldsymbol{F}_{n+1}}\right) \tag{4.29}$$

For the case of isotropic plasticity, the first PDE is equal to the zero tensor, which follows from the fact that the value of the plastic deformation gradient of the next time step solely depends on its value of the current time step:

$$\frac{\partial \boldsymbol{F}_{p,n+1}^{-1}}{\partial \boldsymbol{F}_{n+1}} = \frac{\partial \left(\boldsymbol{F}_{p,n}^{-1} \cdot \left(\boldsymbol{I} - \dot{\lambda}_n \boldsymbol{r} \Delta t\right)\right)}{\partial \boldsymbol{F}_{n+1}} = \boldsymbol{0} \tag{4.30}$$

Similar to the isotropic plasticity case, also the first PDE is the zero tensor because of the same reason:

$$\frac{\partial \boldsymbol{F}_{p,n+1}^{-1}}{\partial \boldsymbol{F}_{n+1}} = \frac{\partial \left(\boldsymbol{F}_{p,n}^{-1} \cdot \left(\boldsymbol{I} - \Delta t \sum_{\alpha=1}^{N} \boldsymbol{P}_0^{\alpha} \dot{\gamma}_n^{\alpha}\right)\right)}{\partial \boldsymbol{F}_{n+1}} = \boldsymbol{0} \tag{4.31}$$

Furthermore, the second PDE can be rewritten by using the multiplicative split of the total deformation gradient into the elastic and plastic parts as follows:

$$\frac{\partial \bar{\boldsymbol{S}}_{n+1}}{\partial \boldsymbol{F}_{n+1}} = \mathbb{C} : \frac{\partial \boldsymbol{E}_{e,n+1}}{\partial \boldsymbol{F}_{n+1}} = \frac{1}{2}\mathbb{C} : \frac{\partial \left(\boldsymbol{C}_{e,n+1} - \boldsymbol{I}\right)}{\partial \boldsymbol{F}_{n+1}} = \frac{1}{2}\mathbb{C} : \frac{\partial \boldsymbol{C}_{e,n+1}}{\partial \boldsymbol{F}_{n+1}} \tag{4.32}$$

$$= \frac{1}{2}\mathbb{C} : \left(\frac{\partial \boldsymbol{F}_{e,n+1}^{T}}{\partial \boldsymbol{F}_{n+1}} \odot \boldsymbol{F}_{e,n+1} + \boldsymbol{F}_{e,n+1}^{T} \cdot \frac{\partial \boldsymbol{F}_{e,n+1}}{\partial \boldsymbol{F}_{n+1}}\right) \tag{4.33}$$

$$= \frac{1}{2}\mathbb{C} : \left(\left[\frac{\partial \boldsymbol{F}_{p,n+1}^{-T}}{\partial \boldsymbol{F}_{n+1}} \odot \boldsymbol{F}_{n+1}^{T} + \boldsymbol{F}_{p,n+1}^{-T} \cdot \frac{\partial \boldsymbol{F}_{n+1}^{T}}{\partial \boldsymbol{F}_{n+1}}\right] \odot \boldsymbol{F}_{e,n+1} + \boldsymbol{F}_{e,n+1}^{T} \cdot \left[\frac{\partial \boldsymbol{F}_{n+1}}{\partial \boldsymbol{F}_{n+1}} \odot \boldsymbol{F}_{p,n+1}^{-1} + \boldsymbol{F}_{n+1} \cdot \frac{\partial \boldsymbol{F}_{p,n+1}^{-1}}{\partial \boldsymbol{F}_{n+1}}\right]\right) \tag{4.34}$$

Then the result of Equation 4.30 and Equation 4.31 are employed, yielding this expression:

$$\frac{\partial \bar{\boldsymbol{S}}_{n+1}}{\partial \boldsymbol{F}_{n+1}} = \frac{1}{2}\mathbb{C} : \left(\boldsymbol{F}_{p,n+1}^{-T} \cdot \mathbb{I}^{LT} \odot \boldsymbol{F}_{e,n+1} + \boldsymbol{F}_{e,n+1}^{T} \cdot \mathbb{I} \odot \boldsymbol{F}_{p,n+1}^{-1}\right) \tag{4.35}$$

Eventually, the final PDE is evaluated and is equal to the zero tensor:

$$\frac{\partial \boldsymbol{F}_{p,n+1}^{-T}}{\partial \boldsymbol{F}_{n+1}} = \left(\frac{\partial \boldsymbol{F}_{p,n+1}^{-1}}{\partial \boldsymbol{F}_{n+1}} \right)^{LT} = \boldsymbol{0} \tag{4.36}$$

Substituting the three results of the PDEs into the material stiffness expression of Equation 4.29 leads to the next equation:

$$\mathbb{K}_{mat}^{n+1} = \frac{1}{2} \boldsymbol{F}_{e,n+1} \cdot \left(\mathbb{C} : \left(\boldsymbol{F}_{p,n+1}^{-T} \cdot \mathbb{I}^{LT} \odot \boldsymbol{F}_{e,n+1} + \boldsymbol{F}_{e,n+1}^{T} \cdot \mathbb{I} \odot \boldsymbol{F}_{p,n+1}^{-1} \right) \right) \odot \boldsymbol{F}_{p,n+1}^{-T} \tag{4.37}$$

with

$$\begin{aligned} \boldsymbol{F}_{e,n+1} &= \boldsymbol{F}_{n+1} \cdot \boldsymbol{F}_{p,n+1}^{-1} \\ \boldsymbol{F}_{e,n+1}^{T} &= \boldsymbol{F}_{p,n+1}^{-T} \cdot \boldsymbol{F}_{n+1}^{T} \end{aligned} \tag{4.38}$$

where for the isotropic plasticity material model:

$$\boldsymbol{F}_{p,n+1}^{-1} = \boldsymbol{F}_{p,n}^{-1} \cdot \left(\boldsymbol{I} - \dot{\lambda}_n \boldsymbol{r} \Delta t \right) \tag{4.39}$$

$$\boldsymbol{F}_{p,n+1}^{-T} = \left(\boldsymbol{I} - \dot{\lambda}_n \boldsymbol{r} \Delta t \right)^{T} \cdot \boldsymbol{F}_{p,n}^{-T} \tag{4.40}$$

and for the crystal plasticity material model:

$$\boldsymbol{F}_{p,n+1}^{-1} = \boldsymbol{F}_{p,n}^{-1} \cdot \left(\boldsymbol{I} - \Delta t \sum_{\alpha=1}^{N} \boldsymbol{P}_0^{\alpha} \dot{\gamma}_n^{\alpha} \right) \tag{4.41}$$

$$\boldsymbol{F}_{p,n+1}^{-T} = \left(\boldsymbol{I} - \Delta t \sum_{\alpha=1}^{N} \boldsymbol{P}_0^{\alpha} \dot{\gamma}_n^{\alpha} \right)^{T} \cdot \boldsymbol{F}_{p,n}^{-T} \tag{4.42}$$

4.4 Implementation in MSC Marc

FEM computations in this research are performed in combination with the FE solver *MSC Marc*. These computations follow the method that is described before with the elasticity, isotropic plasticity and crystal plasticity material models. Pseudocodes of the algorithms can be found in Appendix A.

4.4.1 Input file and Marc

The MSC Marc program works through submitting and running an input file. Inside this input file, the connectivity matrix is present, in which the nodal positions, element nodes and element type are defined. Even though MSC Marc has its own meshing options, the $Gmsh$ meshing software is used to create the mesh. This created mesh is pasted inside the input file. In the Marc Graphical User Interface (GUI), the boundary conditions can be added, which are automatically added to the input file.

4.4.2 USELEM subroutine

With the given boundary conditions, the user element (USELEM) subroutine is used. This subroutine is a *Fortran* (.f) file that is given to the MSC Marc program. It tells the software how the element stiffness matrix $[\boldsymbol{K}^{(i)}]_m$ and internal forces $[\hat{\boldsymbol{f}}_{int}^{(i)}]_m$ have to be calculated. This involves calculating all stresses and strains, in order to obtain the deformations and forces of the next time step. Therefore, isoparametric mapping, interpolation, linearisation and Gauss integration are used inside the USELEM subroutine to obtain $[\boldsymbol{K}^{(i)}]_m$ and $[\hat{\boldsymbol{f}}_{int}^{(i)}]_m$. Hardening is not implemented, but the relevant equations are given in the literature review.

4.4.3 Solution

When Marc has calculated the element stiffness matrices, as well as the internal forces for all elements, it assembles the elements into the global stiffness matrix $[\boldsymbol{K}^{(i)}]$ and solves the linear system of equations as represented in Equation 4.4. Then, Marc checks whether the residual satisfies the tolerance and, if it does not, proceeds to the next iteration until the solution has converged to the tolerance. If this is the case, it is moved on to the next time increment.

4.4.4 PLOTV subroutine

An important tool for postprocessing of the calculated results is the PLOTV subroutine. This subroutine allows the user to plot quantities that are not present in Marc's list of variables beforehand, such as quantities that are computed within the USELEM subroutine.

4.5 Cohesive zone model

Marc has a list of so-called interface elements, which can be used to model an interface between two materials. The 3D interface element that is considered in this research, is element 188 of Marc's element library, which is shown in Figure 4.1.

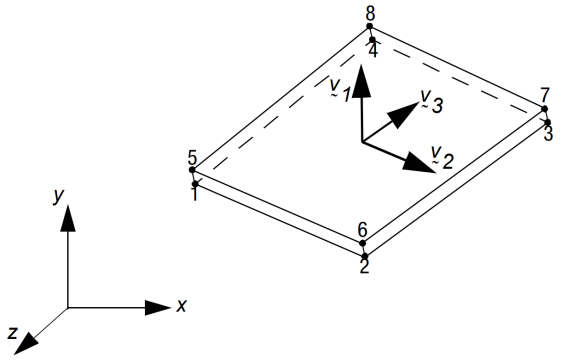

Figure 4.1: Schematic representation of cohesive zone element 188 [35].

The constitutive behaviour of this element is defined by the relation between the tractions versus relative displacements between the top and bottom surfaces of the element [35]. For the 3D interface element, the components of the relative displacements comprise one normal displacement and two shear displacements, according to:

$$\begin{aligned} v_1 &= u_1^{top} - u_1^{bottom} \\ v_2 &= u_2^{top} - u_3^{bottom} \\ v_3 &= u_3^{top} - u_3^{bottom} \end{aligned} \tag{4.43}$$

Using these relative displacements, the effective opening displacement is defined in Marc like:

$$v = \sqrt{v_1^2 + v_2^2 + v_3^2} \tag{4.44}$$

Marc offers three types of cohesive zone models: a bilinear, exponential and linear-exponential model. These three models are plotted in Figure 4.2, where here the universal binding energy relation is used, so the exponential model.

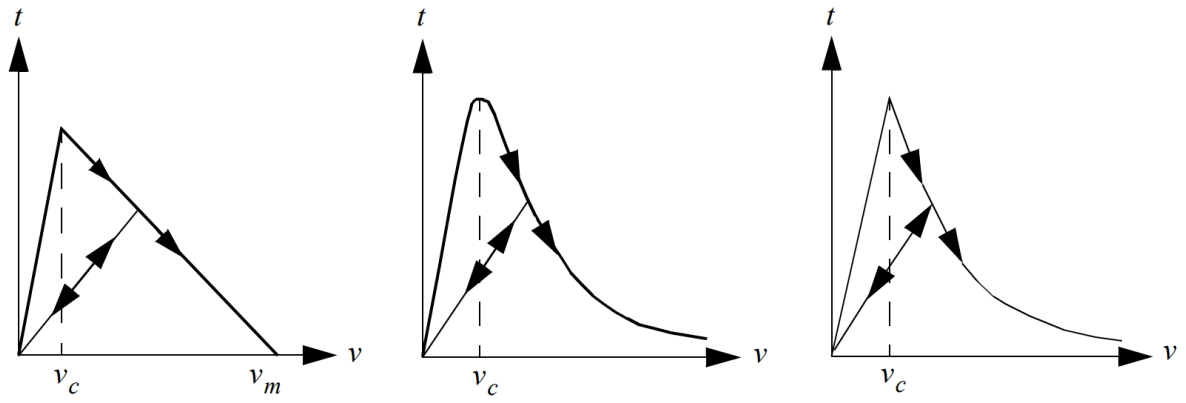

Figure 4.2: Bilinear (left), exponential (middle) and linear-exponential (right) cohesive zone models [35].

Keeping in mind the PVW of Equation 4.2, an additional term should be considered, namely a term due to the work of the cohesive tractions over the surfaces of the interface (S_{0coh}) [31]. This term is added to the PVW as follows:

$$\int_{S_0} \boldsymbol{v} \cdot \boldsymbol{t} \, \mathrm{d}S_0 + \int_{V_0} \boldsymbol{v} \cdot \boldsymbol{b}_0 \, \mathrm{d}V_0 + \int_{S_{0coh}} \boldsymbol{v} \cdot \boldsymbol{t} \, \mathrm{d}S_{0coh} = \int_{V_0} \nabla_x \boldsymbol{v} : \boldsymbol{P} \, \mathrm{d}V_0 \tag{4.45}$$

As input, Marc requires the cohesive energy and critical opening displacement for normal separation. The corresponding traction-separation behaviour can be adjusted in the shear directions by using shear/normal coefficients for the maximum stress (β_1) and cohesive energy (β_2). β_1 adjusts the effective opening displacement in the following way:

$$v = \sqrt{v_1^2 + \beta_1^2 v_2^2 + \beta_1^2 v_3^2} \tag{4.46}$$

and β_2 adjusts the cohesive energy in the shear direction. Furthermore, a stiffening factor in compression can be applied to increase the stiffness in compression. Upon full debonding between two elements, the interface element can be deactivated and removed from the post file. Full debonding occurs once the *damage* parameter inside a cohesive zone element has reached a value of 1, starting at 0 with no damage.

4.6 Numerical study

4.6.1 Geometry and mesh

Inclusions are usually distributed randomly inside the material as shown in the left schematic in Figure 4.3. In order to perform a computationally feasible analysis, the piece of material containing a random distribution of inclusions is divided into multiple equally sized periodic cells. Consequently, the inclusion volume fraction of the whole material is equal to that of the periodic cells. Each periodic cell contains a single inclusion. The geometry on which the FEM computations are performed, is a further simplified version of the periodic cell, called the representative unit cell, which contains one inclusion located at the centre of the cell.

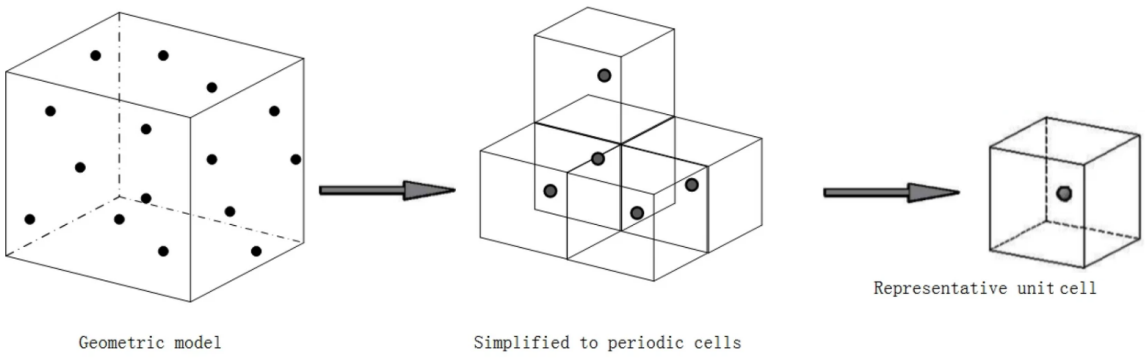

Figure 4.3: Schematic representation of periodic unit cell [36].

Carbide particles in spheroidised low-carbon steels are micron-sized (10^{-6}m) [33, 37] and therefore an inclusion diameter (d) of 1 micron is chosen. In order to get a low void volume fraction, corresponding to a low-carbon steel, it is chosen that the relation between the length of the side of the matrix (D) and the inclusion diameter (d): $d = \frac{D}{4}$. This means that $D = 4$ μm, leading to an inclusion volume fraction of 0.82 %.

From this geometry, a mesh is created using hexahedral 8-node elements. 512 of these elements are used to make the inclusion, 384 very thin elements of 3 nm thickness are used for the cohesive zone layer and 3840 elements are utilised for meshing the matrix. Various views of the resulting mesh can be observed in Figure 4.4. In Figure 4.4a, the complete mesh can be observed, which shows the outer elements of the whole mesh. By removing a quarter of the mesh, Figure 4.4b is obtained. Here the inclusion inside the matrix can be seen in terms of the mesh. Figure 4.4c shows half of the entire mesh, indicating a symmetric spherical inclusion inside the matrix. In between the inclusion and the matrix lies the cohesive zone layer, identified by a blue colour in Figure 4.4d. A total of 4975 nodes are shared among all elements making up the mesh.

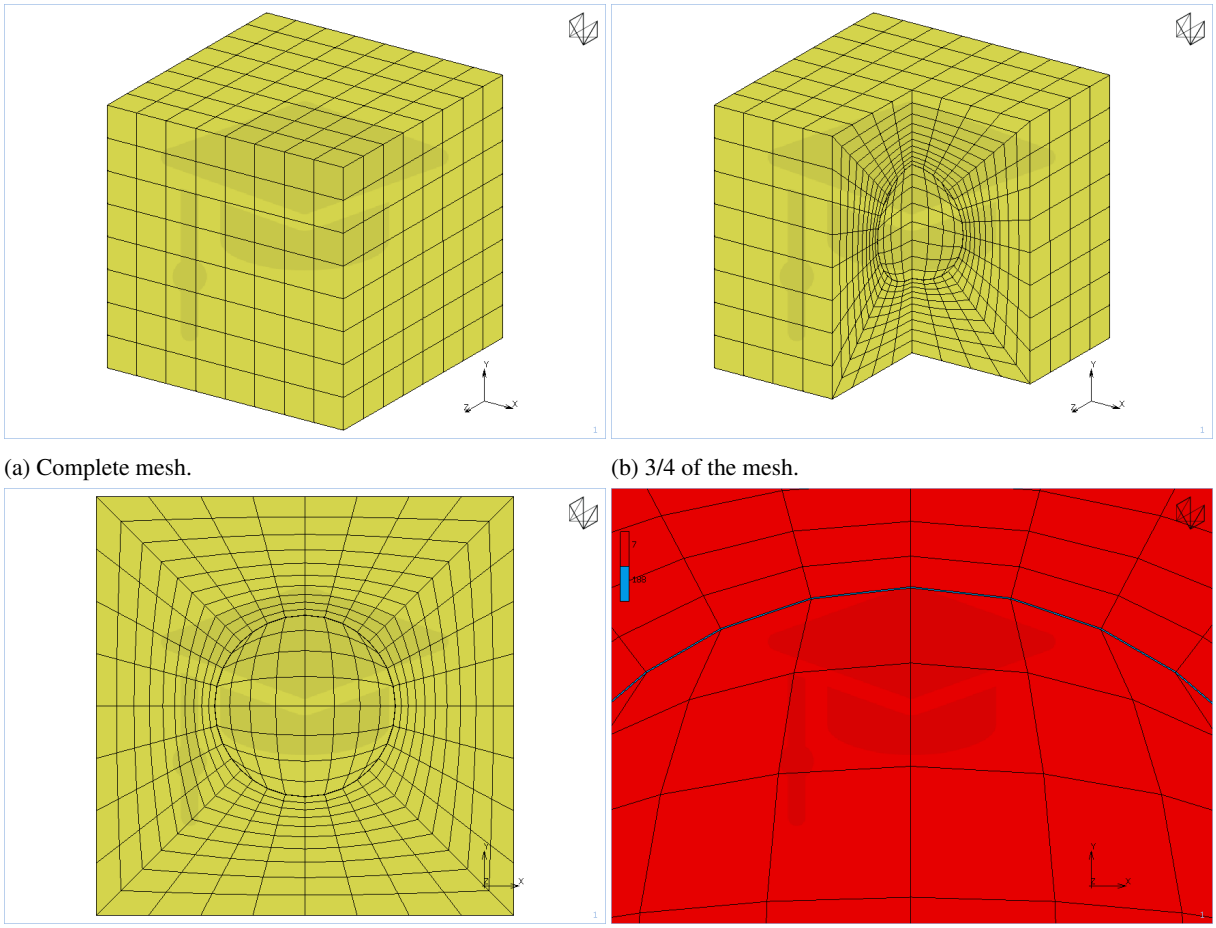

(a) Complete mesh.

(b) 3/4 of the mesh.

(c) 1/2 of the mesh.

(d) Cohesive zone layer (blue) between inclusion and matrix (both red).

Figure 4.4: Mesh with inclusion, matrix and cohesive zone layer in between.

4.6.2 Material parameters

Matrix

According to uniaxial micro-tensile tests performed on single crystals of ferrite [38], the material properties of the ferrite matrix are as shown in Table 4.1.

Quantity	Symbol	Value
Elastic constant	C_{11}	233.50 GPa
Elastic constant	C_{12}	135.50 GPa
Elastic constant	C_{44}	118.0 GPa
Yield stress	σ_y	110 MPa
Yield stress Taylor factor	σ_y	75 MPa
Reference plastic strain rate	$\dot{\lambda}_0$	0.01 s^{-1}
Strain rate sensitivity	m	0.05
Slip resistance {110}	$s^{\alpha}_{\{110\}}$	15 MPa
Slip resistance {112}	$s^{\alpha}_{\{112\}}$	15.25 MPa
Reference slip rate	$\dot{\gamma}_0$	0.01 s^{-1}
Strain rate sensitivity	m	0.05

Table 4.1: Ferrite matrix material properties [8, 38].

In the previous table, a yield stress can be found that is determined experimentally [38], but also a yield stress that is determined through a Taylor factor [39]. This Taylor factor relates the critical resolved shear stress to a yield stress. Only the slip resistances for the {110}<111> and {112}<111> slip systems are listed, even though {123}<111> slip systems are observed in some researches as well, giving 48 slip systems in total. The reason for this is that no {123}<111> slip system traces were observed in the micro-tensile tests that correspond to the material properties. The 24 slip systems that remain are listed in Table 4.2.

Number	Slip plane	Slip direction	Number	Slip plane	Slip direction
1	(011)	$[11\bar{1}]$	13	$(2\bar{1}1)$	$[11\bar{1}]$
2	(101)	$[11\bar{1}]$	14	$(\bar{1}21)$	$[11\bar{1}]$
3	$(1\bar{1}0)$	$[11\bar{1}]$	15	(112)	$[11\bar{1}]$
4	$(01\bar{1})$	$[1\bar{1}\bar{1}]$	16	(211)	$[1\bar{1}\bar{1}]$
5	(101)	$[1\bar{1}\bar{1}]$	17	$(12\bar{1})$	$[1\bar{1}\bar{1}]$
6	(110)	$[1\bar{1}\bar{1}]$	18	$(1\bar{1}2)$	$[1\bar{1}\bar{1}]$
7	(011)	$[1\bar{1}1]$	19	$(21\bar{1})$	$[1\bar{1}1]$
8	$(10\bar{1})$	$[1\bar{1}1]$	20	(121)	$[1\bar{1}1]$
9	(110)	$[1\bar{1}1]$	21	$(\bar{1}12)$	$[1\bar{1}1]$
10	$(01\bar{1})$	[111]	22	$(\bar{2}11)$	[111]
11	$(10\bar{1})$	[111]	23	$(1\bar{2}1)$	[111]
12	$(1\bar{1}0)$	[111]	24	$(11\bar{2})$	[111]

Table 4.2: BCC ferrite slip systems considered in this research [14].

Hardening of the matrix is not accounted for in all simulations, which means that the yield stress and slip resistances stay constant over the whole time period and keep their initial values:

$$\begin{aligned} \dot{\sigma}_y &= 0 \\ \dot{s}^{\alpha} &= 0 \end{aligned} \tag{4.47}$$

Inclusion

A wide range of DFT computations exists of anisotropic elastic constants of cementite, as summarised in the work of Bhadeshia [40]. In this research, however, isotropic values for this material are used because the cementite/ferrite interface behaves strongly anisotropic and the anisotropy of the cementite and the interface lie not within the scope of this research. The isotropic values are found by taking the average of the Reuss and Voigt

values of the anisotropic DFT elastic constant values and are given in Table 4.3. These values were calculated at zero Kelvin, but the difference with the elastic properties at room temperature is negligibly small.

Quantity	Symbol	Value
Young's modulus	E	203 GPa
Poisson's ratio	ν	0.35
Bulk modulus	K	227 GPa
Shear modulus	G	75 GPa

Table 4.3: Cementite inclusion material properties [40].

Cohesive zone

For the properties of the ferrite-cementite interface, the statement of Tvergaard and Hutchinson of Equation 2.63 is taken into account. Therefore, the cohesive strength is taken to be 110 MPa. A value of 0.5 J/m^2 is taken for the cohesive energy as this value is of the same order of magnitude as in previous studies [26, 33, 41], but at the lower side to ensure the occurrence of debonding. Also this value can be justified as the aim of this study is to draw qualitative conclusions and the ratio between the cohesive strength and cohesive energy is equivalent to the ratio observed in multiple studies [26, 33, 37, 42, 43]. The values are listed in Table 4.4 too.

Quantity	Symbol	Value
Cohesive strength	σ_c	110 MPa
Cohesive energy	G_c	0.5 J/m^2

Table 4.4: Cohesive zone properties.

4.6.3 Boundary conditions

Boundary conditions are selected such that the whole debonding process is captured within the total simulation time interval. For the sake of computational stability, a strain instead of a stress is applied. An applied displacement of 0.1 μm turned out to work properly, resulting in a total applied strain of 0.0125. This displacement is applied in the y-direction to the top of the matrix, as shown in Figure 4.5, while displacements of the nodes at the opposite sides are fixed to zero. The total displacement is applied in a total time of 1 second, where for the elasticity case 500 time steps are used, 5000 for the isotropic plasticity cases and 12500 for the crystal plasticity cases.

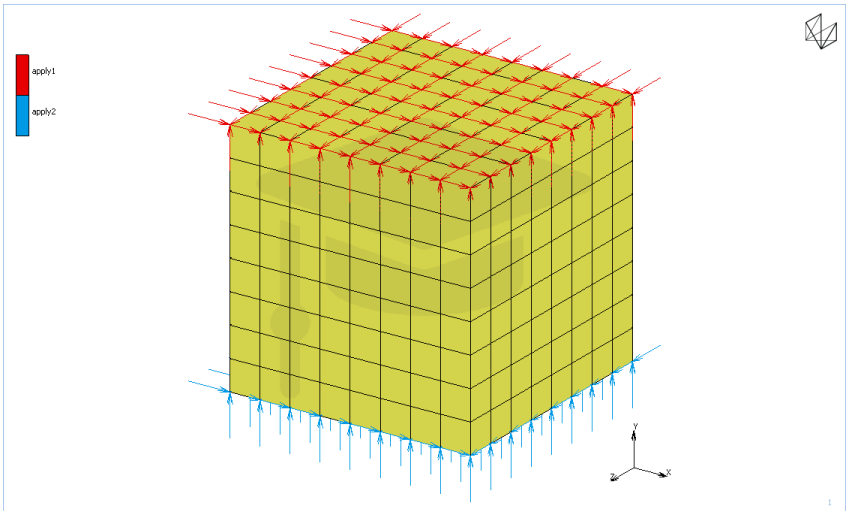

Figure 4.5: Displacement boundary conditions.

One unrotated and one rotated crystal are considered in this analysis. The rotated crystal orientation is a 45 degrees counterclockwise rotation, as depicted in Figure 4.6 indicated in red. This crystal rotation is chosen because it is a simple first rotation with respect to the axis along which the displacement is applied, namely the y-axis.

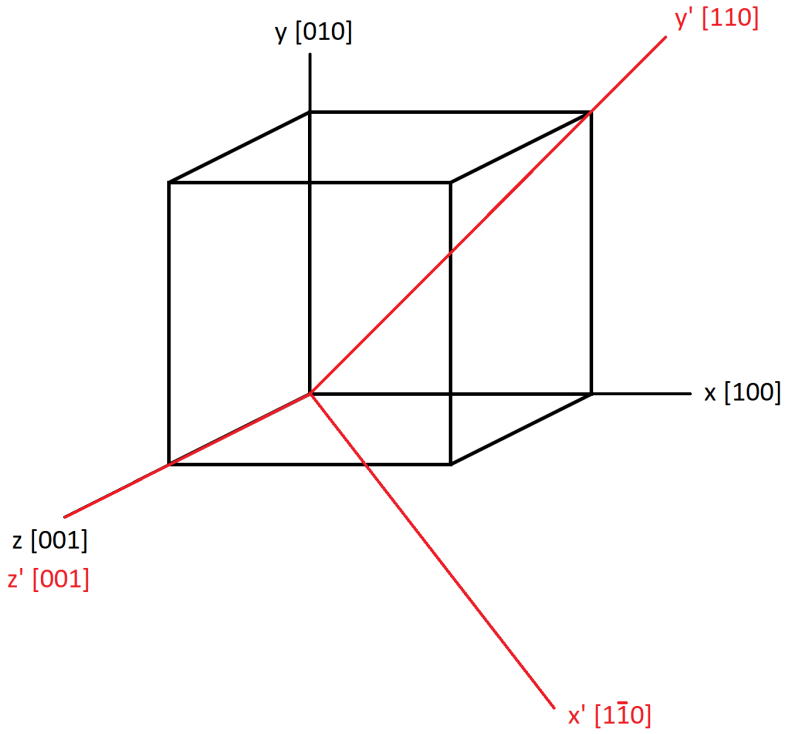

Figure 4.6: Crystal orientation of rotated crystal, indicated by the primes.

Number	Slip plane	Slip direction	Number	Slip plane	Slip direction
1	$(11\bar{\sqrt{2}})$	$[\sqrt{2}0\bar{1}]$	13	$(\frac{1}{2}\frac{\bar{3}}{2}\bar{\sqrt{\frac{1}{2}}})$	$[\sqrt{2}0\bar{1}]$
2	$(1\bar{1}\bar{\sqrt{2}})$	$[\sqrt{2}0\bar{1}]$	14	$(\frac{1}{2}\frac{3}{2}\bar{\sqrt{\frac{1}{2}}})$	$[\sqrt{2}0\bar{1}]$
3	$(0\bar{1}0)$	$[\sqrt{2}0\bar{1}]$	15	$(10\bar{\sqrt{2}})$	$[\sqrt{2}0\bar{1}]$
4	$(11\bar{\sqrt{2}})$	$[0\bar{\sqrt{2}}\bar{1}]$	16	$(\frac{3}{2}\frac{\bar{1}}{2}\bar{\sqrt{\frac{1}{2}}})$	$[0\bar{\sqrt{2}}\bar{1}]$
5	$(1\bar{1}\bar{\sqrt{2}})$	$[0\bar{\sqrt{2}}\bar{1}]$	17	$(\frac{3}{2}\frac{1}{2}\bar{\sqrt{\frac{1}{2}}})$	$[0\bar{\sqrt{2}}\bar{1}]$
6	(100)	$[0\bar{\sqrt{2}}\bar{1}]$	18	$(0\bar{1}\bar{\sqrt{2}})$	$[0\bar{\sqrt{2}}\bar{1}]$
7	$(11\bar{\sqrt{2}})$	$[0\bar{\sqrt{2}}1]$	19	$(\frac{3}{2}\frac{\bar{1}}{2}\bar{\sqrt{\frac{1}{2}}})$	$[0\bar{\sqrt{2}}1]$
8	$(1\bar{1}\bar{\sqrt{2}})$	$[0\bar{\sqrt{2}}1]$	20	$(\frac{3}{2}\frac{1}{2}\bar{\sqrt{\frac{1}{2}}})$	$[0\bar{\sqrt{2}}1]$
9	(100)	$[0\bar{\sqrt{2}}1]$	21	$(01\bar{\sqrt{2}})$	$[0\bar{\sqrt{2}}1]$
10	$(11\bar{\sqrt{2}})$	$[\sqrt{2}01]$	22	$(\frac{\bar{1}}{2}\frac{3}{2}\bar{\sqrt{\frac{1}{2}}})$	$[\sqrt{2}01]$
11	$(1\bar{1}\bar{\sqrt{2}})$	$[\sqrt{2}01]$	23	$(\frac{\bar{1}}{2}\frac{\bar{3}}{2}\bar{\sqrt{\frac{1}{2}}})$	$[\sqrt{2}01]$
12	$(0\bar{1}0)$	$[\sqrt{2}01]$	24	$(10\bar{\sqrt{2}})$	$[\sqrt{2}01]$

Table 4.5: Rotated BCC ferrite slip systems.

Chapter 5

Simulation results

5.1 Verification

An important first step is to check whether the algorithm is functioning correctly. For this reason, some benchmark tests have been performed.

Firstly, a simulation is done on one element of 1×1 mm. The elastic properties of this element were a Young's modulus $E = 200$ GPa and Poisson's ratio $\nu = 0.25$. One side of the element was fixed, as represented by the blue arrows in Figure 5.1. The other side was displaced by an amount of 0.1 mm. Stress and strain values calculated by the FEM algorithm were compared with hand-calculated values from the Saint-Venant model and these corresponded perfectly.

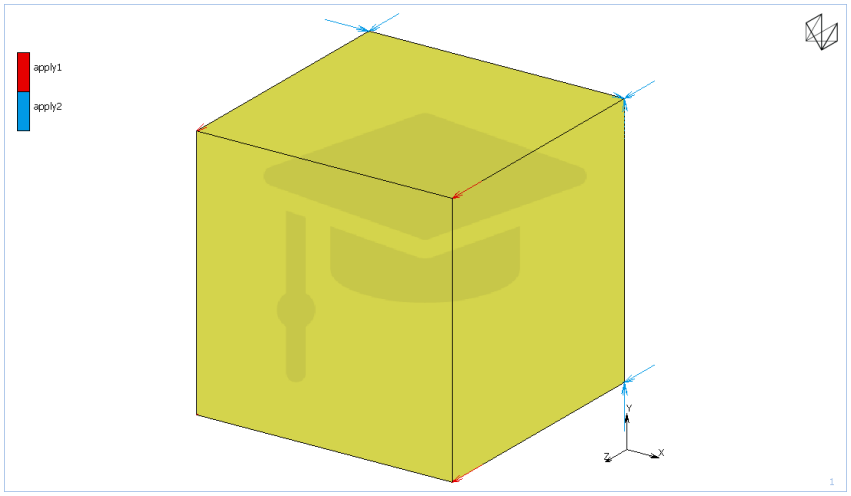

Figure 5.1: Boundary conditions of single elastic element simulation.

Secondly, the same boundary conditions were applied to a crystal plasticity element, but with plasticity disabled by putting the reference slip rate $\dot{\gamma} = 0$. This simulation yielded the same results for both elements, as can be seen in the plots of the P_{33} component of the first Piola-Kirchhoff stress tensor. This means that the elastic part of the crystal plasticity element is working as expected.

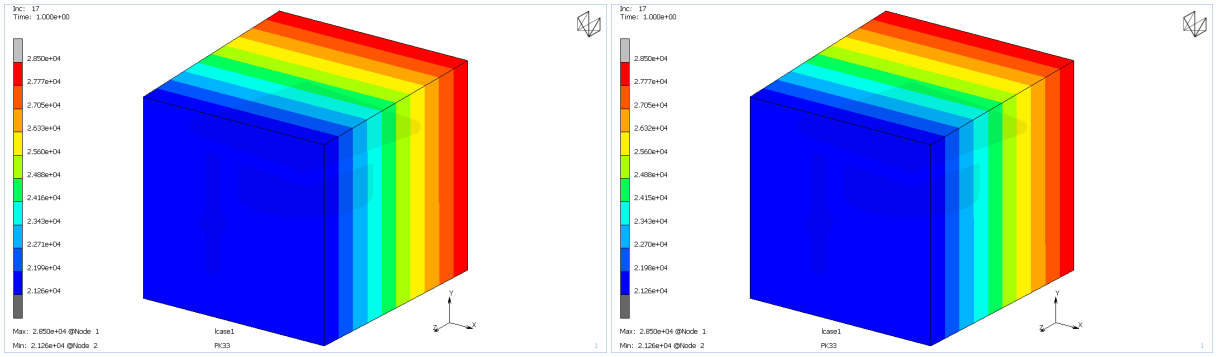

(a) P_{33} of single elastic element.

(b) P_{33} of single crystal plasticity element.

Figure 5.2: P_{33} after applied deformation for an elastic element and a crystal plasticity element.

Then, it is checked whether the real plasticity part of the crystal plasticity elements makes sense, by applying the same boundary conditions as before. However, for this case, the crystal plasticity parameters of Table 4.1 and Table 4.2 are utilised. At the end of the simulation, all slip systems were activated, except for slip systems 3, 6, 9 and 12. This is correct, since these four slip systems correspond to Schmid factors of zero according to Equation 2.40.

Eventually, the cohesive zone elements are tested by doing a simulation on two elastic elements with a cohesive zone element in between, as shown in Figure 5.3. A displacement of 0.1 mm was used again on the top element.

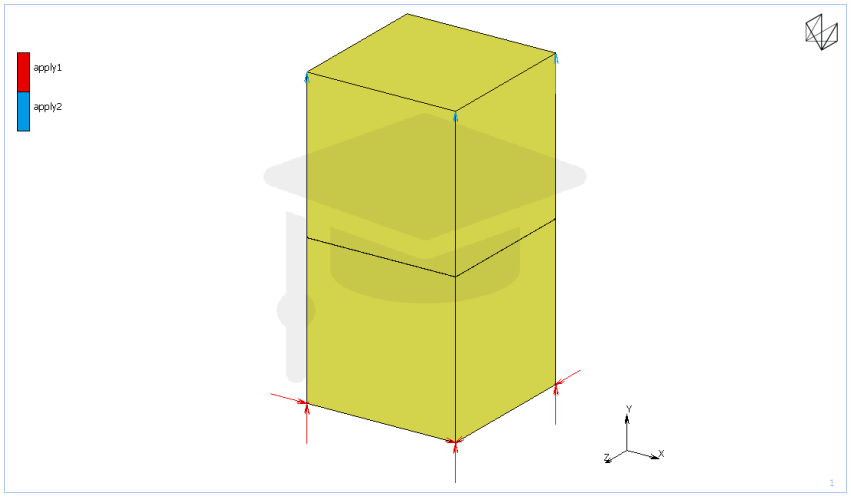

Figure 5.3: Three-element mesh to verify MSC Marc's cohesive zone element behaviour.

One simulation was done with the material model implemented by the author of this thesis, while one simulation was done with the material model from MSC Marc's library. Also a simulation was done on a single cohesive zone element without elastic elements at the sides. Cohesive zone properties were chosen as: σ_c = 74 MPa and G_c = 1 J/m^2. The traction-separation behaviour of one of the top four nodes was tracked, and is shown in Figure 5.4. Also the universal binding energy relation is plotted in this figure.

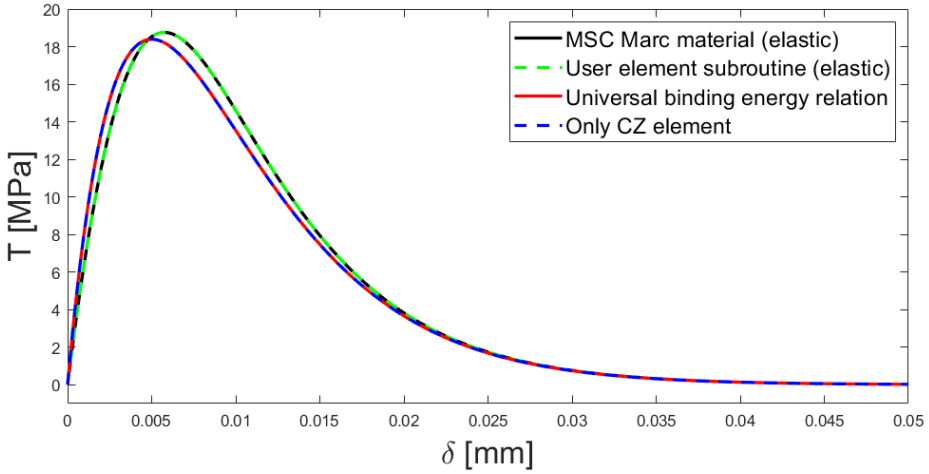

Figure 5.4: Traction versus separation of one of four nodes of top element.

It can be observed that the traction-separation behaviour of the user element subroutine and MSC Marc's own elastic implementation is very similar. However, they differ from the universal binding energy relation that is given as an input. This can be explained by elastic deformation of the two elements. This is not the case for the test on a single cohesive zone element, which shows the exact same curve as the universal binding energy relation.

5.2 Uniaxial tension

After verification of the algorithm, it is moved on to the real results for the uniaxial tension case. It should be noted that for the stress contour plots in this chapter, no nodal averaging is used, which means that the values at the nodes are not averaged using the values inside neighbouring elements. So, the values are presented as they are computed, which can result in rather discontinuous plots. This is done because the stresses calculated in the subroutine cannot communicate with the stress calculated by Marc inside the cohesive zone elements. This would result in nodal values being averaged with zero stress of the cohesive zone layer, leading to a blue ring around the inclusion. For all other plots, nodal averaging is used.

5.2.1 Global stress/strain behaviour

To begin with, investigating the global stress/strain response is an important step to locate certain events occurring during the debonding process. Therefore, the global stress/strain curve of σ_{yy} versus ε_{yy} can be observed in Figure 5.5 for all five material models. These material models are indicated by E = elasticity, P = isotropic plasticity, PTF = isotropic plasticity with Taylor factor, CPX = unrotated crystal plasticity and CPA = rotated crystal plasticity.

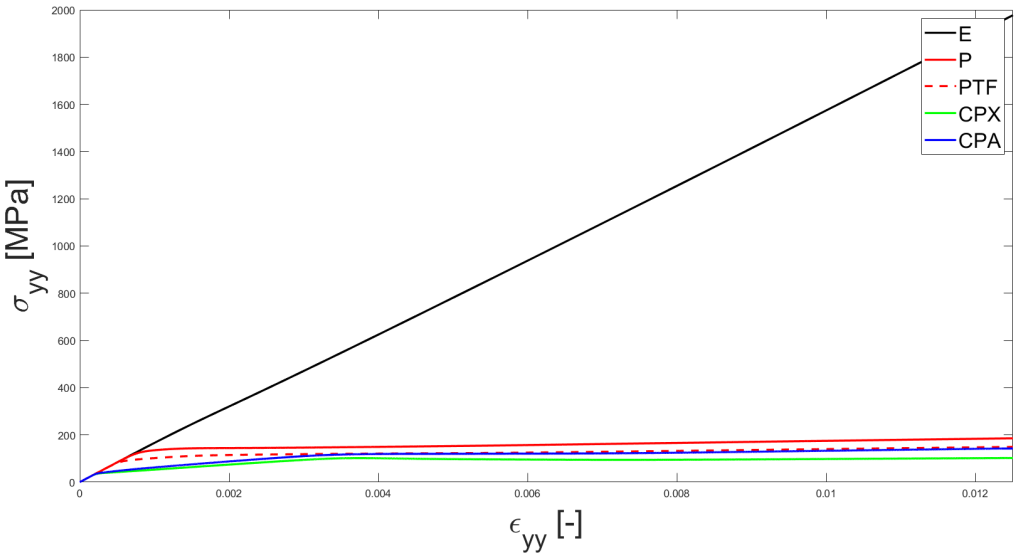

Figure 5.5: Global stress versus strain curve for all material models under uniaxial tension.

The black line, representing the pure elasticity model, reaches significantly larger stresses compared to the isotropic plasticity and crystal plasticity models. Because the line seems quite straight as well, the stress is cut off at 250 MPa in Figure 5.6 to investigate the behaviour of the plasticity and crystal plasticity models more easily.

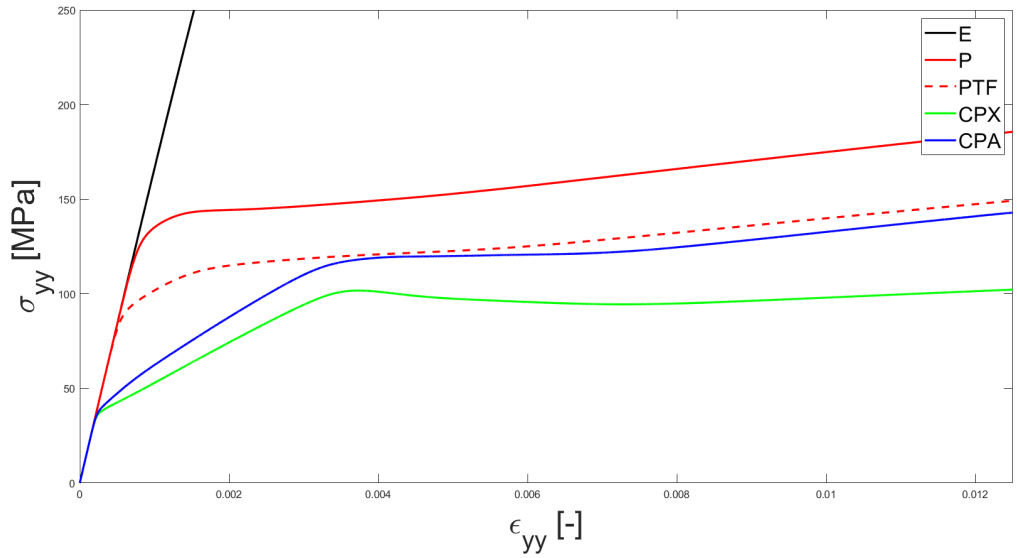

Figure 5.6: Global stress versus strain curve for all material models under uniaxial tension where the elastic curve is cut off at 250 MPa.

At small applied strain, all material models follow the seemingly straight line of the elasticity model. However, it becomes clear that for the isotropic plasticity models at least one major change in slope (stiffness) is present. For the crystal plasticity cases, two major changes in the slope are observed. The first drop in slope for both crystal plasticity cases happens simultaneously at smaller strain compared to both isotropic plasticity models. The slope of the PTF curve decreases at smaller strain than the P curve. After these first stiffness drops, the slope decreases another time for the CPX and CPA models at somewhat larger applied strain, where this drop starts earlier for the rotated crystal compared to the unrotated one.

To illustrate the stiffness variations more clearly, a plot of the stiffness versus applied strain can be found in

Figure 5.7, in which the derivatives at each point on the curves are computed.

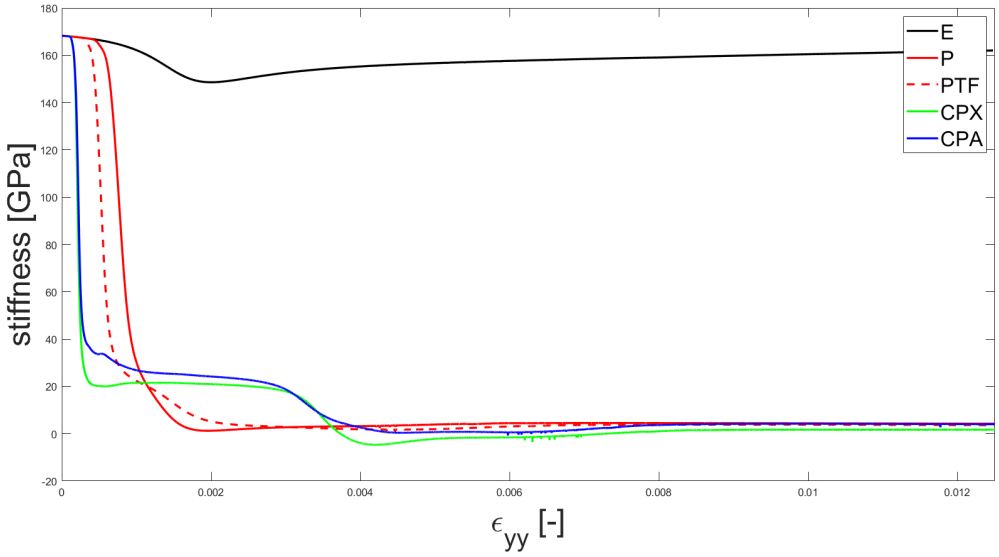

Figure 5.7: Stiffness as a function of the applied strain for all material models.

This figure shows a slight decrease in stiffness for the elastic material model too, which was not clear from Figure 5.5. Also, there seems to be a drop in stiffness for the PTF curve, right after its first drop. All other stiffness trends observed earlier can be found in this figure as well.

Other important observations related to the debonding of the inclusion from the matrix are listed in Table 5.1. The first column indicates the material model, whereas the second column states the applied strain at which the onset (first values) of the damage parameter is observed. In the third column, the applied strains are listed at which the first cohesive zone element is fully deleted and thus where full debonding has occurred. The fourth column contains the difference between the third and second column, and the last column shows the percentage of the total number of cohesive zone elements that are deleted entirely. There were 384 of these cohesive zone elements in total.

Material model	ε_{app} at 1st damage	ε_{app} at 1st deleted CZ element	Difference	Percentage of deleted CZ elements
E	$1.125 \cdot 10^{-3}$	$5.175 \cdot 10^{-3}$	$4.05 \cdot 10^{-3}$	63.5 %
P	$1.0375 \cdot 10^{-3}$	$4.2125 \cdot 10^{-3}$	$3.175 \cdot 10^{-3}$	79.2 %
PTF	$1.05 \cdot 10^{-3}$	$4.355 \cdot 10^{-3}$	$3.305 \cdot 10^{-3}$	74.0 %
CPX	$2.581 \cdot 10^{-3}$	$6.202 \cdot 10^{-3}$	$3.621 \cdot 10^{-3}$	69.8 %
CPA	$2.306 \cdot 10^{-3}$	$5.977 \cdot 10^{-3}$	$3.671 \cdot 10^{-3}$	69.8 %

Table 5.1: Observations from stress/strain curve with regard to debonding of the inclusion from the matrix.

The onset of damage, as well as the first deleted cohesive zone element happen at lowest applied strain for the isotropic plasticity case with the highest yield stress, while the last to experience this onset of damage is the rotated crystal plasticity model. The complete order from small to large strain is: P < PTF < E < CPA < CPX. But, the order for the difference between the onset of damage and the first deleted cohesive zone element has changed, as this difference is largest for the elasticity material model. The entire order from small to large strain is: P < PTF < CPX < CPA < E. So, this difference in strain is again the smallest for the isotropic plasticity model. Furthermore, the largest amount of cohesive zone elements is deleted for this material model too, whereas the smallest amount is deleted in the elasticity material model. The order is the same as for the difference, from largest to smallest percentage: P > PTF > CPX > CPA > E.

To investigate these effects and the effects observed in the stress strain curves, local stress and strain response are researched. This is done at different values for the applied strain, which are listed in Table 5.2 and visualised

in Figure 5.8 and Figure 5.9. These strain values are chosen as they lie at spots on the stress/strain curve where behaviour changes. The descriptions can be found in Table 5.2 too.

Applied strain step	Strain value	Description
ε_1	$7.5 \cdot 10^{-5}$	Everything is linear, before 1st drop CPX + CPA
ε_2	$2.5 \cdot 10^{-4}$	After 1st drop CPX + CPA, before 1st drop PTF
ε_3	$5.5 \cdot 10^{-4}$	After 1st drop PTF, before 1st drop P
ε_4	$1.125 \cdot 10^{-3}$	After 1st drop P, before 2nd drop PTF
ε_5	$2.9 \cdot 10^{-3}$	Before 2nd drop CPX + CPA
ε_6	$4.0 \cdot 10^{-3}$	After part of 2nd drop CPX + CPA
ε_7	$1.25 \cdot 10^{-2}$	End

Table 5.2: Values of the analysed applied strain steps with descriptions.

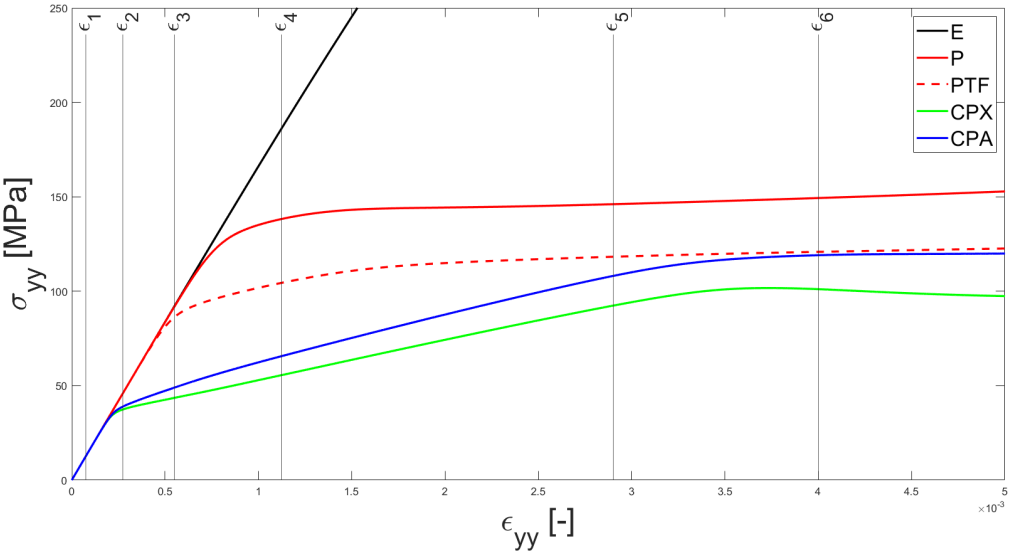

Figure 5.8: Global stress/strain curve until $\varepsilon_{yy} = 5 \cdot 10^{-3}$ where the strain steps are indicated with vertical black lines.

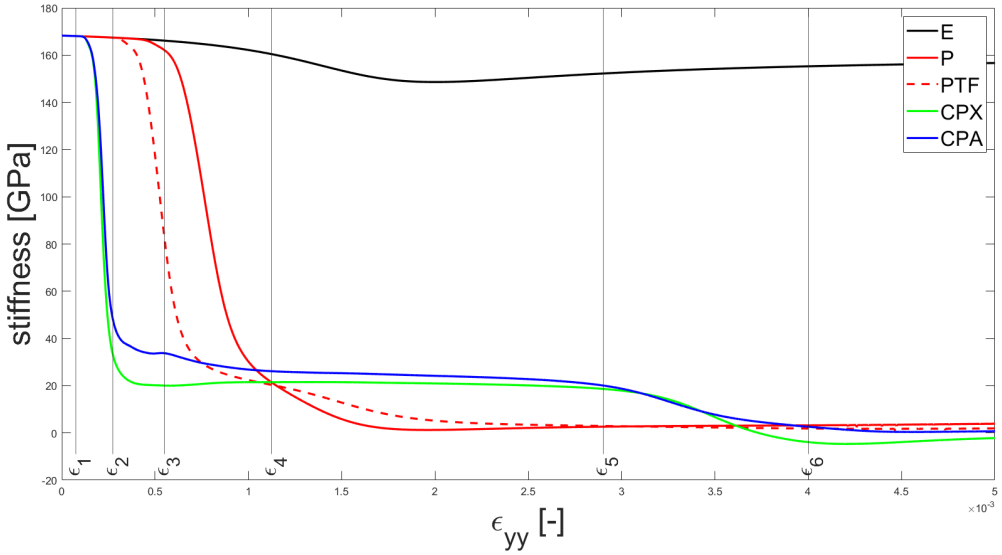

Figure 5.9: Stiffness versus applied strain curve until $\varepsilon_{yy} = 5 \cdot 10^{-3}$ where the strain steps are indicated with vertical black lines.

5.2.2 1st applied strain step

At the first applied strain step, which is before any drop in stiffness, the local stress and displacement fields are exactly the same for all material models. The stress and displacement for all models can be observed in Figure 5.10 in the x-y plane. In Figure 5.10a, the stress component σ_{yy} is plotted in MPa, which is mainly responsible for debonding. In Figure 5.10b the total resulting displacement is plotted. The stress is found to be highest near the interface of inclusion and matrix at the left and right sides. No plastic slip is observed and no damage is done to the cohesive zone layer.

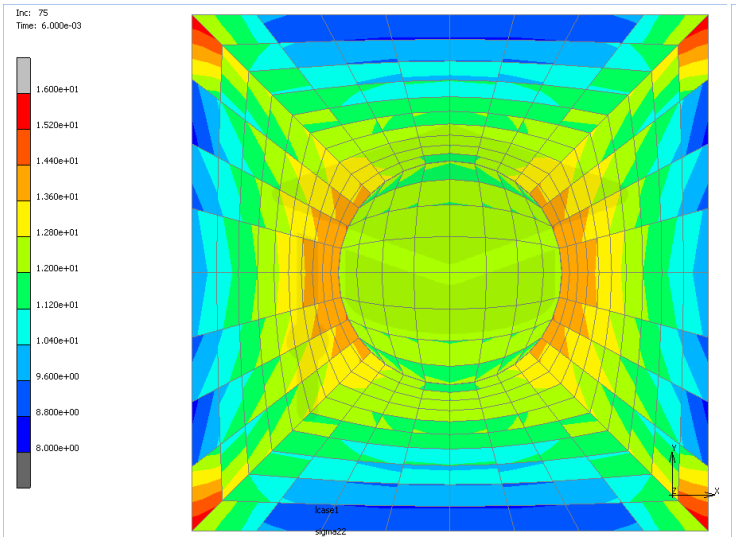

(a) σ_{yy} contours in MPa of all material models at the first applied strain step.

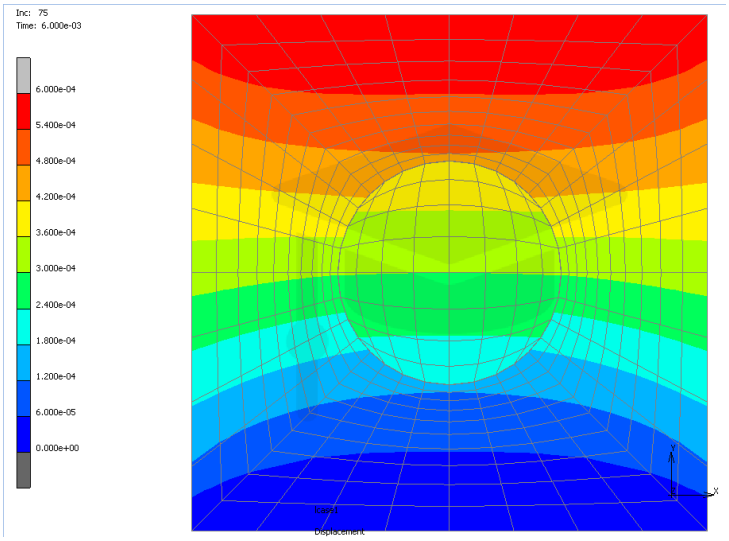

(b) Total displacement contours at the first applied strain step.

Figure 5.10: Contour plots of σ_{yy} and total displacement of all material models.

5.2.3 2nd applied strain step

At the second applied strain step, some deviations between the different material models can be observed. The stress has remained the same for the elasticity model and both isotropic plasticity models. Here, the highest stresses are still located at the left and right sides of the inclusion. However, the σ_{yy} values for both crystal plasticity models differ. In Figure 5.11, this stress is plotted for both crystal plasticity models. For the case of CPX, the stress is lower at the left and right sides, but has increased on the top and bottom sides of the inclusion. For the CPA case, the stress is still highest at the left and right sides, but it is lower with respect to the isotropic material models.

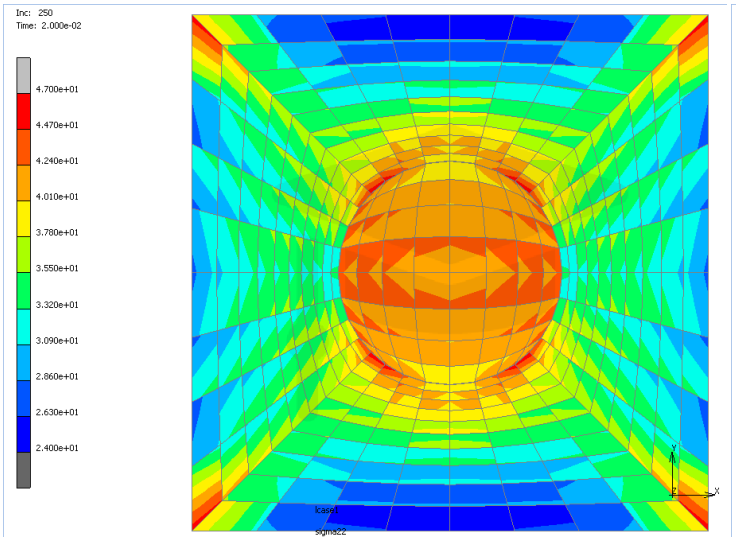

(a) σ_{yy} contours of the CPX model.

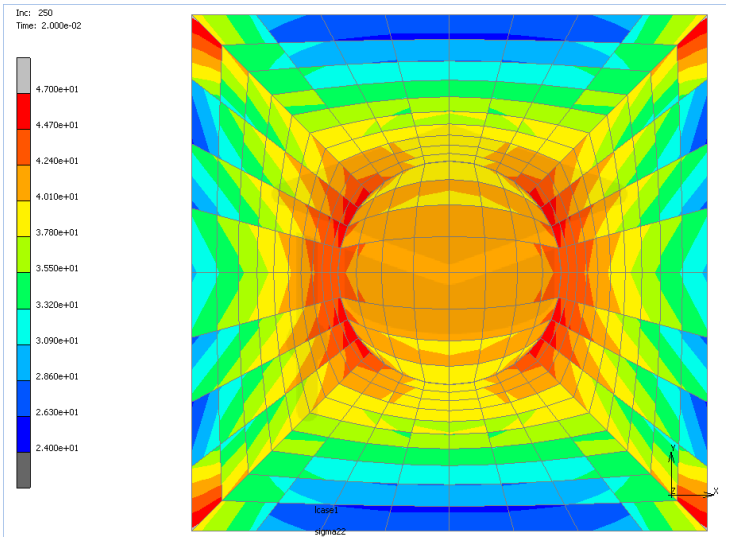

(b) σ_{yy} contours of the CPA model.

Figure 5.11: Contour plots of σ_{yy} of CPX and CPA for the second applied strain step.

Plastic slip occurs for the crystal plasticity models too, and the total plastic slip values on the x-y plane can be observed in Figure 5.12. For the CPX and CPA models, the plastic slip is concentrated at the left and right sides of the inclusion in a symmetric manner.

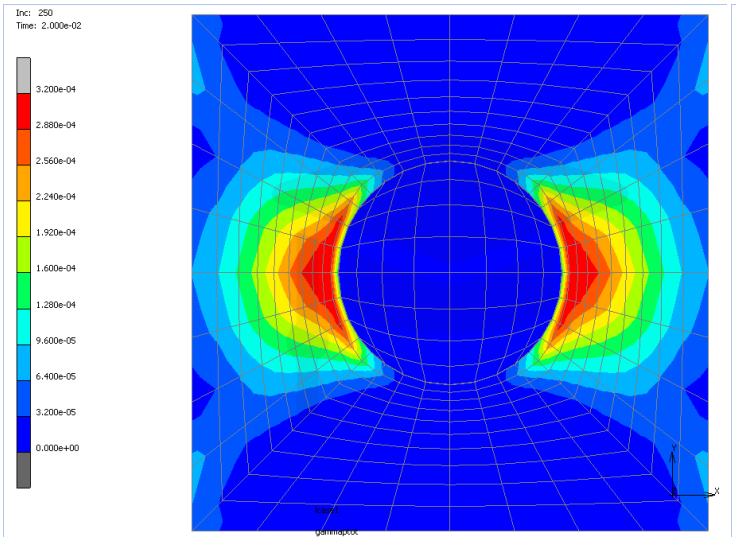

(a) Plastic slip for CPX.

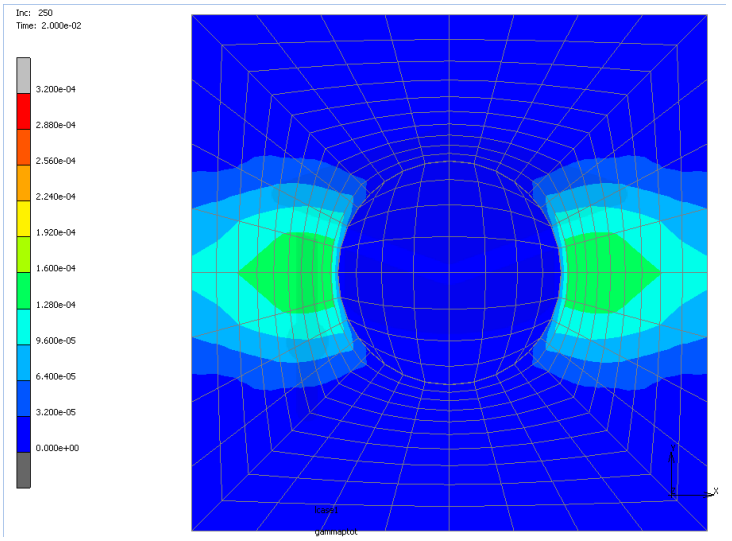

(b) Plastic slip for CPA.

Figure 5.12: Total plastic slip values for crystal plasticity models.

The plastic slip for the CPX model comprises mainly of slip through slip systems 14, 17, 20 and 23. In Figure 5.13d, the plastic slip of slip system 20 is displayed. It is maximum at the left and right sides, but the maximum values are located slightly more to the bottom left and top right. Slip on slip system 17 is located at the exact same location as for this slip system, with the exact same magnitudes. Plastic slip contours of slip systems 14 and 23 have similar shape and same magnitudes, but have their maximum values located at the top left and bottom right. Also, slip systems 3, 6, 9 and 12 are active to a lesser extent, as can be observed in Figure 5.13b for slip system 3. The other three slip systems have the same slip contours with the same magnitude.

Fewer slip systems are active for the CPA model, which are slip systems 18 and 21. Plastic slip on these slip systems is located directly at the left and right sides, as can be seen in Figure 5.14.

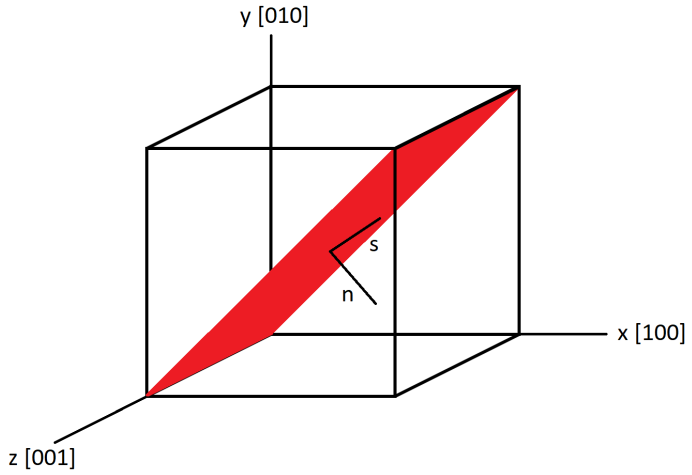

(a) Schematic of slip system 3 $(1\bar{1}0)[11\bar{1}]$ of CPX.

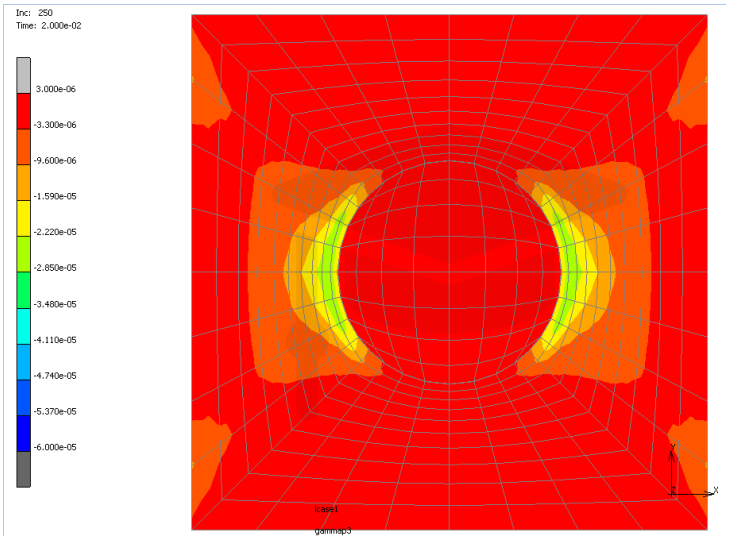

(b) Plastic slip of slip system 3 of CPX model at second applied strain step.

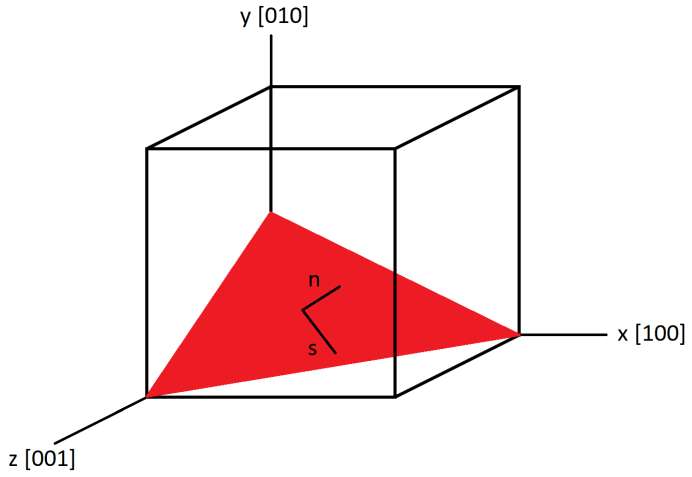

(c) Schematic of slip system 20 $(121)[1\bar{1}1]$ of CPX.

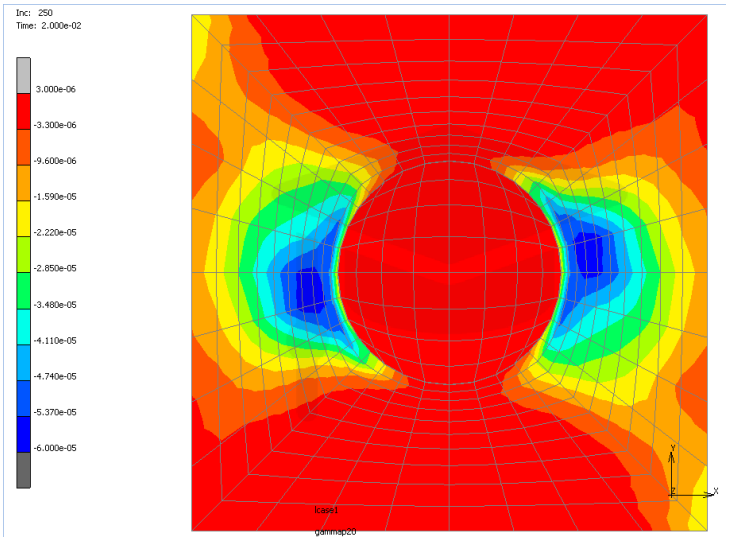

(d) Plastic slip of slip system 20 of CPX model at second applied strain step.

Figure 5.13: Plastic slip of slip systems 3 and 20 of CPX model at second applied strain step.

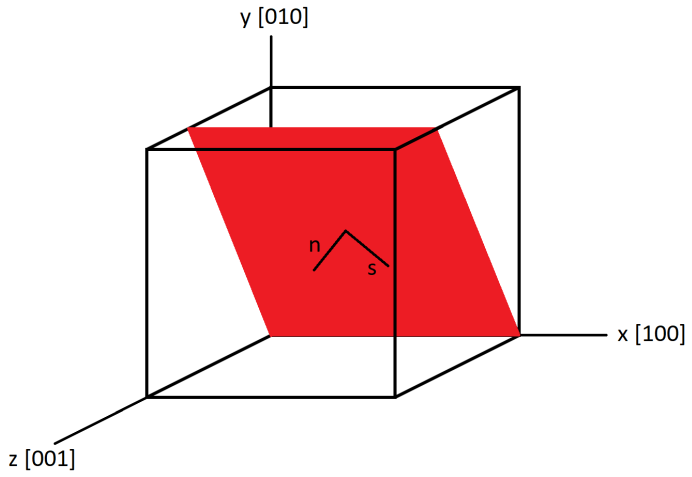

(a) Schematic of slip system 18 $(0\bar{1}\sqrt{2})[0\sqrt{\bar{2}}1]$ of CPA.

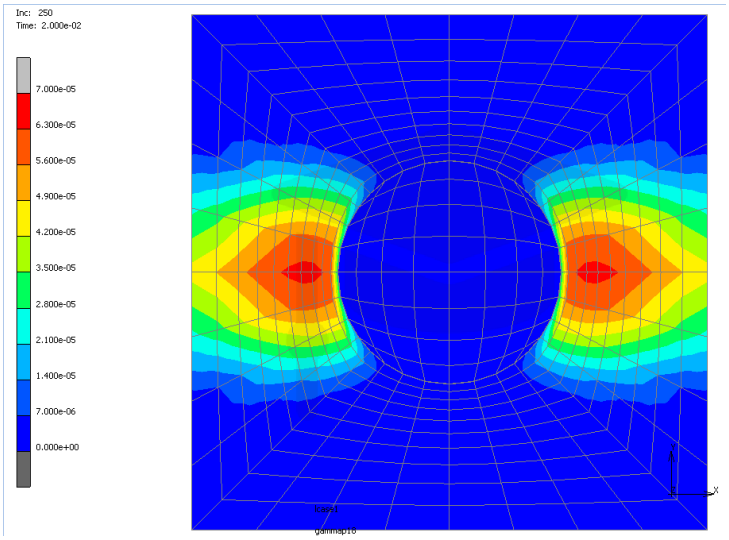

(b) Plastic slip of slip system 18 of CPA model at second applied strain step.

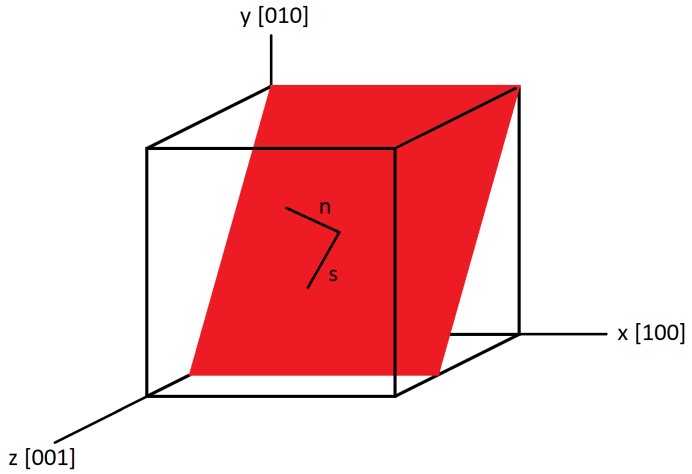

(c) Schematic of slip system 21 $(01\sqrt{2})[0\sqrt{\bar{2}}1]$ of CPA.

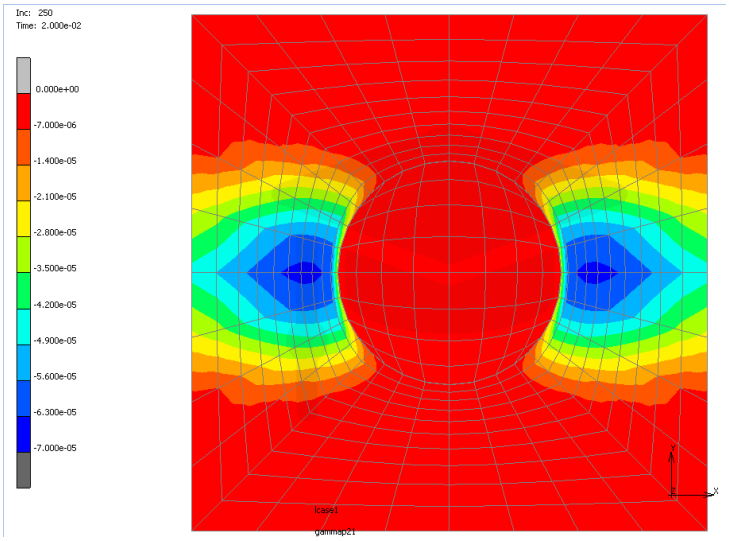

(d) Plastic slip of slip system 21 of CPA model at second applied strain step.

Figure 5.14: Plastic slip of slip systems 18 and 21 of CPA model at second applied strain step.

Displacements resulting from this applied strain step turn out to be the same for the elasticity and isotropic plasticity. The displacements in the y direction near the top of the inclusion are slightly higher and near the bottom of the inclusion are slightly lower for both crystal plasticity cases compared to the other models, as can be observed in Figure 5.15.

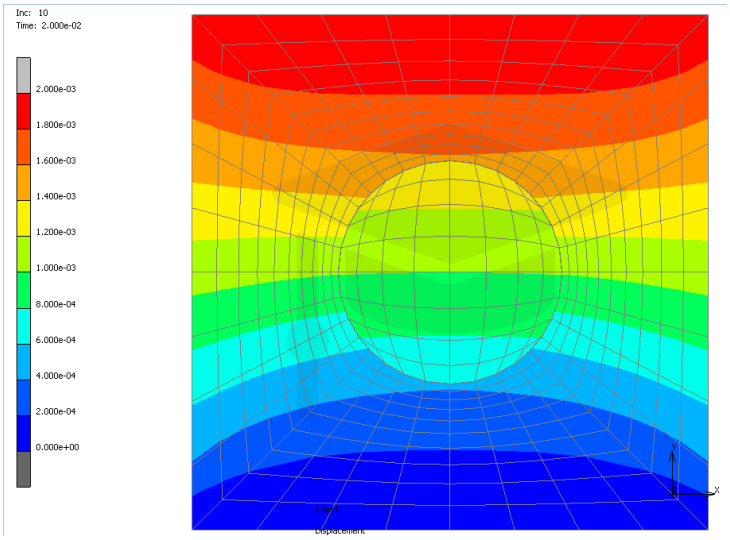

(a) Displacements of E at second applied strain step.

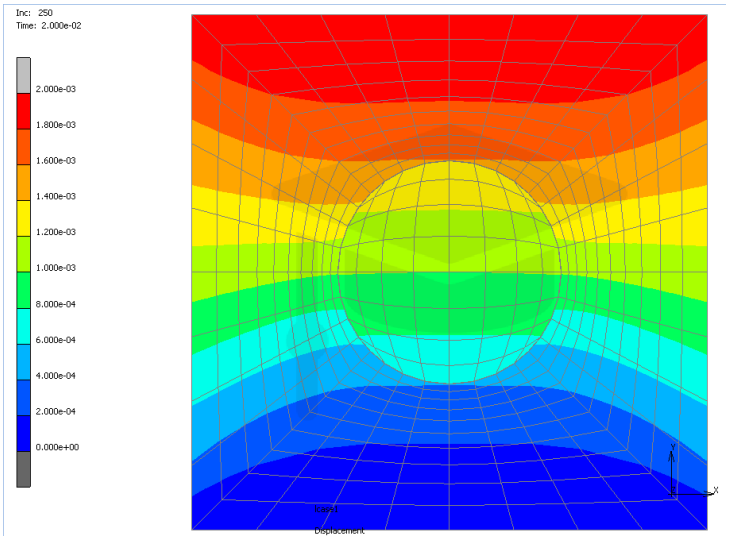

(b) Displacements of CPX at second applied strain step.

Figure 5.15: Displacements for E and CPX models.

5.2.4 3rd applied strain step

At the third applied strain step, the stress at the left and right side of the inclusion decreases for the PTF model as well, as can be observed in Figure 5.16. Practically, the stresses for E and P are still identical. The decrease in stress at the left and right sides continues for both crystal plasticity cases, while the increase on the top and bottom continues for both models too.

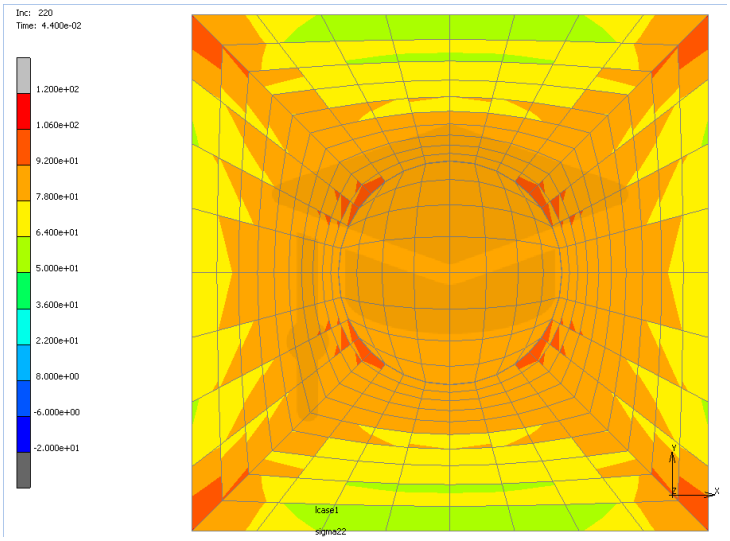

(a) σ_{yy} of PTF at third applied strain step.

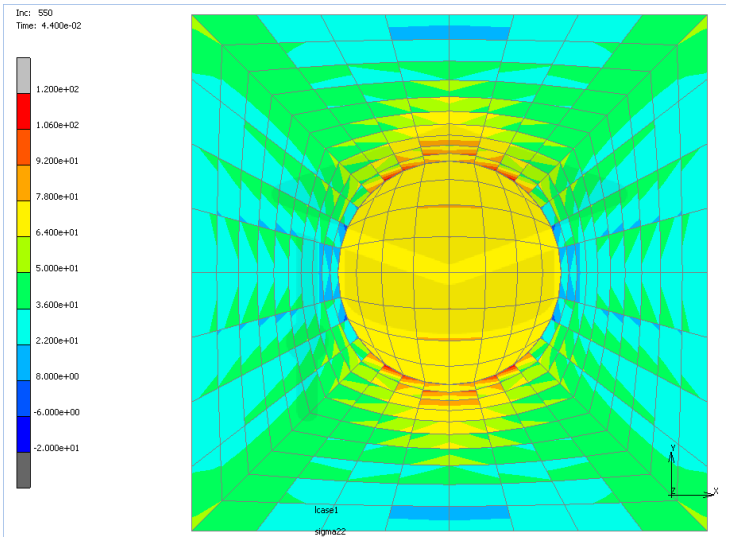

(b) σ_{yy} of CPX at third applied strain step.

Figure 5.16: σ_{yy} of PTF and CPX at third applied strain step.

Plots of the plastic strain and slip can be observed in Figure 5.17. Negligibly small plastic strain values were found for P, whereas the PTF starts yielding at the left and right side of the inclusion. Besides the plastic slip at the left and right side, also some plastic slip starts to occur at the top and bottom of the inclusion in both the CPX and CPA cases.

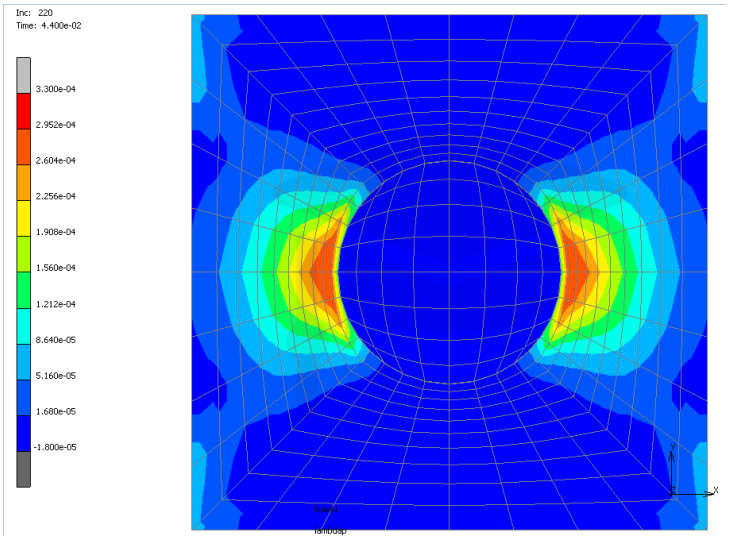

(a) Plastic strain of PTF model at third applied strain step.

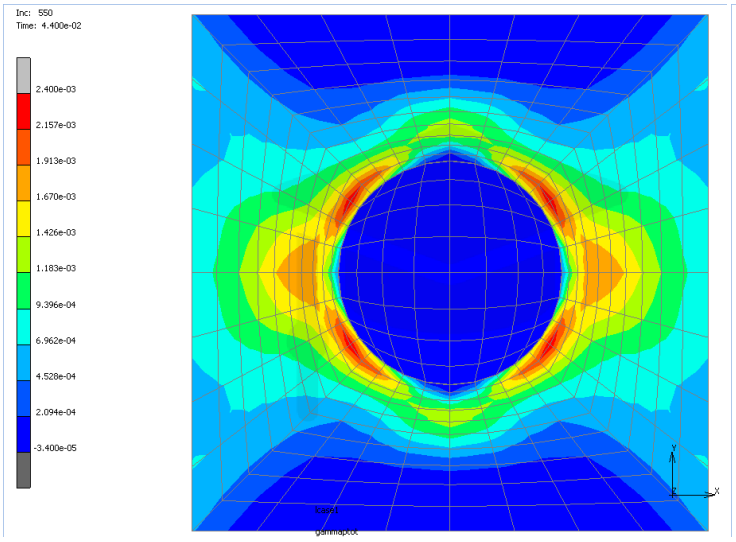

(b) Plastic slip of CPX model at third applied strain step.

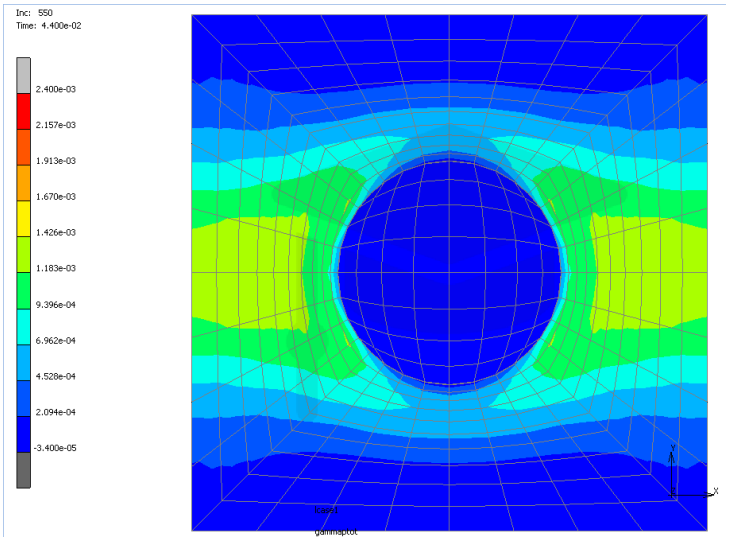

(c) Plastic slip of CPA model at third applied strain step.

Figure 5.17: Plastic strain of PTF, CPX and CPA models at third applied strain step.

Additional slip systems become active, which contribute to the total plastic slip of the CPX case. These newly activated slip systems are: 1, 4, 7 and 10. Figure 5.18b shows the plastic slip from slip system 4. The values are relatively small and are located at the top left and bottom right of the inclusion. Slip system 7 has the same values at the same locations. Slip systems 1 and 10 have the same values as well, but for these two cases the maximum values are located at the bottom left and top right of the inclusion with positive values. The slip values of the groups of slip systems 3 and 20 increase near the top and bottom of the inclusion, as shown in Figure 5.18.

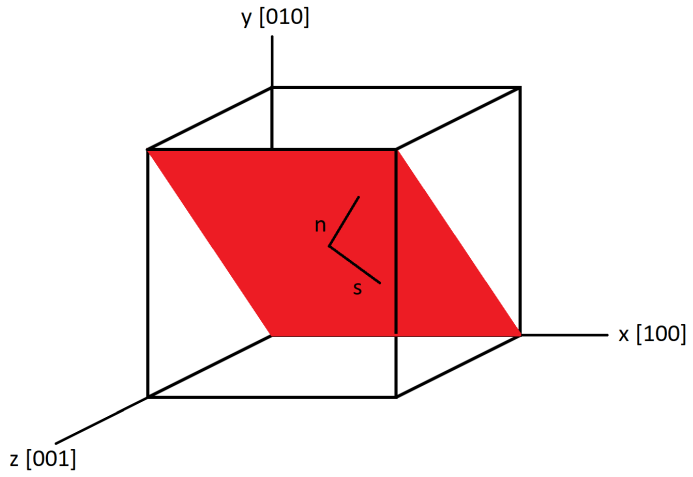

(a) Schematic of slip system 4 $(01\bar{1})[1\bar{1}\bar{1}]$ of CPX.

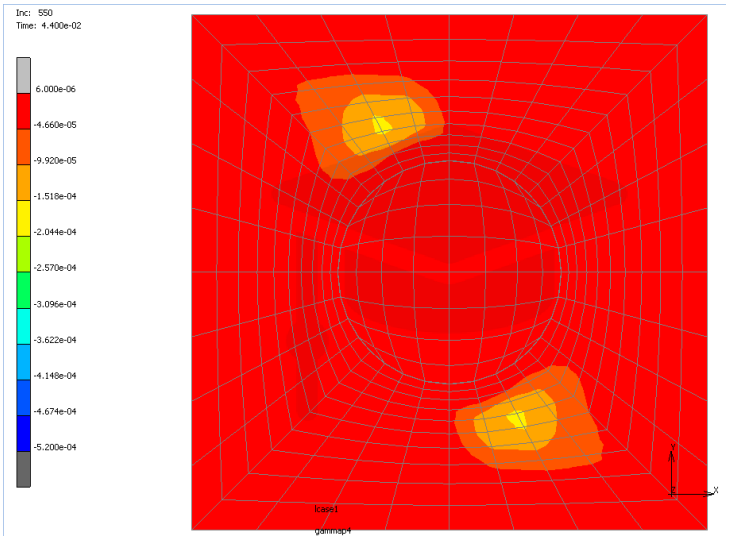

(b) Plastic slip of slip system 4 of CPX model at third applied strain step.

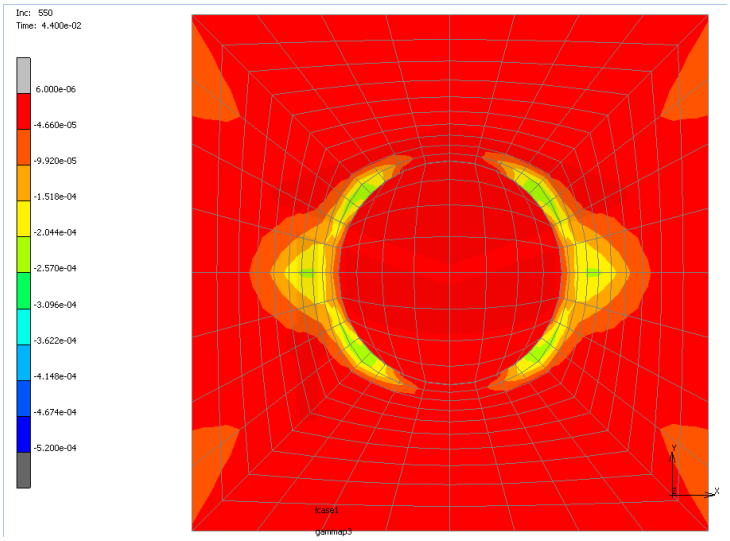

(c) Plastic slip of slip system 3 of CPX model at third applied strain step.

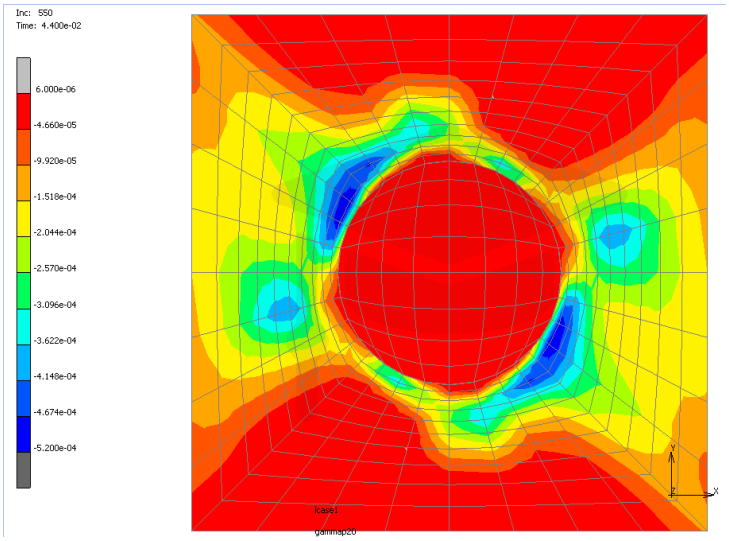

(d) Plastic slip of slip system 20 of CPX model at third applied strain step.

Figure 5.18: Plastic slip of slip systems 3, 4 and 20 of CPX model at third applied strain step.

Other slip systems activate inside the rotated crystal too, namely 4, 5, 7 and 8. Slip system 7 provides slip at the bottom left and top right of the inclusion, as shown in Figure 5.19b. Slip system 4 has the same values at the same spots, whereas the highest slip values for slip systems 5 and 10 are located at the top left and bottom right, which are positive values. Due to slip systems 18 and 21, slip increases at the left and right sides, but at the top and bottom of the inclusion as well.

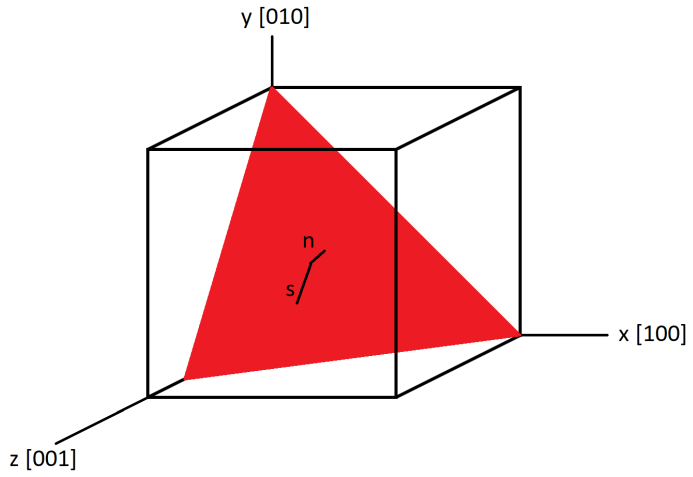

(a) Schematic of slip system 7 $(11\sqrt{2})[0\sqrt{2}1]$ of CPA.

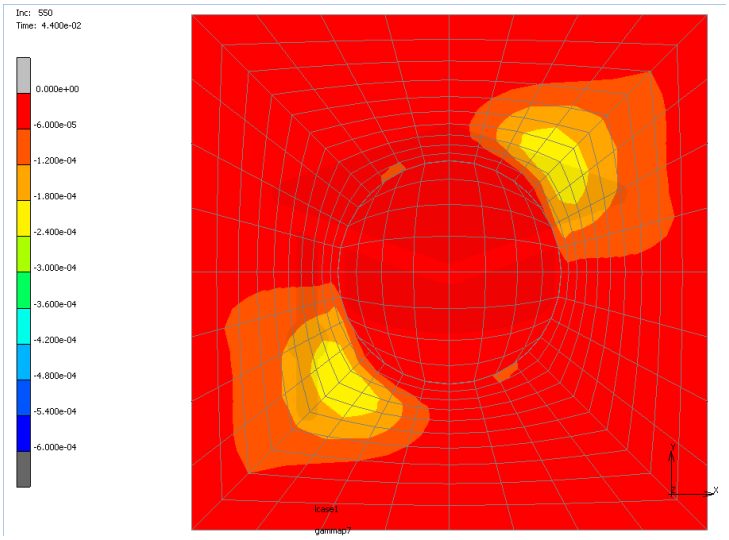

(b) Plastic slip of slip system 7 of CPA model at third applied strain step.

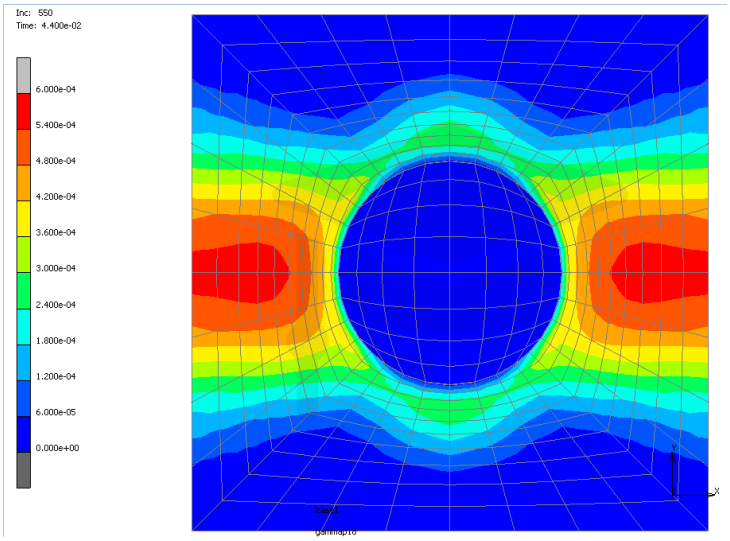

(c) Plastic slip of slip system 18 of CPA model at third applied strain step.

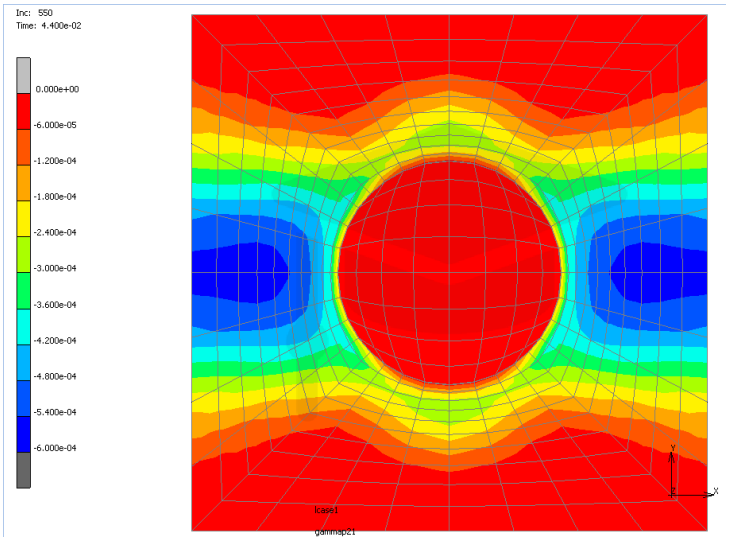

(d) Plastic slip of slip system 21 of CPA model at third applied strain step.

Figure 5.19: Plastic slip of slip systems 7, 18 and 21 of CPX model at third applied strain step.

The resulting displacement is now highest near the top and smallest near the bottom for PTF, as can be seen in Figure 5.20. At this location, also the E and P models have larger displacement differences at top and bottom compared to the crystal plasticity material models. The difference in displacement between the inclusion and matrix at the top and bottom is larger for the CPA model than the CPX model.

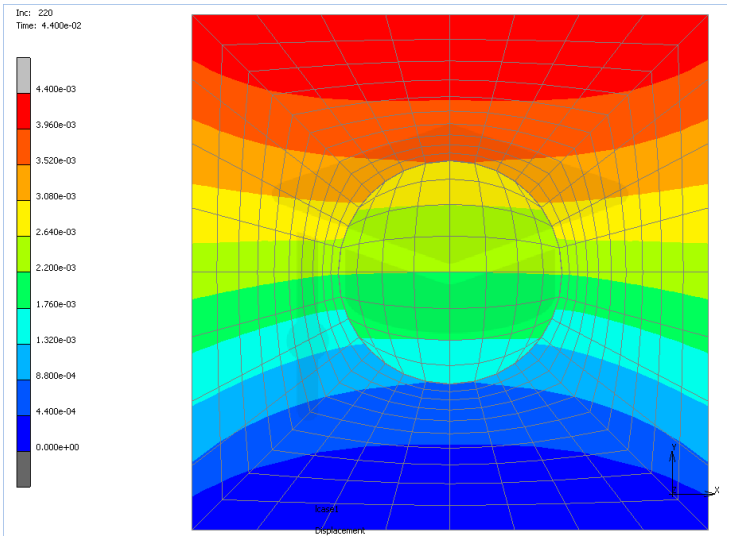

(a) Displacements of PTF at third applied strain step.

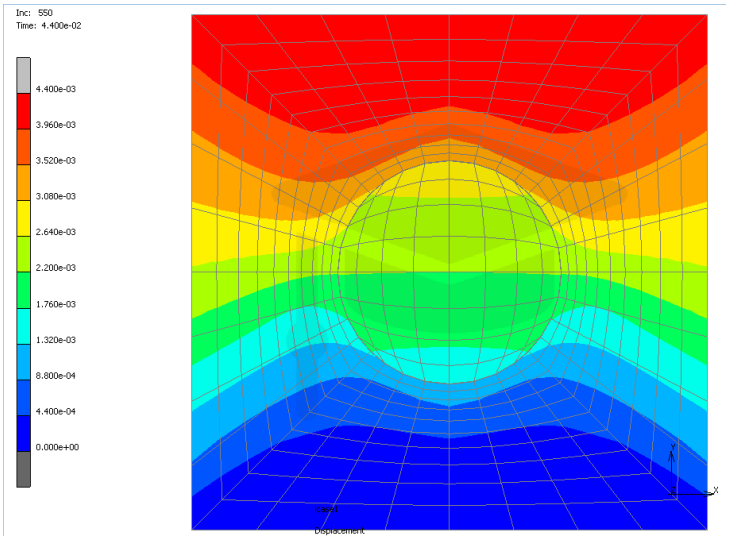

(b) Displacements of CPX at third applied strain step.

Figure 5.20: Displacements for PTF and CPX models at third applied strain step.

5.2.5 4th applied strain step

As can be seen from Figure 5.21, the stress in the P matrix decreases with respect to the E matrix at the fourth applied strain step, as was the case for the PTF matrix in the previous strain step. Now, there is also higher stress at the top compared to the left and right sides for both the P and PTF matrices. The stress trend for both crystal plasticity models continues.

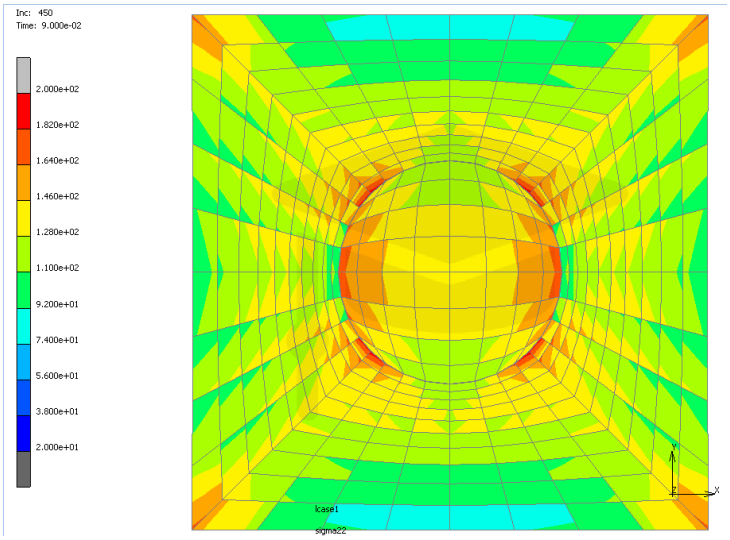

(a) σ_{yy} of P at fourth applied strain step.

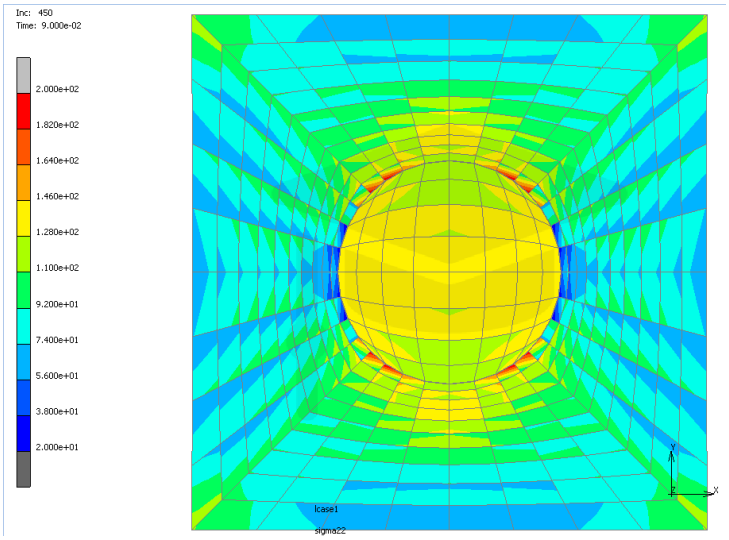

(b) σ_{yy} of PTF at fourth applied strain step.

Figure 5.21: σ_{yy} of P and PTF models at fourth applied strain step.

In addition, significant plastic strain is now occurring at the left and right sides of the inclusion in the P matrix. Small plastic strain is present near the top and bottom of the inclusion in the PTF matrix, as can be observed in Figure 5.22. The plastic slip also increases near the top and bottom of the inclusion in both crystal plasticity matrices. This can be seen in the same Figure 5.22. The plastic slip at the top and bottom is higher for the CPX model than for the CPA model.

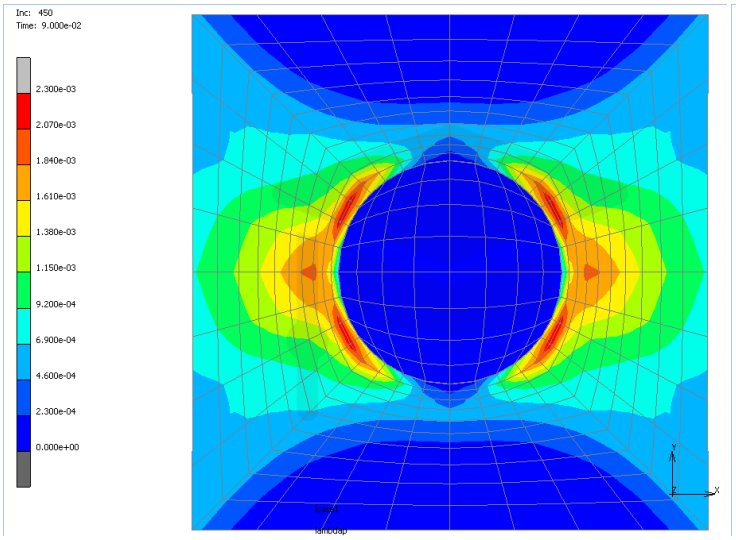

(a) Plastic strain of PTF model at fourth applied strain step.

(b) Plastic slip of CPX model at fourth applied strain step.

Figure 5.22: Plastic strain and plastic slip of PTF and CPX models at fourth applied strain step.

Plastic slip increases for all slip systems that were already active for CPX, especially at the top and bottom of the inclusion for the group of slip system 20. Slip systems 13, 16, 19 and 22 become slightly active, which have some slip on the top and bottom, but their highest slip values on the edges at which the total plastic slip is observed to be highest.

Similar observations are done for CPA for the groups of slip systems 7 and 21. Slip at the top and bottom of the inclusion increases for the group of slip system 21. Slip systems 1, 2, 10 and 11 become active, but with fairly low slip values that are located at the edges as for the group of slip system 13 for CPX. They have little plastic slip on the top and bottom of the inclusion. Slip systems 15 and 24 become somewhat more prominently present, with their largest values on the same edges at which the total plastic slip is highest for CPX.

Figure 5.23 shows the displacements at the fourth applied strain step for the P and PTF models. At the top of the inclusion, the difference in displacement between inclusion and matrix is now largest for the P matrix.

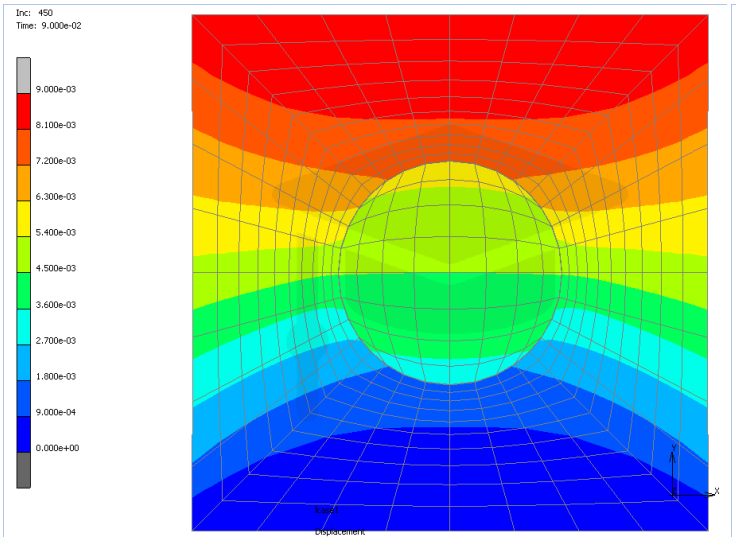

(a) Displacements of P at fourth applied strain step.

(b) Displacements of PTF at fourth applied strain step.

Figure 5.23: Displacements for P and PTF models at fourth applied strain step.

As a consequence of the applied strain, damage is done to the cohesive zone layer at the top and bottom of the inclusion, which is displayed in Figure 5.24. This is observed for all three purely isotropic material models.

The damage is larger and comprises more elements for the P model, while the damage values for the PTF model is of similar magnitude. The cohesive zone layer for the E model has little damage, whereas the layer remains undamaged for the crystal plasticity models.

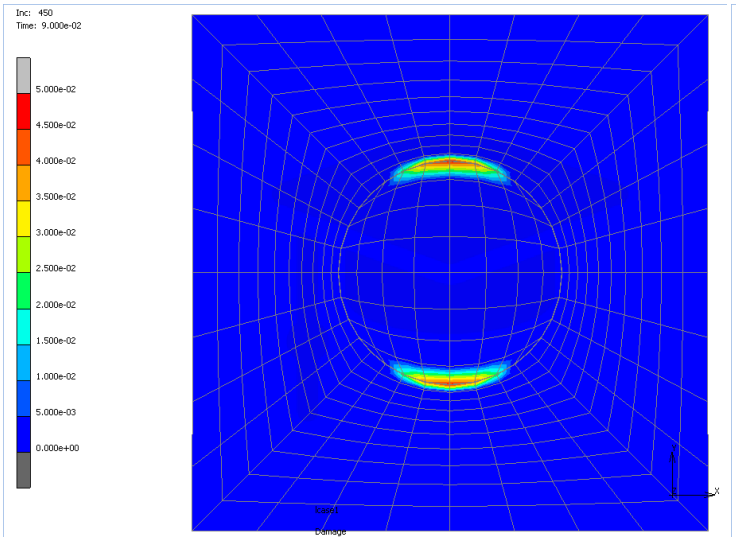

(a) Damage of P at fourth applied strain step.

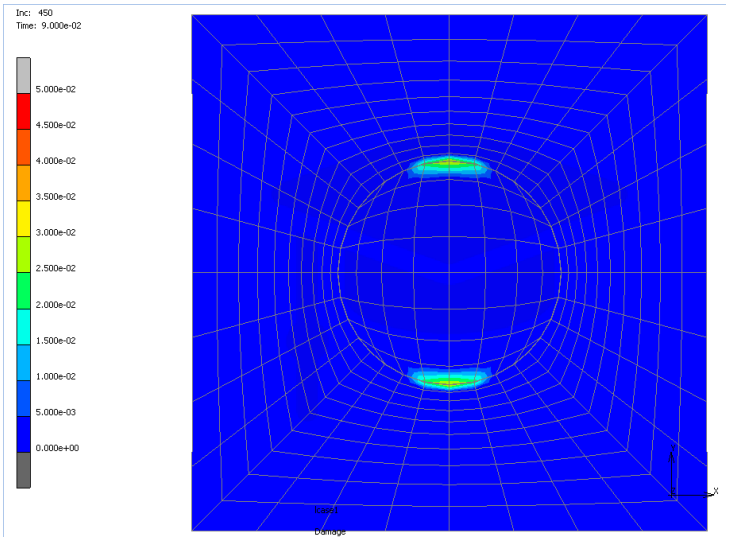

(b) Damage of PTF at fourth applied strain step.

Figure 5.24: Damage of P and PTF models at fourth applied strain step.

5.2.6 5th applied strain step

A decrease in stress is observed at the top and bottom of the inclusion for the E, P and PTF models, as can be concluded from Figure 5.25.

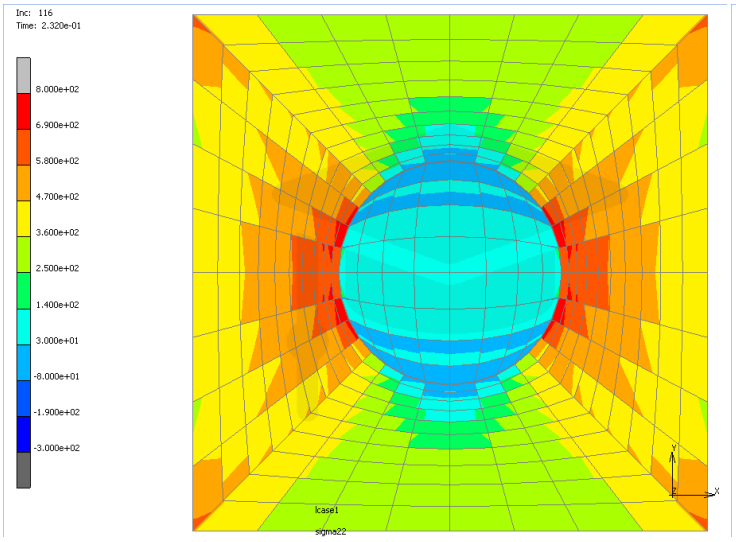

(a) σ_{yy} of E at fifth applied strain step.

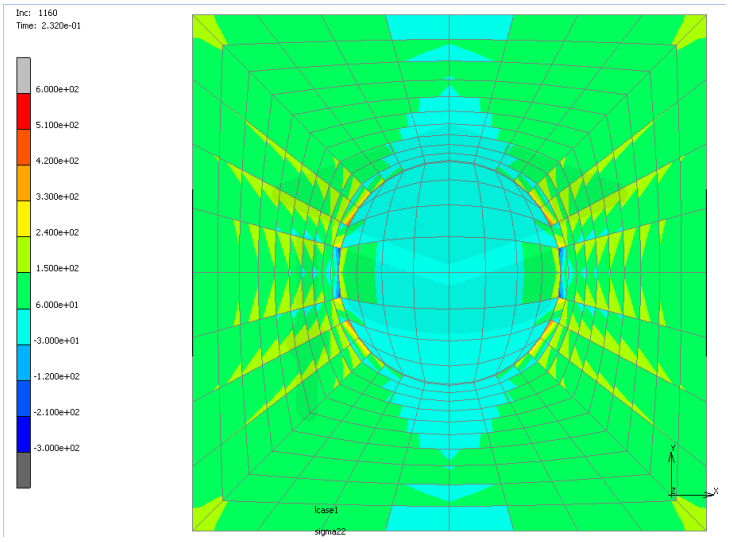

(b) σ_{yy} of P at fifth applied strain step.

Figure 5.25: σ_{yy} of E and P models at fifth applied strain step.

Plastic strain stays at the left and right sides of the inclusion for P and has increased compared to the previous strain. The PTF model still shows very little plastic strain at the top and bottom, next to its large strains at the left and right sides. The plastic slip keeps increasing on the top and bottom of the inclusion for the CPX and CPA models and the plastic slip values at the top and bottom have exceeded their values at the left and right sides, as can be observed in Figure 5.26.

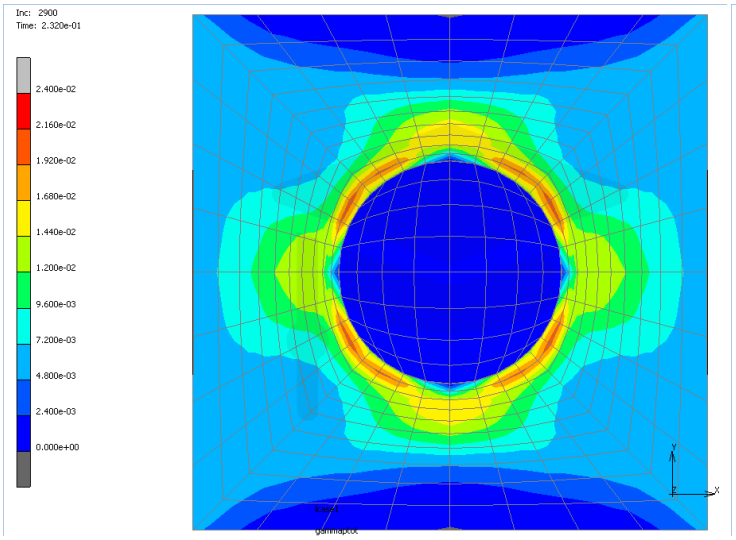

(a) Plastic slip of CPX model at fifth applied strain step.

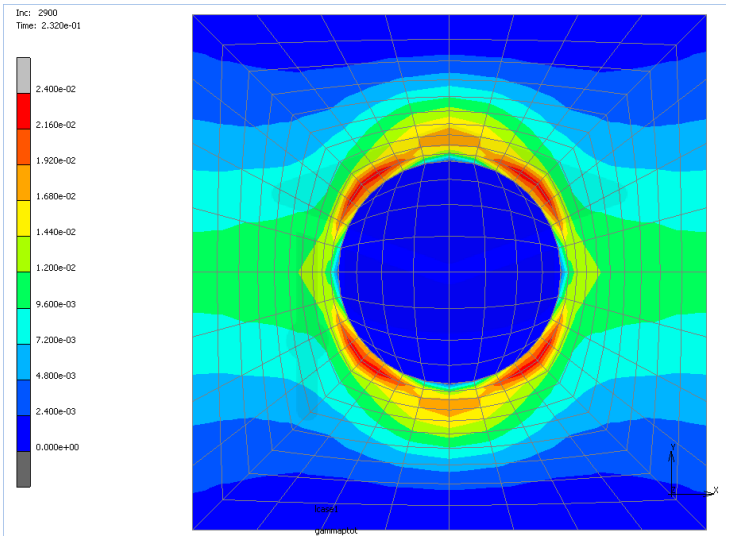

(b) Plastic slip of CPA model at fifth applied strain step.

Figure 5.26: Plastic slip of CPX and CPA models at fifth applied strain step.

Plastic slip of the group of slip system 20 continues increasing at the top and bottom of the CPX matrix. Slip systems 2, 5, 8 and 11 become active too, which have their highest slip values on the four red high-value edges in Figure 5.26.

Slip on slip system 21 of the CPA matrix has exceeded its values of the left and right sides on the top and bottom of the inclusion. As can be seen in Figure 5.27, slip has increased at the top and bottom of the inclusion for slip system 15. The same holds for slip system 24.

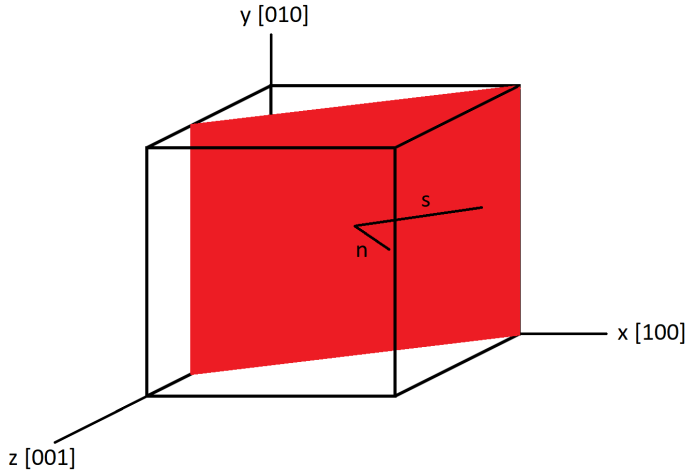

(a) Plastic slip of slip system 15 of CPA model at fifth applied strain step.

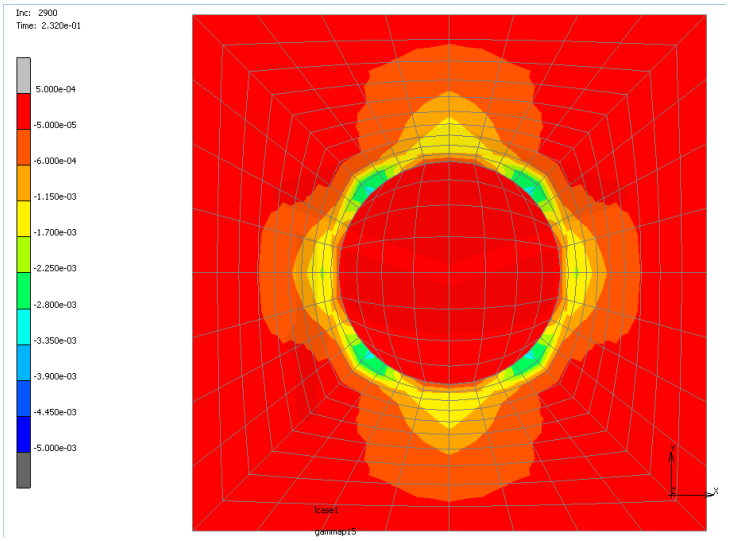

(b) Plastic slip of slip system 15 of CPA model at fifth applied strain step.

Figure 5.27: Plastic slip of slip system 15 of CPA model at fifth applied strain step.

For E, P and PTF the damage has spread further and has increased in value. Also, there is some damage done to the cohesive zone layer of the CPX geometry at the top and bottom. Even more damage can be found on the cohesive zone layer of the CPA model.

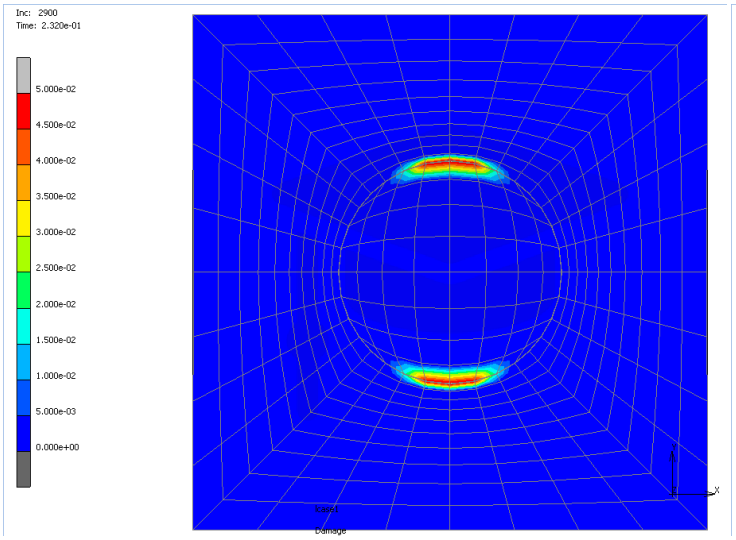

(a) Damage of CPX at fifth applied strain step.

(b) Damage of CPA at fifth applied strain step.

Figure 5.28: Damage of CPX and CPA models at fifth applied strain step.

5.2.7 6th applied strain step

Stress for the purely isotropic material models keeps going down at the top and bottom interface between inclusion and matrix. The stress at the location of highest stress seem to be the same for both crystal plasticity models. Similar plastic strain contours are obtained at the sixth applied strain step compared to the previous strain step for the crystal plasticity models. However, the plastic slip now again occurs mostly on the left and right sides, as shown in Figure 5.29.

This is substantiated by decreases in plastic slip for the group of slip system 20 for CPX and the group of slip system 21 for CPA, where the slip has decreased at this applied strain step at the top and bottom of the inclusion. The damage increases for all models.

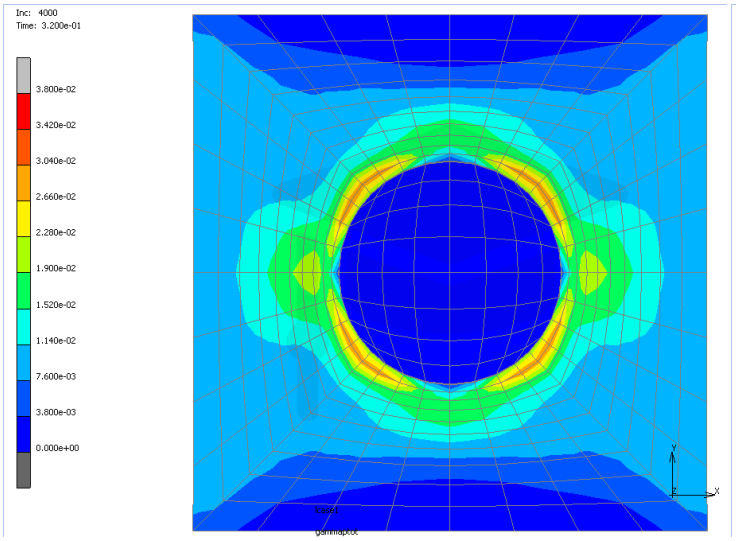

(a) Plastic slip of CPX model at sixth applied strain step.

(b) Plastic slip of CPA model at sixth applied strain step.

Figure 5.29: Plastic slip of CPX and CPA models at sixth applied strain step.

5.2.8 7th applied strain step

For all material models, the inclusions have partially debonded at the top and bottom side from the matrix. Since debonding occurs at identical locations for all material models, final debonding is shown in Figure 5.31f for the P model only, which has the largest debonded area of all models.

In Figure 5.30, the plastic strain contours after some full debonding are entirely located at the left and right sides of the inclusion for all models. The plastic strain that was present near the top and bottom of the inclusion has become far less significant for the CPX and CPA models as it was previously.

Relative displacement at the top of the inclusion has increased significantly for the crystal plasticity models and are even larger than for the elasticity case, as shown in Figure 5.31.

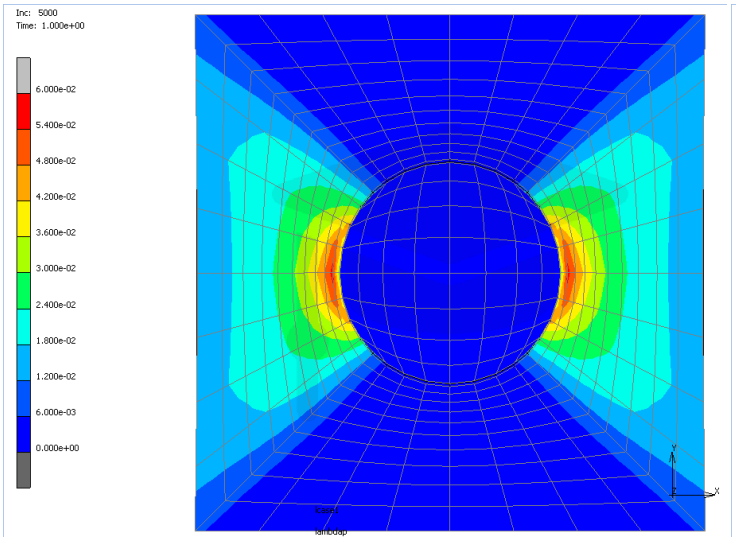

(a) Plastic strain of P model at seventh applied strain step.

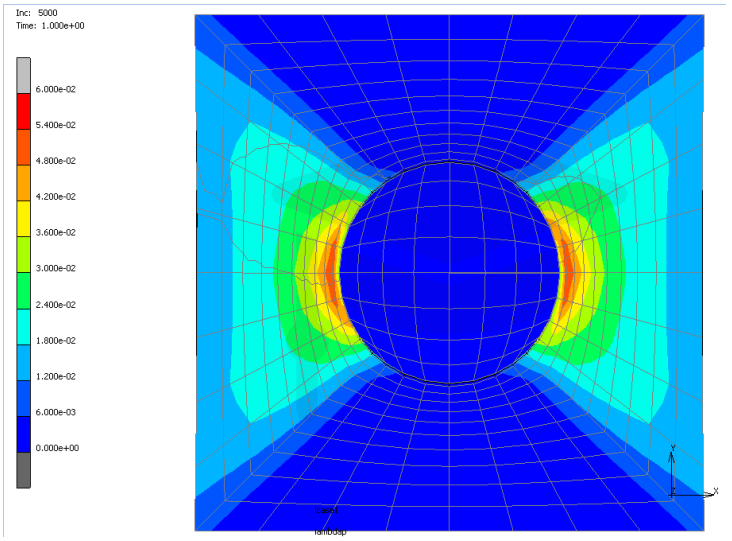

(b) Plastic strain of PTF model at seventh applied strain step.

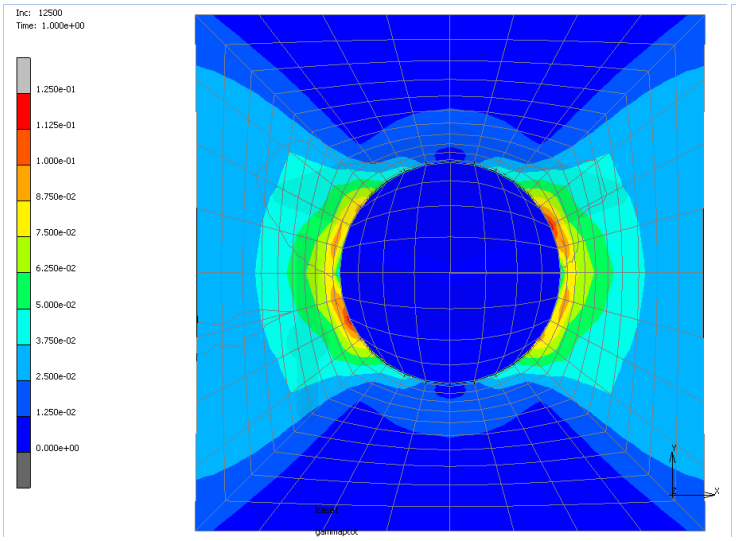

(c) Plastic slip of CPX model at seventh applied strain step.

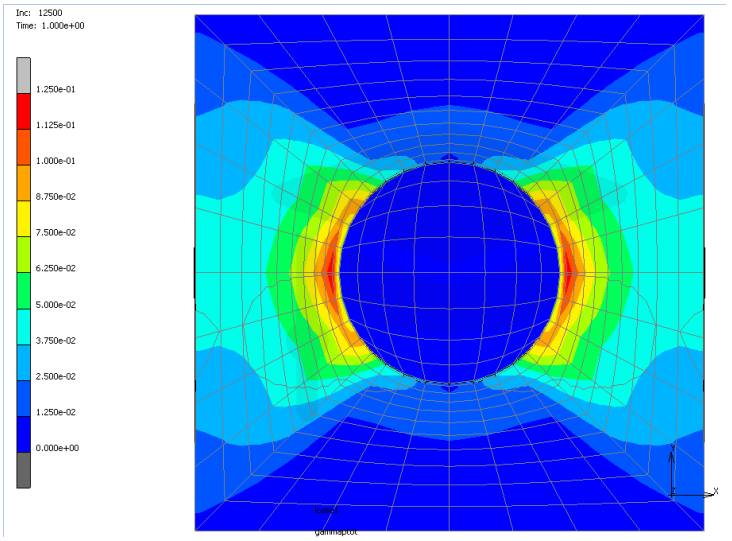

(d) Plastic slip of CPA model at seventh applied strain step.

Figure 5.30: Plastic strain of all plasticity models at seventh applied strain step.

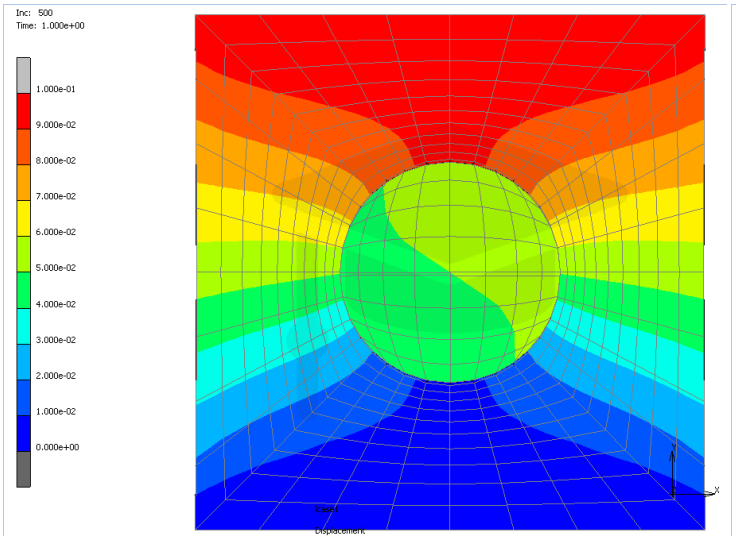

(a) Displacements of E at seventh applied strain step.

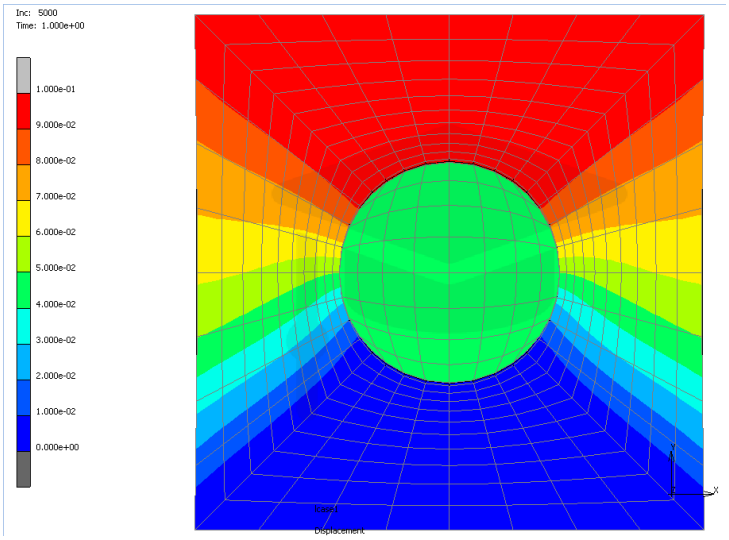

(b) Displacements of P at seventh applied strain step.

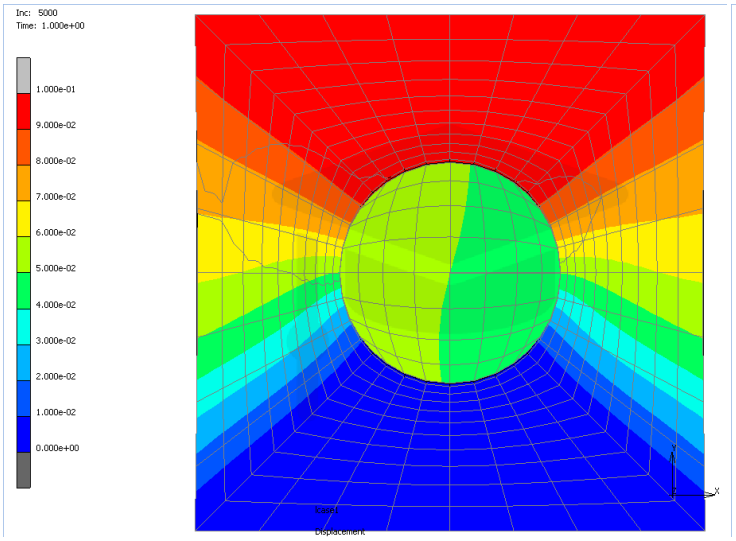

(c) Displacements of PTF at seventh applied strain step.

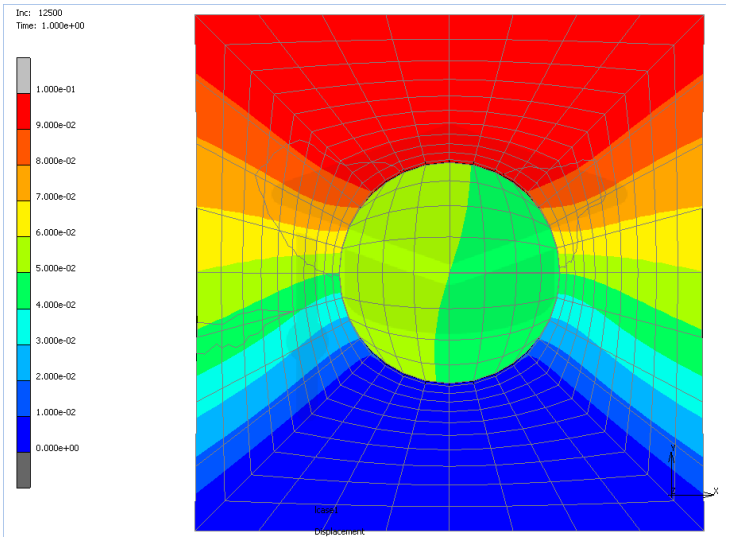

(d) Displacements of CPX at seventh applied strain step.

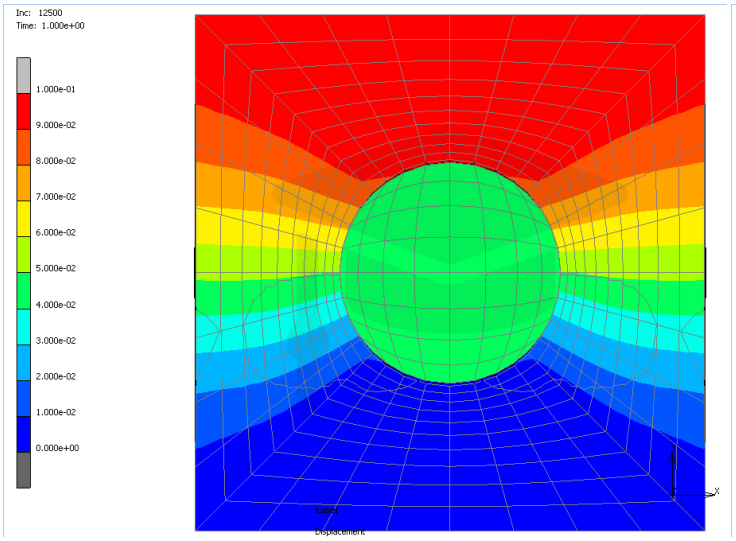

(e) Displacements of CPA at seventh applied strain step.

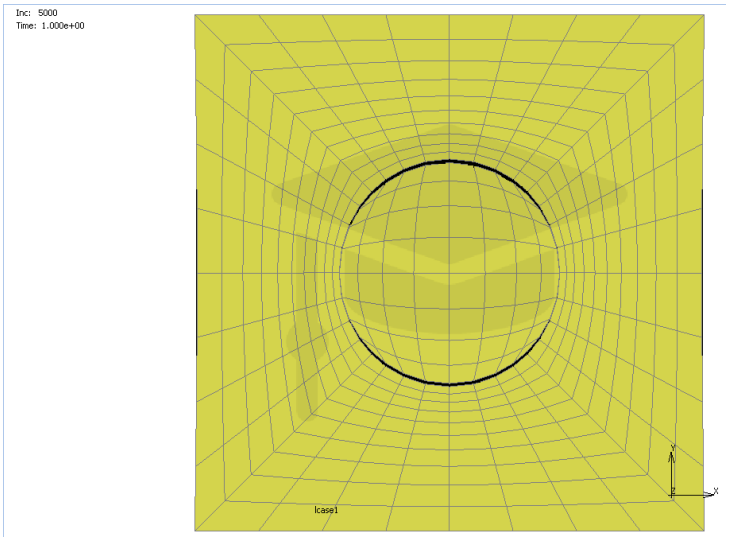

(f) Final debonding for P model. Space with deleted cohesive zone elements is indicated with black.

Figure 5.31: Displacements for all models at seventh applied strain step including final debonding of the P model.

Chapter 6

Discussion

6.1 Global behaviour

As described in the results, multiple stiffness drops are observed in the global stress/strain response of the complete system of inclusion and matrix. These changes in the slopes of the five curves can be explained by investigating the local stress and plastic strain fields at the chosen applied strain steps as indicated in Figure 5.9 and Table 5.2.

Stress plots at the first applied strain step ($\varepsilon_1 = 7.5 \cdot 10^{-5}$) showed that the stresses were the same for all material models, meaning that no yielding has occurred yet. At the second applied strain step ($\varepsilon_2 = 2.5 \cdot 10^{-4}$), however, differences in stress were observed as shown in Figure 5.11. The stress had namely increased at the sides of the inclusion in the elastic and isotropic plastic matrices, while this was not the case for both crystal plasticity models. This indicates that the first stiffness drops of the curve of the crystal plasticity models are related to yielding.

At the third ($\varepsilon_3 = 5.5 \cdot 10^{-4}$) and fourth ($\varepsilon_4 = 1.125 \cdot 10^{-3}$) applied strain steps, the stresses stop increasing with the elasticity matrix for the P and PTF matrices, respectively. This means that the matrix has plastically deformed at these two applied strain steps for both material models. Therefore, the first stiffness drop of both the P and PTF models are related to a yielding matrix too.

From Figure 5.24, it became clear that damage to the cohesive zone layer has initiated for the elasticity and both isotropic plasticity models at the fourth applied strain step. This damage initiation indicates the onset of debonding for these three models and implies that this happens between the third and fourth applied strain steps in Figure 5.9. The first stiffness drop of the elasticity model and the second drop of the PTF model thus are related to the onset of debonding, as these drops start in between the third and fourth applied strain steps. Only one smooth stiffness drop is observed for P, meaning that the drops for the yielding and debonding must coincide.

The same logic can be applied to both crystal plasticity material models. Small damage is observed at the fifth applied strain step ($\varepsilon_5 = 2.9 \cdot 10^{-3}$) for the CPX model and more for the CPA model. Therefore, the onset of debonding happens for CPX just before the fifth applied strain step and the onset of debonding for CPA occurs earlier than that for the CPX case. So, the second drops of the crystal plasticity curves are related to debonding of the inclusion from the matrix as well.

6.2 Order of debonding

An important result of this research is the order in which debonding occurs. The applied strain at which deletion of the first cohesive zone element takes place, can act as a parameter to establish this order. From low to high applied strain, the following order was obtained: P > PTF > E > CPA > CPX.

In the simulations, the crystal plasticity matrices start yielding at lowest applied strain. Plots of the total plastic slip, for example in Figure 5.12, show plastic deformation near the left and right sides of the inclusion. The main active slip systems during initial yielding were found to be 14, 17, 20 and 23 for CPX, and 18 and 21 for CPA. The activation of these slip systems makes sense, since these slip systems are the ones with the highest Schmid factor $\cos(\lambda)\cos(\phi)$, thus resulting in highest resolved shear stress according to Schmid's law for uniaxial tension:

$$\tau = \sigma \cos(\lambda)\cos(\phi) \tag{6.1}$$

Slip system (CPX)	Slip plane	Slip direction
14	$(\bar{1}21)$	$[11\bar{1}]$
17	$(12\bar{1})$	$[1\bar{1}\bar{1}]$
20	(121)	$[1\bar{1}1]$
23	$(1\bar{2}1)$	$[111]$
Slip system (CPA)	Slip plane	Slip direction
18	$(0\bar{1}\sqrt{2})$	$[0\sqrt{2}\bar{1}]$
21	$(01\sqrt{2})$	$[0\sqrt{2}1]$

Table 6.1: Main first activated slip systems.

The direction of the plastic deformation partially points in the opening direction of the cohesive zone at the top and bottom of the inclusion, which led to higher displacement differences between the inclusion and matrix at this location. At this point, the displacement at these locations are higher for the crystal plasticity models than the elasticity and isotropic plasticity models.

However, increased applied strain leads to higher stresses at the top and bottom of the inclusion for the crystal matrices, leading to more activated slip systems and more slip on other locations of already active slip systems, resulting in total plastic slip. This plastic slip points in various directions, including the opening direction. As a displacement is applied to the top of the matrix, a certain amount of displacement is allowed. If at the top of the inclusion much plastic deformation occurs in the opening direction, less opening displacement will be present. Therefore, the displacement difference at the top of the inclusion is now lower for both crystal plasticity models compared to the rest of the models. The same holds for the bottom. In addition, the PTF matrix starts to yield as the first of the two isotropic plasticity models. This plastic deformation is highest at the left and right side of the inclusion, leading to higher displacement at the top of the inclusion and lower displacement at the bottom of the inclusion. The P matrix has not yielded yet, hence the PTF matrix has the highest displacement difference between the inclusion and matrix near the top and bottom. Thereafter, the P matrix starts to show plastic deformation at the left and right sides of the inclusion, leading to extra displacement in the y-direction near the top of the inclusion. The PTF matrix starts to show some plastic deformation that is near the top of the inclusion. As a consequence the displacement difference between matrix and inclusion near the top of inside the PTF matrix is slightly lower than that of the P matrix.

The fact that debonding occurs earlier for CPA compared to CPX can be attributed to the slip system behaviour. At lower applied strain in the simulations, slip system activation follows Schmid's law for uniaxial tension along the y-axis ([010]). For CPX, the only slip systems with a Schmid factor of zero are: 3, 5, 8 and 11, which comes from the fact that their slip plane normals make angles of 90 degrees with the applied tension. Substantially more slip systems remain inactive at low applied strain for the CPA model. Slip systems 1-3, 10-12, 13-15 and 22-24 have Schmid factors of zero because the angles between their slip directions and the applied tension are 90 degrees. The slip plane normals of slip systems 6 and 9 make angles of 90 degrees with the applied tension as well. So at the early stage in the simulations, CPX has more activated slip systems which inhibit debonding.

Later on, new slip systems become active for CPA because the case cannot be seen as a uniaxial tension case, because of deformation in the x- and z-direction. Plastic slip coming from these slip systems contribute to the total plastic slip, but slip systems 1-3, 10-12, 13-15 and 22-24 are not directed in the y-direction, unlike all slip systems of CPX. As a consequence, plastic slip on these slip systems do not counteract debonding at the top and bottom of the inclusion. This leads to slightly earlier debonding for CPA and the aforementioned debonding order is governed.

6.3 Debonding strain interval and total surface area

If the difference is taken between the applied strain at first detected damage and the applied strain at which the first cohesive zone element is deleted, the following order is found from small to large difference: P > PTF > CPX > CPA > E. This difference is called the debonding strain interval and can be seen as the rate at which debonding occurs once it has started. As the plastic strain at the sides of the inclusion increases during the whole simulation, it is obvious that for the P and PTF models this difference is smallest.

Even though debonding occurs earlier (at lower applied strain) for E than for the crystal plasticity material models, the debonding strain interval is shorter for the crystal plasticity material models. The elasticity material

model did not show plastic deformation at all, so not on the top and bottom of the inclusion as well. The crystal plasticity material models did. As damage starts to increase in the cohesive zone elements, the stress starts to lower there according to the universal binding energy relation there. This means that at a certain point the stress decreases, and accordingly the plastic slip that inhibits opening of the cohesive zone. As the plastic slip decreases at the top and bottom of the inclusion, more opening displacement is allowed, which accelerates the debonding process once damage has initiated. The same reasoning can be applied to the order of the fraction of deleted cohesive zone elements.

6.4 Crystal plasticity role assessment

To come back to the initial goal of the research, the role of crystal plasticity on the void nucleation process should be assessed. Crystal plasticity inhibits debonding at first, as plastic deformation occurs early due to a low slip resistance. The plastic deformation is not only located at the left and right sides of the inclusion when being subjected to uniaxial tension, but also at the top and bottom.

Debonding being suppressed by crystal plasticity, can be related to a size effect. In Figure 6.1, two schematics of an inclusion inside a matrix are shown. The first inclusion lies inside a polycrystal matrix, which means that the plastic anisotropy is averaged out and the matrix behaves isotropic. The inclusion is larger than the grain size. The second inclusion lies inside a single crystal matrix, meaning that there is plastic anisotropy present and the inclusion is smaller than the grain size. Therefore, the effect that larger inclusions debond earlier compared to small inclusions could be explained by the effect that inclusions debond later in crystal plasticity matrices.

It is expected that other crystal orientations or boundary conditions could lead to other debonding locations. The reason for this is that if the plastic slip contours become asymmetric on the x-y plane, debonding is only inhibited at a certain side of the inclusion and not on the whole top and bottom as was the case in this research.

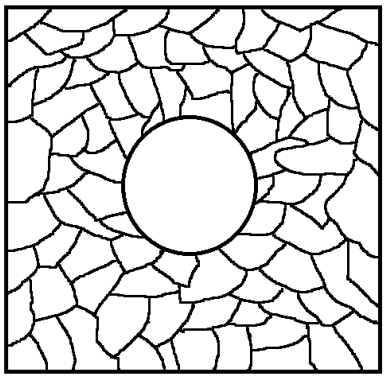

(a) Schematic of inclusion inside a polycrystal where the grain size < inclusion size.

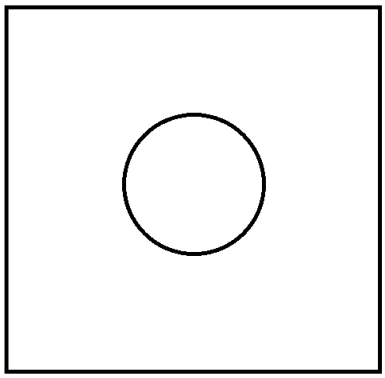

(b) Schematic of inclusion inside a single crystal where the grain size > inclusion size.

Figure 6.1: Schematics of inclusion inside a polycrystal and single crystal.

Chapter 7

Conclusions

FEM simulations have been performed on a matrix containing an elastic inclusion with a cohesive zone layer in between. Five different material models were used to describe the behaviour of the matrix, which were a purely elastic material model (E), two isotropic plasticity models with different yield strengths (P and PTF) and two crystal plasticity models of which one was unrotated (CPX) and one was rotated (CPA). Global stress/strain curves were obtained from uniaxial tests on this geometry and certain conclusions were made. The results were investigated by analysing the local behaviour at different steps of the applied strain.

Various drops in stiffness were observed in the resulting stress/strain curves, which were related to yielding and debonding. Therefore, each material model had two drops in slope, except for the pure elasticity material model as that matrix did not yield. Both crystal plasticity models yielded first, where the initial stiffness drop was largest for the unrotated crystal. At larger applied strain, the P and PTF matrices started showing plastic deformation and a drop in slope is observed for these models. Subsequently, five stiffness drops occur for all models, which starts earliest for P, then for PTF, then for E, and eventually for CPA and CPX.

It was determined at which applied strain the first damage was done to the cohesive zone layer and at which applied strain the first cohesive zone element was deleted. This order is in agreement with the order at which the debonding stiffness drops occur, namely from low to high applied strain: P < PTF < E < CPA < CPX. The exact values can be observed in Table 5.1.

This order can be explained by plastic deformation around the inclusion. At quite low applied strain, plastic deformation starts occurring at the top and bottom of the inclusion in the crystal plasticity matrices as a result of the low slip resistance. As a consequence, the top side of the matrix deforms more than that the cohesive zone can open. Plastic deformation also occurs in the isotropic plasticity matrices, but stays mainly on the left and right sides of the inclusion. This leads to a higher opening displacement on the top and bottom of the inclusion. As a consequence, the isotropic plasticity models debond first, then the elasticity model and eventually the crystal plasticity models. The P model debonds earlier than the PTF model, because there is slight plastic deformation inside the PTF matrix at the top and bottom of the inclusion.

The difference in strain between the first observed damage and the first deleted cohesive zone element was determined as well, of which the values are listed in Table 5.1. This difference gives information about the speed at which the inclusion debonds once damage has initiated. The order from small to large is given by: P > PTF > CPX > CPA > E.

Both crystal plasticity models debond faster compared to the elasticity model, while debonding occurs at lower applied strain. An explanation could be that, as damage increases inside the cohesive zone layer, the stress eventually decreases as a result of its traction-separation relation. This results in less plastic deformation at the top and bottom of the inclusion, resulting in an acceleration of the debonding process once damage starts.

Debonding is observed to occur at the top and bottom sides of the inclusion in the simulations performed in this research.

Chapter 8

Recommendations

Potential improvements, as well as suggestions for follow-up research are discussed in this section. A lot of research on this topic can be done, however, one has to keep in mind the total duration of the research project.

8.1 Improvements of current work

Principal stress computation

Principal stresses are responsible for debonding of surfaces. These can be obtained by using spectral decomposition, but no time was left to implement this in the subroutines. For this reason, σ_{yy} was used, which comes close if the surface normals are directed in the y-direction. But, principal stresses should be plotted for debonding anywhere.

Hardening

Hardening is not accounted for in this research. Implementing this phenomenon for both isotropic plasticity and crystal plasticity would result in a more realistic material response.

8.2 Future work

Stress triaxiality

Originally, the idea was to do an analysis of the stress triaxiality. This is interesting with crystal plasticity because it can increase the effect that crystal orientations have. This could not be done, however, because it was too computationally expensive. These boundary conditions required such a small time step for the forward Euler method that the time did not allow it.

Compression

Another interesting boundary condition to investigate is the case of compression.

Other crystal orientations

Additional crystal orientations can be considered. Potentially, this could lead to debonding on different sites because of plastic deformation developing in an asymmetric manner. This plastic deformation could inhibit debonding in an asymmetric manner.

Particle cracking

A large portion of void nucleation cases is the result of particle cracking. Therefore it would be very relevant to look into this phenomenon in combination with crystal plastic anisotropy.

Rest of ductile fracture process

Void nucleation is the first step in the entire ductile fracture process. This research can be taken further to the next step: void growth, which turns into a contact problem. Also void coalescence could be investigated, or even the complete ductile fracture process. Growth, coalescence or complete fracture using CP

Chapter 9

References

[1] John Reynolds. *99 Diseases of Pressure Equipment: Brittle Fracture*. Feb. 2007. URL: https://inspectioneering.com/journal/2007-01-01/3683/99-diseases-of-pressure-equipm.

[2] F. Roters et al. "Overview of constitutive laws, kinematics, homogenization and multiscale methods in crystal plasticity finite-element modeling: Theory, experiments, applications". In: *Acta Materialia* 58.4 (Feb. 2010), pp. 1152–1211. DOI: 10.1016/j.actamat.2009.10.058. URL: https://doi.org/10.1016/j.actamat.2009.10.058.

[3] *Stress–strain curve*. Feb. 2022. URL: https://en.wikipedia.org/wiki/Stress%5C%E2%5C%80%5C%93strain_curve.

[4] F. Maresca. *Finite element modelling for advanced processing Lecture notes*. 2021.

[5] Ekkehart Kröner. "Allgemeine Kontinuumstheorie der Versetzungen und Eigenspannungen". In: *Archive for Rational Mechanics and Analysis* 4.1 (Jan. 1959), pp. 273–334. DOI: 10.1007/bf00281393. URL: https://doi.org/10.1007/bf00281393.

[6] E. H. Lee and D. T. Liu. "Finite-Strain Elastic—Plastic Theory with Application to Plane-Wave Analysis". In: *Journal of Applied Physics* 38.1 (Jan. 1967), pp. 19–27. DOI: 10.1063/1.1708953. URL: https://doi.org/10.1063/1.1708953.

[7] E. H. Lee. "Elastic-Plastic Deformation at Finite Strains". In: *Journal of Applied Mechanics* 36.1 (Mar. 1969), pp. 1–6. DOI: 10.1115/1.3564580. URL: https://doi.org/10.1115/1.3564580.

[8] F. Maresca, V.G. Kouznetsova, and M.G.D. Geers. "Reduced crystal plasticity for materials with constrained slip activity". In: *Mechanics of Materials* 92 (Jan. 2016), pp. 198–210. DOI: 10.1016/j.mechmat.2015.09.011. URL: https://doi.org/10.1016%5C%2Fj.mechmat.2015.09.011.

[9] E. van der Giessen. *Solid Mechanics for Applied Physicists*. 2018.

[10] E Schmid. *Kristallplastizität: Mit Besonderer Berücksichtigung der Metalle*. Springer, 1935.

[11] *Slip geometry: the critical resolved shear stress*. 2022. URL: https://www.doitpoms.ac.uk/tlplib/slip/slip_geometry.php.

[12] J.R. Rice. "Inelastic constitutive relations for solids: An internal-variable theory and its application to metal plasticity". In: *Journal of the Mechanics and Physics of Solids* 19.6 (Nov. 1971), pp. 433–455. DOI: 10.1016/0022-5096(71)90010-x. URL: https://doi.org/10.1016/0022-5096(71)90010-x.

[13] J.W. Hutchinson. "Bounds and self-consistent estimates for creep of polycrystalline materials". In: *Proceedings of the Royal Society of London. A. Mathematical and Physical Sciences* 348.1652 (Feb. 1976), pp. 101–127. DOI: 10.1098/rspa.1976.0027. URL: https://doi.org/10.1098/rspa.1976.0027.

[14] Woojin Jeong et al. "Grain Scale Representative Volume Element Simulation to Investigate the Effect of Crystal Orientation on Void Growth in Single and Multi-Crystals". In: *Metals* 8.6 (June 2018), p. 436. DOI: 10.3390/met8060436. URL: https://doi.org/10.3390/met8060436.

[15] F. Maresca, V.G. Kouznetsova, and M.G.D. Geers. “Subgrain lath martensite mechanics: A numerical–experimental analysis”. In: *Journal of the Mechanics and Physics of Solids* 73 (Dec. 2014), pp. 69–83. DOI: 10.1016/j.jmps.2014.09.002. URL: https://doi.org/10.1016/j.jmps.2014.09.002.

[16] F. Hannard et al. “Characterization and micromechanical modelling of microstructural heterogeneity effects on ductile fracture of 6xxx aluminium alloys”. In: *Acta Materialia* 103 (Jan. 2016), pp. 558–572. DOI: 10.1016/j.actamat.2015.10.008. URL: https://doi.org/10.1016/j.actamat.2015.10.008.

[17] T. Pardoen. *Recent progress in micromechanics-based approaches of ductile fracture in metals*. May 2022.

[18] I Baker. *Fifty Materials That Make the World*. Springer, 2018.

[19] R. F. Cochrane. *Micrograph 224 and full record*. Sept. 2002. URL: https://www.doitpoms.ac.uk/miclib/micrograph_record.php?id=224.

[20] Kun Zhou et al. “A review of recent works on inclusions”. In: *Mechanics of Materials* 60 (July 2013), pp. 144–158. DOI: 10.1016/j.mechmat.2013.01.005. URL: https://doi.org/10.1016/j.mechmat.2013.01.005.

[21] “The determination of the elastic field of an ellipsoidal inclusion, and related problems”. In: *Proceedings of the Royal Society of London. Series A. Mathematical and Physical Sciences* 241.1226 (Aug. 1957), pp. 376–396. DOI: 10.1098/rspa.1957.0133. URL: https://doi.org/10.1098/rspa.1957.0133.

[22] “The elastic field outside an ellipsoidal inclusion”. In: *Proceedings of the Royal Society of London. Series A. Mathematical and Physical Sciences* 252.1271 (Oct. 1959), pp. 561–569. DOI: 10.1098/rspa.1959.0173. URL: https://doi.org/10.1098/rspa.1959.0173.

[23] M. A. CONTRERAS et al. “Use of the small punch test to determine the ductile-to-brittle transition temperature of structural steels”. In: *Fatigue and Fracture of Engineering Materials and Structures* 31.9 (Oct. 2008), pp. 727–737. DOI: 10.1111/j.1460-2695.2008.01259.x. URL: https://doi.org/10.1111/j.1460-2695.2008.01259.x.

[24] N Hussein. *Materials science and engineering*. International energy and environment foundation, 2017.

[25] Shakir Gatea et al. “Modelling of ductile fracture in single point incremental forming using a modified GTN model”. In: *Engineering Fracture Mechanics* 186 (Dec. 2017), pp. 59–79. DOI: 10.1016/j.engfracmech.2017.09.021. URL: https://doi.org/10.1016/j.engfracmech.2017.09.021.

[26] S.H. Goods and L.M. Brown. “Overview No. 1: The Nucleation of Cavities by Plastic Deformation”. In: *Acta Metallurgica* 27.1 (Jan. 1979), pp. 1–15. DOI: 10.1016/0001-6160(79)90051-8. URL: https://doi.org/10.1016%5C%2F0001-6160%5C%2879%5C%2990051-8.

[27] Tsuyoshi INOUE and Shushi KINOSHITA. “Three Stages of Ductile Fracture Process and Criteria of Void Initiation in Spheroidized and Ferrite/Pearlite Steels”. In: *Transactions of the Iron and Steel Institute of Japan* 17.9 (Sept. 1977), pp. 523–531. DOI: 10.2355/isijinternational1966.17.523. URL: https://doi.org/10.2355/isijinternational1966.17.523.

[28] K. Tanaka, T. Mori, and T. Nakamura. “Cavity formation at the interface of a spherical inclusion in a plastically deformed matrix”. In: *The Philosophical Magazine: A Journal of Theoretical Experimental and Applied Physics* 21.170 (Feb. 1970), pp. 267–279. DOI: 10.1080/14786437008238415. URL: https://doi.org/10.1080/14786437008238415.

[29] Matthieu Marteleur et al. “Ductile fracture of high strength steels with morphological anisotropy, Part I: Characterization, testing, and void nucleation law”. In: *Engineering Fracture Mechanics* 244 (Mar. 2021), p. 107569. DOI: 10.1016/j.engfracmech.2021.107569. URL: https://doi.org/10.1016/j.engfracmech.2021.107569.

[30] G.I. Barenblatt. “The Mathematical Theory of Equilibrium Cracks in Brittle Fracture”. In: *Advances in Applied Mechanics*. Elsevier, 1962, pp. 55–129. DOI: 10.1016/s0065-2156(08)70121-2. URL: https://doi.org/10.1016/s0065-2156(08)70121-2.

[31] P. Andric. *The mechanics of crack-tip dislocation emission and twinning*. Apr. 2019.

[32] Viggo Tvergaard and John W. Hutchinson. "The relation between crack growth resistance and fracture process parameters in elastic-plastic solids". In: *Journal of the Mechanics and Physics of Solids* 40.6 (Aug. 1992), pp. 1377–1397. DOI: 10.1016/0022-5096(92)90020-3. URL: https://doi.org/10.1016/0022-5096(92)90020-3.

[33] A. Needleman. "A Continuum Model for Void Nucleation by Inclusion Debonding". In: *Journal of Applied Mechanics* 54.3 (Sept. 1987), pp. 525–531. DOI: 10.1115/1.3173064. URL: https://doi.org/10.1115%5C%2F1.3173064.

[34] X-P Xu and A Needleman. "Void nucleation by inclusion debonding in a crystal matrix". In: *Model. Simul. Mat. Sci. Eng.* 1.2 (Jan. 1993), pp. 111–132.

[35] MSC software. *Marc 2021.1 Volume B: Element Library*. 2021.

[36] Xin Liu et al. "Experimental study on the influence of locked-in stress on the uniaxial compressive strength and elastic modulus of rocks". In: *Scientific Reports* 10.1 (Oct. 2020). DOI: 10.1038/s41598-020-74556-1. URL: https://doi.org/10.1038/s41598-020-74556-1.

[37] G. Le Roy et al. "A model of ductile fracture based on the nucleation and growth of voids". In: *Acta Metallurgica* 29.8 (Aug. 1981), pp. 1509–1522. DOI: 10.1016/0001-6160(81)90185-1. URL: https://doi.org/10.1016%5C%2F0001-6160%5C%2881%5C%2990185-1.

[38] C. Du et al. "Ferrite slip system activation investigated by uniaxial micro-tensile tests and simulations". In: *Acta Materialia* 146 (Mar. 2018), pp. 314–327. DOI: 10.1016/j.actamat.2017.12.054. URL: https://doi.org/10.1016%5C%2Fj.actamat.2017.12.054.

[39] J. M. Rosenberg and H. R. Piehler. "Calculation of the taylor factor and lattice rotations for bcc metals deforming by pencil glide". In: *Metallurgical Transactions* 2.1 (Dec. 1971), pp. 257–259. DOI: 10.1007/bf02662666. URL: https://doi.org/10.1007/bf02662666.

[40] H K D H Bhadeshia. "Cementite". en. In: *Int. Mater. Rev.* 65.1 (Jan. 2020), pp. 1–27.

[41] J. R. Fisher and J. Gurland. "Void nucleation in spheroidized carbon steels Part 2: Model". In: *Metal Science* 15.5 (May 1981), pp. 193–202. DOI: 10.1179/030634581790426660. URL: https://doi.org/10.1179%5C%2F030634581790426660.

[42] A. Brownrigg et al. "The influence of hydrostatic pressure on the flow stress and ductility of a spherodized 1045 steel". In: *Acta Metallurgica* 31.8 (Aug. 1983), pp. 1141–1150. DOI: 10.1016/0001-6160(83)90176-1. URL: https://doi.org/10.1016%5C%2F0001-6160%5C%2883%5C%2990176-1.

[43] H. Cialone and R. J. Asaro. "The role of hydrogen in the ductile fracture of plain carbon steels". In: *Metallurgical Transactions A* 10.3 (Mar. 1979), pp. 367–375. DOI: 10.1007/bf02658347. URL: https://doi.org/10.1007%2Fbf02658347.

[44] MSC software. *Marc 2021.1 Volume C: Element Library*. 2021.

Appendix A

FEM algorithms

A.1 Elasticity implementation

Algorithm 1: Elasticity FEM

discretise domain (define nodal positions $\boldsymbol{x}$ and element connectivity);
define model parameters ($\mathbb{C}$);
set total prescribed displacement $\boldsymbol{u}$;
initialise $\boldsymbol{y} = \boldsymbol{x} + \boldsymbol{u}$;
while $|\boldsymbol{f}_{ext} - \boldsymbol{f}_{int}| > \omega^{NR}$ *and* $i < i_{max}$ **do**
  for *each integration point* **do**
    compute in order: $\boldsymbol{F}_{(i)}$, $\boldsymbol{C}_{(i)}$, $\boldsymbol{E}_{(i)}$, $\boldsymbol{S}_{(i)}$, $\boldsymbol{P}_{(i)}$, $\boldsymbol{K}_{m(i)}$, $\boldsymbol{f}_{int_{m(i)}}$;
  end
  assembly: $\boldsymbol{K}_{m(i)} \rightarrow \boldsymbol{K}_{(i)}$ and $\boldsymbol{f}_{int_{m(i)}} \rightarrow \boldsymbol{f}_{int_{(i)}}$;
  solve $\boldsymbol{K}_{(i)}\delta\boldsymbol{y} = \boldsymbol{f}_{ext} - \boldsymbol{f}_{int_{(i)}}$;
  update $\boldsymbol{y}_{(i+1)} = \boldsymbol{y}_{(i)} + \delta\boldsymbol{y}$
end

A.2 Isotropic plasticity implementation

Algorithm 2: Isotropic Plasticity FEM

discretise domain (define nodal positions $\boldsymbol{x}$ and element connectivity);
define model parameters ($\dot{\lambda}_0$, $\bar{M}_y$, $\mathbb{C}$);
set total displacement $\boldsymbol{u}$, displacement increments $\boldsymbol{u}_{incr}$, # increments N_{incr} and time step Δt;
initialise $\boldsymbol{y}(t_0)$=$\boldsymbol{x}$ and $\boldsymbol{F}_p(t_0) = \boldsymbol{I}$, $\boldsymbol{L}_p(t_0) = \boldsymbol{0}$;
for $n = 1 : N_{incr}$ **do**
  $\boldsymbol{y}(t_{n+1}) = \boldsymbol{y}(t_n) + \boldsymbol{u}_{incr}$;
  compute $\boldsymbol{F}_p(t_{n+1}) = (\boldsymbol{I} + \boldsymbol{L}_p(t_n)\Delta t) \cdot \boldsymbol{F}_p(t_n)$;
  while $|\boldsymbol{f}_{ext} - \boldsymbol{f}_{int}| > \omega^{NR}$ *and* $i < i_{max}$ **do**
    for *each integration point* **do**
      compute in order: $\boldsymbol{F}_{(i)}(t_{n+1})$, $\boldsymbol{F}_{e(i)}(t_{n+1})$, $\boldsymbol{C}_{e(i)}(t_{n+1})$, $\boldsymbol{E}_{e(i)}(t_{n+1})$, $\bar{\boldsymbol{S}}_{(i)}(t_{n+1})$, $\boldsymbol{S}_{(i)}(t_{n+1})$, $\boldsymbol{P}_{(i)}(t_{n+1})$, $\boldsymbol{K}_{m(i)}(t_{n+1})$, $\boldsymbol{f}_{int_{m(i)}}(t_{n+1})$;
    end
    assembly: $\boldsymbol{K}_{m(i)} \rightarrow \boldsymbol{K}_{(i)}$ and $\boldsymbol{f}_{int_{m(i)}} \rightarrow \boldsymbol{f}_{int_{(i)}}$;
    solve $\boldsymbol{K}_{(i)}\delta\boldsymbol{y} = \boldsymbol{f}_{ext} - \boldsymbol{f}_{int_{(i)}}$;
    update $\boldsymbol{y}_{(i+1)}(t_{n+1}) = \boldsymbol{y}_{(i)}(t_{n+1}) + \delta\boldsymbol{y}$
  end
  compute in order: $\bar{\boldsymbol{M}}(t_{n+1})$, $\bar{\boldsymbol{M}}^d(t_{n+1})$, $\bar{M}^d_{eq}(t_{n+1})$, $\boldsymbol{r}(t_{n+1})$, $\dot{\lambda}(t_{n+1})$, $\boldsymbol{L}_p(t_{n+1})$;
end

A.3 Crystal plasticity implementation

Algorithm 3: Crystal Plasticity FEM

discretise domain (define nodal positions $\boldsymbol{x}$ and element connectivity);
define model parameters ($\dot{\gamma}_0$, s^α, $\mathbb{C}$, $\boldsymbol{s}^\alpha$, $\boldsymbol{n}^\alpha$);
set total displacement $\boldsymbol{u}$, displacement increments $\boldsymbol{u}_{incr}$, # increments N_{incr} and time step Δt;
initialise $\boldsymbol{y}(t_0)$=$\boldsymbol{x}$ and $\boldsymbol{F}_p(t_0) = \boldsymbol{I}$, $\boldsymbol{L}_p(t_0) = \boldsymbol{0}$;
for $n = 1 : N_{incr}$ **do**
  $\boldsymbol{y}(t_{n+1}) = \boldsymbol{y}(t_n) + \boldsymbol{u}_{incr}$;
  compute $\boldsymbol{F}_p(t_{n+1}) = (\boldsymbol{I} + \boldsymbol{L}_p(t_n)\Delta t) \cdot \boldsymbol{F}_p(t_n)$;
  while $|\boldsymbol{f}_{ext} - \boldsymbol{f}_{int}| > \omega^{NR}$ *and* $i < i_{max}$ **do**
    for *each integration point* **do**
      compute in order: $\boldsymbol{F}_{(i)}(t_{n+1})$, $\boldsymbol{F}_{e(i)}(t_{n+1})$, $\boldsymbol{C}_{e(i)}(t_{n+1})$, $\boldsymbol{E}_{e(i)}(t_{n+1})$, $\bar{\boldsymbol{S}}_{(i)}(t_{n+1})$, $\boldsymbol{S}_{(i)}(t_{n+1})$, $\boldsymbol{P}_{(i)}(t_{n+1})$, $\boldsymbol{K}_{m(i)}(t_{n+1})$, $\boldsymbol{f}_{int_{m(i)}}(t_{n+1})$;
    end
    assembly: $\boldsymbol{K}_{m(i)} \rightarrow \boldsymbol{K}_{(i)}$ and $\boldsymbol{f}_{int_{m(i)}} \rightarrow \boldsymbol{f}_{int_{(i)}}$;
    solve $\boldsymbol{K}_{(i)}\delta\boldsymbol{y} = \boldsymbol{f}_{ext} - \boldsymbol{f}_{int_{(i)}}$;
    update $\boldsymbol{y}_{(i+1)}(t_{n+1}) = \boldsymbol{y}_{(i)}(t_{n+1}) + \delta\boldsymbol{y}$
  end
  compute in order: $\bar{\boldsymbol{M}}(t_{n+1})$, $\tau^\alpha(t_{n+1})$, $\dot{\gamma}^\alpha(t_{n+1})$, $\boldsymbol{L}_p(t_{n+1})$;
end

Appendix B

Simulation guide

This appendix serves as a guide to reproduce the results obtained in this research. First of all, four software packages are needed:

1. MSC Marc student edition
2. Microsoft visual studio 2022
3. Intel oneAPI base toolkit
4. Intel oneAPI HPC toolkit

The student edition of MSC Marc can be obtained from the MSC website (`https://www.mscsoftware.com/marc-student-edition`) by registering using a university email address. A fortran compiler is required as well to utilise the USELEM subroutine. Microsoft visual studio 2022 has to be installed and integrated with the fortran compiler. This Fortran compiler is included in the Intel oneAPI HPC toolkit, but in order for it to run, the Intel oneAPI base toolkit is needed as well. Microsoft visual studio 2022 (Community edition) can be downloaded at: `https://visualstudio.microsoft.com/vs/` and the Intel toolkits can be downloaded at: `https://www.intel.com/content/www/us/en/developer/tools/oneapi/toolkits.html#base-kit`. Once all this software is installed, the instructions in the readme file should be followed to add the location of the Fortran compiler and Microsoft visual studio to the environment variable path in order to use Marc with user subroutines.

Now Marc is ready to compile Fortran files and use them in FEM simulations. In these Fortran files, it should be programmed how the element stiffness matrix and internal forces are computed. To prevent getting corrupted files, Notepad++ can be used.

Geometry, mesh and boundary conditions can be chosen in the GUI of MSC Marc. To use the subroutine, the input file should be edited. In the Fortran files the element stiffness matrix and internal forces are obtained, but the element type should be specified inside the input file. This is done by adding the following line to the input file:

```
USER,-7,3,9,8,9,3,8,3,6,8,0,,61,
```

A description of these numbers can be found in volume C of Marc's manual [44]. Regular elements in MSC Marc are denoted by positive numbers. User elements are indicated by negative numbers, -7 in this case. If the subroutine involves time dependence, the number of state variables should be specified according to this line:

```
STATE VARS,118,
```

The elements that are listed in the input file before editing have positive numbers. The properties of user element -7 can be assigned to the corresponding elements by changing their numbers to -7, or by using the UFCONN subroutine and entering the elements that should be changed like this:

```
UFCONN
1 to 512,
```

To plot quantities that are calculated within the subroutines, the PLOTV subroutine is used. To communicate the values between the USELEM and PLOTV subroutines, COMMON blocks have to be used. PLOTV can be activated by entering the variable that has to be plotted under the *post* part in the input file. Again a negative number should be entered for the post variable, after that a zero and lastly the name of the post variable as follows:

```
-1,0,PKstress
```

Once the input file is set, the main Fortran file should be selected and the input file can be submitted to compute the results.